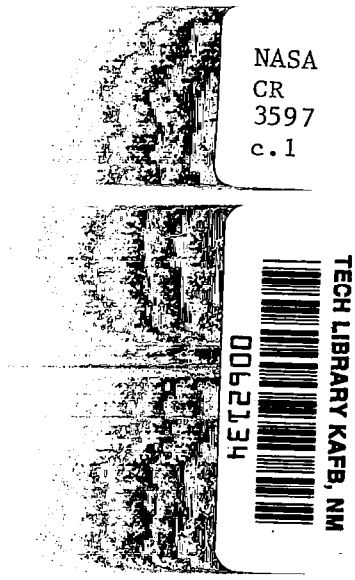

NASA Contractor Report 3597

Singular Perturbation Techniques for Real Time Aircraft Trajectory Optimization and Control

Anthony J. Calise and Daniel D. Moerder

GRANT NSG-1496
AUGUST 1982

NASA

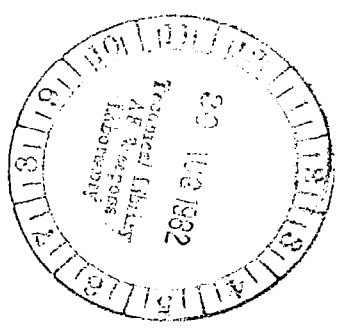

NASA Contractor Report 3597

Singular Perturbation Techniques for Real Time Aircraft Trajectory Optimization and Control

Anthony J. Calise and Daniel D. Moerder
Drexel University
Philadelphia, Pennsylvania

Prepared for
Langley Research Center
under Grant NSG-1496

National Aeronautics
and Space Administration

**Scientific and Technical
Information Branch**

1982

TABLE OF CONTENTS

Table of Contents (cont.)

LIST OF ILLUSTRATIONS

List of Illustrations (cont.)

LIST OF TABLES

SINGULAR PERTURBATION TECHNIQUES FOR REAL TIME AIRCRAFT TRAJECTORY OPTIMIZATION AND CONTROL

Anthony J. Calise* and Daniel D. Moerder+
Drexel University, Philadelphia, PA. 19104

SUMMARY

This study examines the usefulness of singular perturbation methods for developing real time computer algorithms to control and optimize aircraft flight trajectories. A minimum time intercept problem using F-8 aerodynamic and propulsion data is used as a baseline. This provides a framework within which issues relating to problem formulation, solution methodology and real time implementation are examined. Theoretical questions relating to separability of dynamics are addressed. With respect to implementation, situations leading to numerical singularities are identified, and procedures for dealing with them are outlined. Also, particular attention is given to identifying quantities that can be precomputed and stored, thus greatly reducing the on-board computational load. Numerical results are given to illustrate the minimum time algorithm, and the resulting flight paths. An estimate is given for execution time and storage requirements.

*Associate Professor, Dept. of Mechanical Engineering and Mechanics
+Graduate Research Assistant

SECTION 1

INTRODUCTION

This report documents the derivation and evaluation of an on-line algorithm for minimum-time intercept. An approximation to the solution of the minimum-time intercept problem, resulting in a feedback control law, was derived using singular perturbation theory. The resulting control logic was evaluated using a model for the F-8 aircraft dynamics.

The singular perturbation method is an order reduction procedure where a system's dynamics are separated into fast and slow modes. There are two major benefits. First, higher-order problems can be approximated by a series of lower-order ones; and second, numerically "stiff" systems, having extreme differences in their modal behavior are solved on separate time scales.

Applications of singular perturbation theory to flight mechanics problems have, to date, centered primarily on aircraft trajectory optimization. In the early seventies, a number of papers appeared in which energy state and reduced order modelling, with separate boundary layer correction terms, were employed to solve a number of flight control optimization problems [1-6]. Matched asymptotic expansions were employed somewhat later in solving the minimum-time-to-climb problem, observing that the first order approximation matched well with the numerical solution obtained for the full order problem using a steepest descent technique [7]. Singular arcs have also been studied in the minimum-time-to-climb problem [8, 9].

In a more recent sequence of papers, complete time scale separation has been applied in order to obtain feedback control solutions. Problems studied this way include the vertical plane minimum time and fuel problems and those involving weighted combinations of the two [10-15]. Feedback

control of a missile in the horizontal plane was examined in [16]. The three-dimensional minimum-time interception problem was examined by patching together two-dimensional subproblems in [17]. Under a NASA-supported research effort that paralleled this effort, trajectory optimization in the long range, three-dimensional minimum-time intercept problem has been studied [18]. Singular perturbation theory has also been found useful in differential game problems [19-21]. The results derived in this study are mainly based on the approach in [12].

The research described in this report resulted in several extensions in the "state of the art" for the three-dimensional minimum-time interception problem:

1. This work provides solutions for both long and short range cases, with short range cases being characterized by the lack of a maximum velocity cruise arc.
2. A boundary layer matching criterion was derived such that the terminal boundary layer matching conditions could be calculated off-line, thus eliminating the problem of attempting to backwards integrate the terminal boundary solution on-line. This has been identified as one of the major stumbling blocks encountered in the application of singular perturbation theory [22]. Indeed, in the short range case, matching between initial and terminal layer arcs is the key issue to be resolved in solving the problem.
3. The ordering and separation of energy and heading rate dynamics has been defined and justified for this problem, where range to interception is sufficiently large that optimal trajectories are dominantly characterized by climb and descent, rather than by turning. It should be noted that the ordering in this report is the reverse of that used in [1] and [10], and is due to the presence of relative position dynamics in the model.

4. A detailed analysis has been made of issues pertaining to the separation of altitude and flight path angle dynamics. Optimization of altitude and flight path angle dynamics is a classical problem in flight mechanics, which to date had not yielded a solution suitable for on-line implementation. The essential problem is that these dynamics are highly coupled when considered apart from position and energy dynamics. It is shown that the dynamics, while not completely separable, can be approximated by singular perturbation methods with the inclusion of a penalty term on flight path angle in the performance index.
5. The control algorithm was implemented as a flight director in the F-8 real time simulator at NASA Langley. Results of this evaluation are given in [23], and a NASA technical report is currently being prepared on this topic. The major issues relating to real time implementations have been addressed as part of the research effort.

The organization of this report is as follows. Section 2 describes the problem formulation and summarizes the zero order singular perturbation solution. Section 3 gives a summary of the on-line control logic, describing the practical issues encountered during implementation of the control law. Section 4 describes the point-mass model of the F-8 aircraft employed in generating numerical results. Section 5 presents numerical results for this aircraft. Section 6 gives the conclusions and recommendations for future work. Detailed derivations of the control solution presented in Section 2 may be found in Appendices A and B. The first deals with position, energy and heading dynamics, and the second, with altitude and flight path angle dynamics. Appendix C presents the analysis relating to separation and ordering of energy and heading rate dynamics. Appendix D presents a means

by which the altitude and flight path angle dynamics can be analyzed on separate time scales, and gives a detailed analysis of the issues involved. Appendix E provides a description of and justification for a procedure for minimizing a Hamiltonian function with one unknown adjoint variable, employed several times in the analysis in Appendices A and B. A detailed description of the measures taken to suppress numerical singularities from the computed control solution is given in Appendix F.

SYMBOLS

C_D = Drag Coefficient

C_{D_o} = Zero Lift Drag Coefficient

C_L = Lift Coefficient

C_{L_α} = Slope of Lift Coefficient Curve, 1/rad

D = Drag, N

D_o = Drag for L = W, N

E = Total Energy per Unit Weight, m

E_o = Pseudo Cruise Energy Level, m

E_o^* = Long Range Cruise Energy Level, m

g = Gravitational Constant, m/s^2

H = Hamiltonian

h = Altitude, m

K = Induced Drag Parameter

k = Flight Path Angle Weighting Parameter in Cost Function

L = Lift, N

L_1 = Vertical Lift Component, N

L_2 = Horizontal Lift Component, N

M = Mach Number

m = Mass, kg

P_E = Energy State and Costate Eigenvalues, 1/s

P_β = Heading State and Costate Eigenvalues, 1/s

q = Dynamic Pressure, N/m^2

r = Range, m

s = Reference Area, m^2

T = Thrust, N

t = Time, s

t_{go} = Time-To-Go, s

V = Velocity, m/s

W = Weight, N

x, y = Horizontal Position Variables, m

α = Angle of Attack, rad

α_o = Zero Lift Angle of Attack, rad

Symbols (cont.)

β = Heading, rad

γ = Flight Path Angle, rad

$\delta(.)$ = Perturbation Associated with a Particular Variable

ε = Perturbation Parameter

η = Induced Drag Parameter

λ = Line-of-Sight Angle, rad

λ_{E_1} = Energy Costate, s/m

λ_{h_3} = Altitude Costate, s/m

λ_{x_o}, λ_{y_o} = Horizontal Position Costates, s/m

λ_{β_2} = Heading Costate, s/rad

λ_{γ_4} = Flight Path Angle Costate, s/rad

μ = Bank Angle, rad

ρ = Air Density, kg/m^3

τ = Stretched Time Scale, s

τ_1, τ_2 = Time Constants, s

Subscripts

c = Climb

d = Descent

D = Desired

f = Final

p = Relating to Proportional Vertical Lift

max = Maximum

min = Minimum

T = Target

o = Outer Solution Variable or Solution

1, 2,3,4 = Boundary Layer Variables or Solution

Superscripts

$(\bar{.})$ = Nominal Value

o = Artificially Perturbed Variable

SECTION 2

PROBLEM FORMULATION AND SOLUTION

This section summarizes the problem formulation and the resulting singular perturbation solution. Derivations of the results summarized here may be found in Appendices A and B. Numerical results are given to illustrate the control solution for a variety of flight conditions.

2.1 Problem Formulation

The equations of motion are written in a horizontal, target centered coordinate frame:

$$\dot{x} = V \cos\gamma \cos\beta \tag{2.1}$$

$$\dot{y} = V \cos\gamma \sin\beta - V_T \cos\gamma_T \tag{2.2}$$

$$\varepsilon\dot{E} = (T-D)\, V/W \tag{2.3}$$

$$\varepsilon^2\dot{\beta} = L \sin\mu/m\, V \cos\gamma \tag{2.4}^{+}$$

$$\varepsilon^3\dot{h} = V \sin\gamma \tag{2.5}$$

$$\varepsilon^4\dot{\gamma} = (L \cos\mu - W \cos\gamma)/mV \tag{2.6}$$

The variables in (2.1-2.6) are defined with the aid of Figure 1, where the subscript "T" is used to designate the target. These equations are valid for a flat earth, with thrust (T) directed along the flight path and constant weight. Drag (D) is assumed to have a conventional parabolic form

$$D = qs\, C_D = qs(C_D + \eta\, C_{L_\alpha}\, \alpha^2) \tag{2.7}$$

which can also be written as

$$D = qs\, (C_D + KL^2/qs),\ q = \rho v^2/2 \tag{2.8}$$

where q is the dynamic pressure, ρ is the air density and

$$K = \eta/C_{L_\alpha} \tag{2.9}$$

$$L = qs\, C_L = qs(C_{L_\alpha}\, \alpha) \tag{2.10}$$

The variable E is the total aircraft energy (kinetic and potential) per unit weight.

+In this report, w/xyz is to be interpreted as w/(xyz).

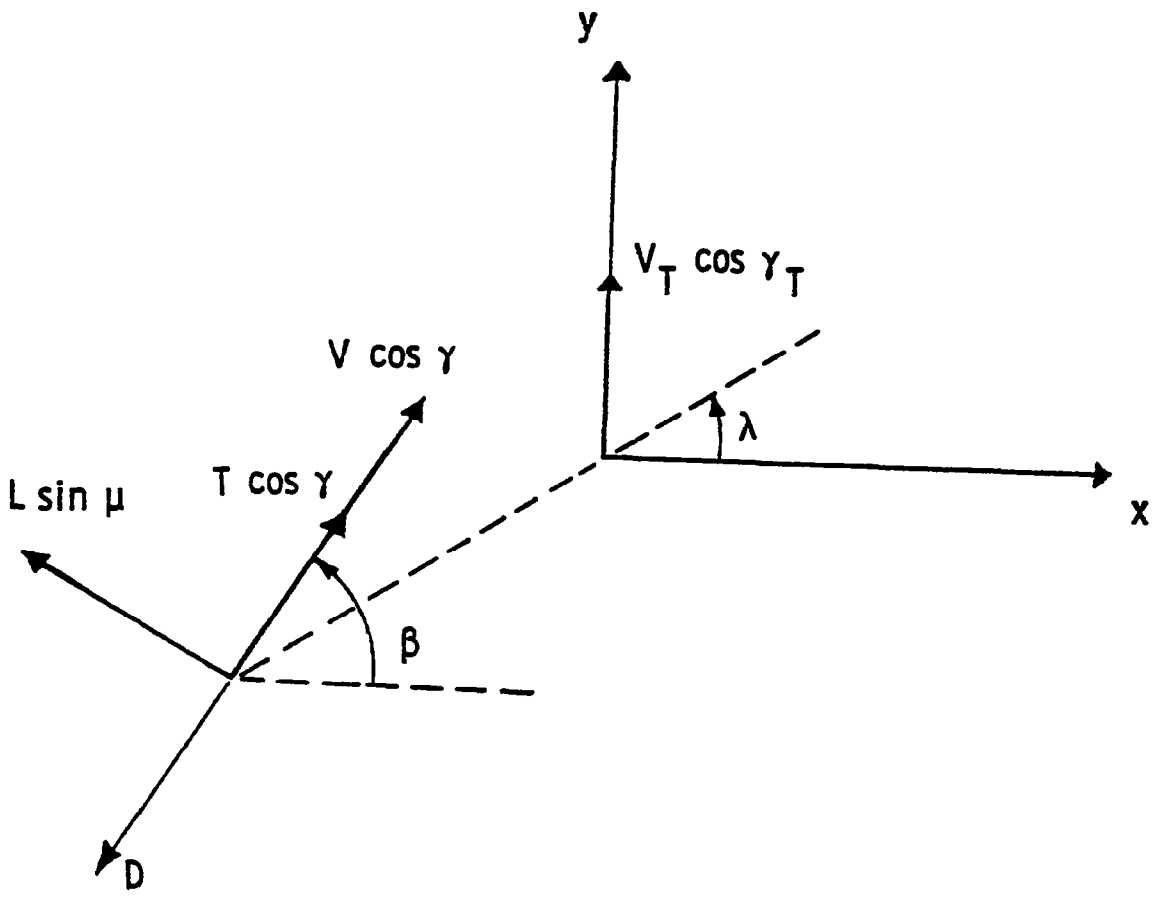

Figure 1. Horizontal plane intercept geometry

$$E = h + V^2/2g \tag{2.11}$$

where h is the aircraft altitude. The control variables are aircraft lift (L), bank angle (μ) and thrust (T). The objective is to find the controls L, μ, T that minimize

$$J = \int_o^{t_f} (1 + k \sin^2\gamma)dt \quad , \quad k \geq 0 \tag{2.12}$$

where k = 0 for minimum time. The minimization is subject to the following state and control variable constraints:

$$L \leq W G_{max} \tag{2.13}$$

$$L \leq qs \, C_{L_\alpha} \, \alpha_{max} \tag{2.14}$$

$$T_{min}(h, V) \leq T \leq T_{max}(h, V) \tag{2.15}$$

$$q \leq q_{max} \, , \, M \leq M_{max}(h) \tag{2.16}$$

where G_{max} is the maximum load factor, α_{max} is the stall angle of attack, T_{min} and T_{max} are the minimum and maximum thrust levels that are functions of aircraft altitude and velocity (V). The boundary conditions are such that the initial aircraft state is fully specified, and we require

$$x(t_f) = y(t_f) = 0 \, , \, h(t_f) = h_T(t_f) \tag{2.17}$$

for intercept, when $h_T(t_f)$ is taken as the projected target motion in altitude

$$h_T(t_f) = h_T(0) + (V_T \sin \gamma_T) \, t_f \tag{2.18}$$

The objective here in using singular perturbation methods is to approximate the open loop optimal control solution with a near-optimal control solution in feedback form. Towards this end, the equations of motion in (2.1-2.6) have been scaled by powers of ε, which imply that a natural separation in the system dynamics exists. Ideally, one would like to identify ε with small physical system parameters. This can be done with varying degrees of success by writting the equations of motion in a non-dimensional form. An example is given in [15]. The ordering selected in (2.1-2.6) is based on an understanding of aircraft dynamics, experience with problems in trajectory optimization, and the earlier results of researchers in this field. The approach here is to seek a solution for ε=1 by an expansion about ε=0. While this departs from the spirit of asymptotic expansions,

where ε is regarded as "sufficiently small", the accuracy of the resulting solution depends more on the degree to which the dynamics are separated.

The particular ordering selected here can be argued on a physical basis. Long range optimal trajectories are generally made up of climb, cruise and descent arcs. The climb and descent arcs can be considered as boundary layers needed to satisfy initial and terminal constraints on energy and altitude, during which energy is first increased (to the cruise energy) and then decreased (to satisfy the terminal altitude constraint). Initial transitions to the optimal climb path and the optimal heading for intercept take place on a much shorter time scale, in comparison to the time needed to gain or lose energy. Selecting β dynamics as slower than h and γ dynamics allows for high and low speed yo-yo maneuvers during the initial turn at large heading errors. This is illustrated in the results of Section 2.4. A detailed analysis of the ordering of E, β and h, γ dynamics is given in Appendices C and D.

2.2 Outer Solution

In the outer solution, the controlled aircraft is assumed to be travelling on a fixed course at a constant speed, as can be seen by letting $\varepsilon \to 0$ in (2.1-2.6). The problem is reduced to optimal intercept in the horizontal plane. The state variables are x and y, and the controls are β, h and E. In order to satisfy the intercept requirement (see Fig. 1), we must have

$$V\sin(\beta-\lambda) = V_T \cos\gamma_T \cos\lambda \tag{2.19}$$

or, in other words, there is no relative motion allowed perpendicular to the horizontal plane line-of-sight axis. The optimal controls h_o and E_o are determined as

$$h_o, E_o = \arg \max_{h,E} \ (V) \tag{2.20}$$

where the maximization takes place subject to the constraints in (2.13-2.16) and subject to

$$T_o = D_o, \ \mu_o = 0, \ \gamma_o = 0, \ L_o = W \tag{2.21}$$

where D_o is drag for L = W

$$D_o = qs\, C_{D_o} + KW^2/qs \tag{2.22}$$

and

$$q = \rho(h_o)V_o^2/2 \quad , \quad V_o = \sqrt{2g(E_o-h_o)} \tag{2.23}$$

These constraints arise from setting $\varepsilon \to 0$ in (2.2-2.6). The cruise point (2.20) for the F-8 aircraft is displayed in Figure 2, superimposed on the aircraft's flight envelope. It should be noted that, in a higher performance aircraft for which the q or Mach boundaries would be encountered while $T \geq D$, the solution would lie at the intersection of the constraint boundary with the zero energy rate boundary. This is illustrated for an F-4 aircraft in [25].

The optimal cruise heading (β_o)is computed using (2.19):

$$\beta_o = \sin^{-1} \{V_T \cos \gamma_T \cos \lambda/V\} + \lambda \tag{2.24}$$

The costates λ_{y_o} and λ_{y_o}, associated with the horizontal position dynamics in the outer solution, while not explicitly appearing in the outer control solution, are used in subsequent boundary layer solutions. These take the form

$$\lambda_{x_o} = -\cos\beta_o/(V_o - V_T \cos \gamma_T \cos \beta_o) \tag{2.25}$$

$$\lambda_{y_o} = -\sin\beta_o/(V_o - V_T \cos \gamma_T \cos \beta_o) \tag{2.26}$$

It should be noted that the cruise solution for h_o and E_o is independent of target motion and intercept geometry. This allows these quantities to be calculated off-line and stored. The only outer solution calculations performed on-line are (2.24-2.26).

2.3 First Boundary Layer Solution

The first boundary layer solution addresses energy dynamics. The constraints

$$\mu_1 = 0, \ \gamma_1 = 0, \ L_1 = W \tag{2.27}$$

in addition to (2.13-2.16), arise when the time transformation $\tau = t/\varepsilon$ is introduced and we let $\varepsilon \to 0$. The controls are T, h, and β. The optimal heading (β_1) is identical to that for the outer solution. Since T appears linearly in the dynamics, we have

$$T_1 = T_{max}(h,V) \quad , \quad \lambda_{E_1} < 0 \tag{2.28}$$

$$T_1 = T_{min}(h,V) \quad , \quad \lambda_{E_1} > 0 \tag{2.29}$$

where λ_{E_1} is the energy costate variable. The solutions in (2.28) and (2.29) essentially correspond to climb and descent. Optimization with respect to h yields

$$h_1 = \arg\min_h \{ \frac{(T_{max}-D_o)V}{V-V_o} \} \Big|_{\substack{E = E_{current} \\ T > D}} \tag{2.30}$$

for ascent, and

$$h_1 = \arg\min_h \{ \frac{-(T_{min}-D_o)V}{V-V_o} \} \Big|_{\substack{E = E_{current} \\ T < D}} \tag{2.31}$$

for descent.

The climb path to cruise for the F-8 is superimposed on the aircraft flight envelope as a bold line in Figure 2. The optimal descent path is along the q_{max} boundary. The expression for the first boundary layer costate is

$$\lambda_{E_1} = -WH_o(E,h_1)/V_1(T_1-D_o) \tag{2.32}$$

where $H_o(E, h_1)$ is the outer solution Hamiltonian evaluated at the first boundary conditions:

$$H_o(E,h_1) = \{\lambda_{x_o} V \cos\beta + \lambda_{y_o} (V\sin\beta - V_T\cos\gamma_T) + 1\} \Big|_{\substack{E = E_{current} \\ h = h_1}} \tag{2.33}$$

Since the solution for $h_1(E)$ is independent of target motion, it can be precomputed and stored as a function of E. Only the costate variable in (2.32) is computed on-line.

2.4 Second Boundary Layer

This boundary layer is obtained by introducing the time transformation $\tau = t/\varepsilon^2$ and letting $\varepsilon \to 0$. This results in the constraints:

$$\gamma_2 = 0 \quad , \quad L^2 = L_{22}^2 + W^2 \tag{2.34}$$

where L is the total lift and L_{22} is the horizontal lift component. The controls in this boundary layer are T, h, and L_{22}. Assuming that all turning takes place near the initial time where $\lambda_{E_1} < 0$, the optimal thrust is

$$T_2 = T_{max}(h_2, V_2) \tag{2.35}$$

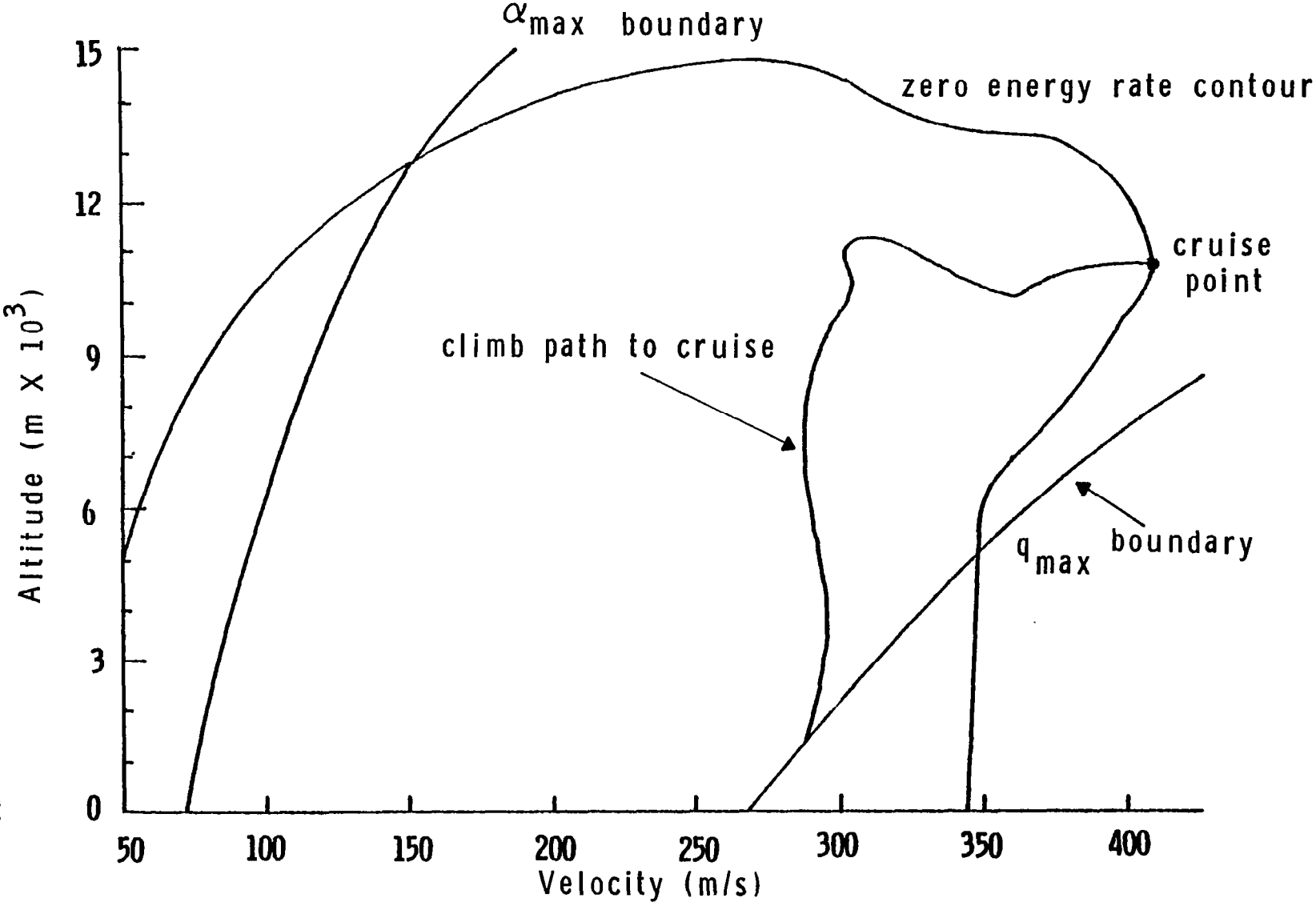

Figure 2. Flight envelope for the F-8 aircraft.

where h_2 is defined by

$$h_2 = \arg\min_h \{-\rho/KV\ H_1(E,h,\beta)\}\Big|_{\substack{E = E_{current} \\ \beta = \beta_{current}}} \tag{2.36}$$

$H_1(E, h, \beta)$ is the first boundary layer Hamiltonian evaluated at current values of E, h and β. It is expressed as

$$H_1(E, h, \beta) = \lambda_{x_o} V \cos\beta + \lambda_{y_o} [V\sin\beta - V_T \cos\gamma_T] +$$

$$\lambda_{E_1} (T-D_o)V/W + 1 \tag{2.37}$$

The solution for L_{22} is analytic, and is given by

$$L_{22} = \sqrt{-\ qs\ W\ H_1(E,h,\beta)\ /VK\lambda_{E_1}}\ .\ \text{sign}\ (\beta_o-\beta) \tag{2.38}$$

After performing the minimization in (2.36), the heading costate variable is computed using

$$\lambda_{\beta_2} = -2\ H_1(E,h,\beta)\ mV/L_{22}\Big|_{h = h_2} \tag{2.39}$$

The calculations in (2.36-2.39) must be performed on line. To accelerate the minimization in (2.36), which is performed each time the control solution is updated, the solution from the previous time instant is used as a starting point.

Numerical results for the F-8 aircraft are given in Figures 3 and 4. These display L_{22} and h_2, respectively, as functions of $\Delta\beta = \beta_o-\beta$ for several values of E. It can be seen from the figures that, at all energy levels, $L_{22} \to 0$ and $h_2 \to h_1$ as $\Delta\beta \to 0$. This type of asymptotic behavior is necessary for a valid singular perturbation solution. Note also that at higher energies, h_2 does not digress very far from h_1 and that L_{22} even for large heading errors, is significantly below L_{max}. This indicates that, at these higher energies, the zero-order solution attempts to preserve the combination of energy rate and closure rate from the first boundary layer solution. At low energy levels the situation is considerably different, with emphasis placed on rapidly reducing heading error. Horizontal lift is saturated before $\Delta\beta$ reaches 1.2 rad. For larger heading errors, h_2 increases so that the

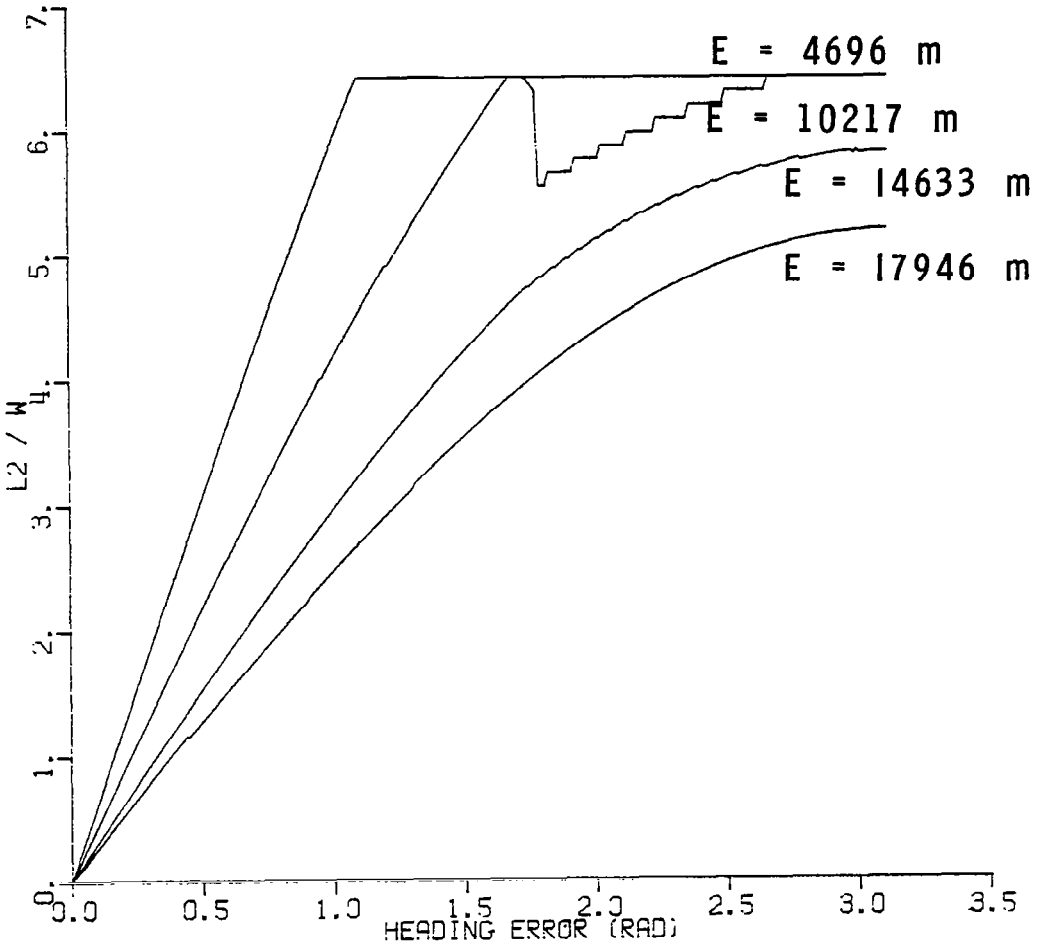

Figure 3. Normalized second boundary layer horizontal lift as a function of heading error for several energy levels.

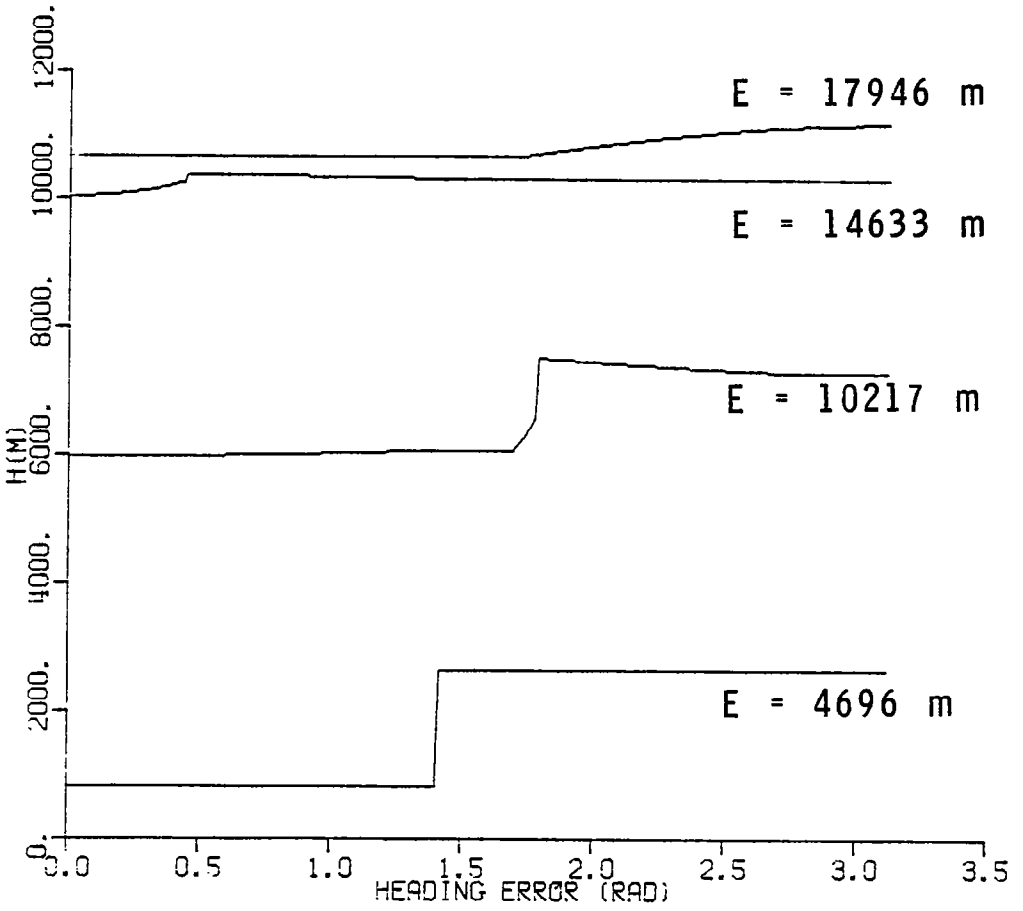

Figure 4. Second boundary layer altitude solution as a function of heading error for several energy levels.

aircraft is driven to the corner velocity for that energy level. At a midrange energy, priorities are more evenly mixed. The solution for h_2 remains close to h_1 longer than in the low energy case. Also note that L_{22} can take on both saturated and nonsaturated values after encountering the maximum lift constraint boundary. These results illustrate the trade-off between energy rate, closure rate and turn rate that takes place in the second boundary layer solution.

2.5 Third Boundary Layer Solution

The third boundary layer addresses the altitude dynamics. It arises from introducing the time transformation $\tau = t/\varepsilon^3$ and letting $\varepsilon \to 0$. The vertical lift L_{13} for this boundary layer is constrained to be

$$L_{13} = W \cos \gamma \tag{2.40}$$

Due to non-zero values of γ, the penalty term $k \sin^2 \gamma$ in (2.12) has an effect on the solution for the third and fourth boundary layers. The controls here are horizontal lift (L_{23}) and γ. The zero-order solution for L_{23} is given by

$$L_{23} = \min \{L_{2max}, L_{22}/\cos \gamma\} \tag{2.41}$$

where

$$L_{2max} = \sqrt{L_{max}^2 - L_{13}^2} \tag{2.42}$$

It can be seen that $L_{23} \to L_{22}$ as $\gamma \to 0$ which is the constrained value for γ in the second boundary layer. The expression for γ_3 is

$$\gamma_3 = \arg \max_{\gamma} \{\sin \gamma / H_2(h,E,\beta,\gamma)\} \cdot \text{sign}\ (h_2 - h) \tag{2.43}$$

where H_2 is the second boundary layer Hamiltonian evaluated at the current conditions for its arguments:

$$H_2(h,E,\beta,\gamma) = (\lambda_{x_o} \cos\beta + \lambda_{y_o} \sin\beta) V \cos \gamma - \lambda_{y_o} V_T \cos \gamma_T$$

$$+ \lambda_{E_1} (T-D)V/W + \lambda_{\beta_2} L_{23}\, g/WV \cos \gamma + 1 + k\sin^2\gamma \tag{2.44}$$

Numerical results for γ_3 as a function of altitude error for zero heading error is shown in Figure 5. The effect of the parameter k is also shown. Note that $\gamma_3 \to 0$ as $h_2 \to h_1$ and that, as might be expected, increasing k decreases the magnitude of γ_3 at all flight conditions. The costate for this boundary layer λ_{h_3} is determined from

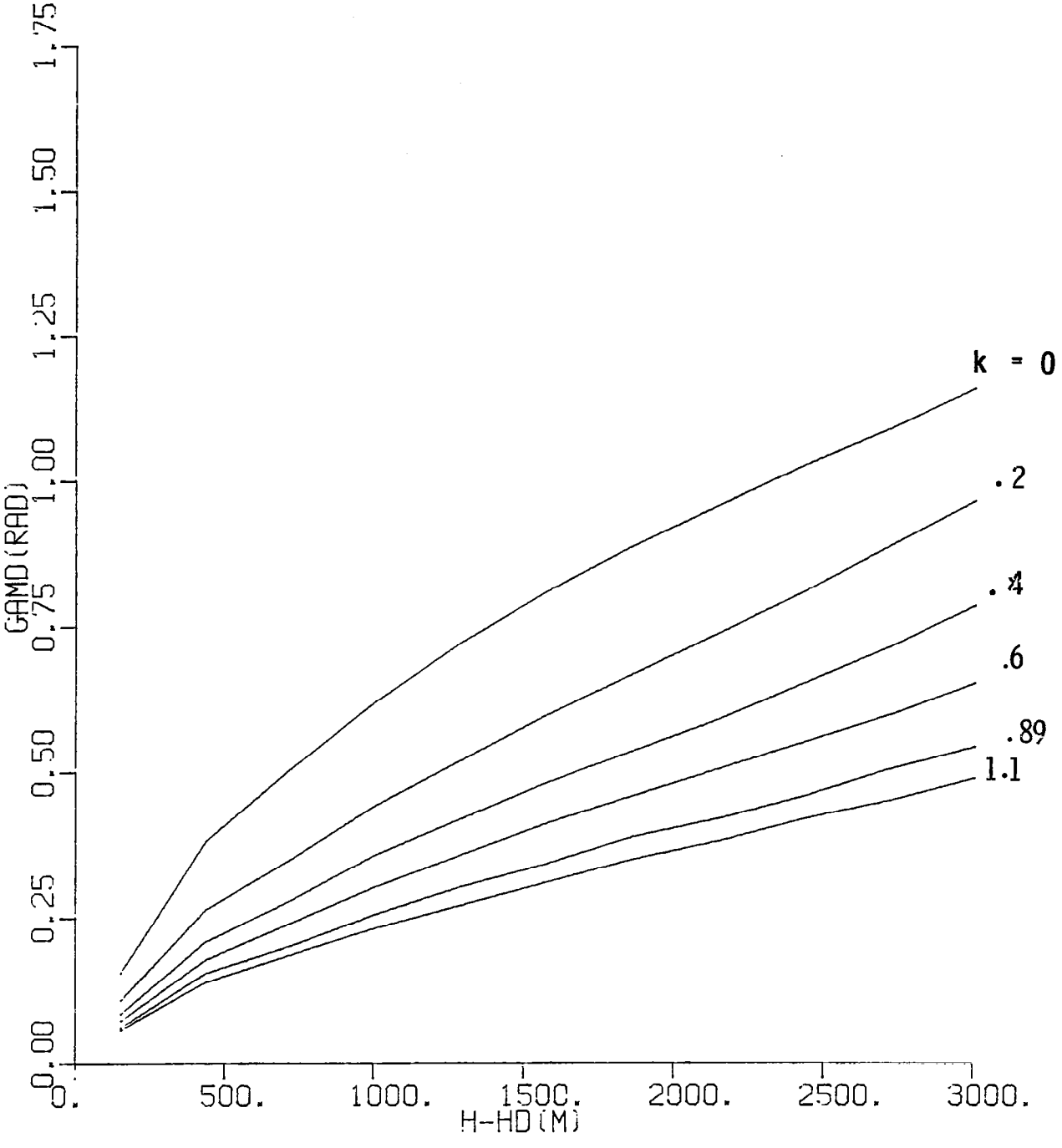

Figure 5. Third boundary layer solution for flight path angle versus altitude error for E = 11320 m.

$$\lambda_{h_3} = - H_2(h,E,\beta,\gamma_3)/V \sin \gamma_3 \tag{2.45}$$

2.6 Fourth Boundary Layer Solution

In the fourth boundary layer, the vertical and horizontal components of lift (L_{14} and L_{24}, respectively) are refined to reflect the flight path angle dynamics. As long as $L \leq L_{max}$, the lift components are:

$$L_{14} = W \cos \gamma - H_3(h,E,\beta,\gamma) qsW/\lambda_{E_1} KV^2 \cos \gamma \tag{2.46}$$

$$L_{24} = \lambda_{\beta_2} gqs/2\lambda_{E_1} KV^2 \cos \gamma \tag{2.47}$$

These are used to define the final lift and bank angle commands:

$$L = \sqrt{L_{14}^2 + L_{24}^2} \tag{2.48}$$

$$\mu = \tan^{-1} (L_{24}/L_{14}) \tag{2.49}$$

If L in (2.48) exceeds L_{max}, we set $L = L_{max}$ and obtain an expression for μ:

$$\tan \mu = (\lambda_{\beta_2}/\lambda_{\gamma_4} \cos \gamma) \cdot \text{sign } (\beta_o - \beta) \tag{2.50}$$

In this formulation λ_{γ_4}, the costate for γ, is evaluated as a root of

$$A\lambda_{\gamma_4}^2 + B\lambda_{\gamma_4} + C = 0 \tag{2.51-a}$$

$$A = g^2(L_{max}^2/W^2 - \cos^2\gamma)/V^2 \tag{2.51-b}$$

$$B = 2\Phi \cos \gamma g/V \tag{2.51-c}$$

$$C = (\lambda_{\beta_2} L_{max} g/WV \cos \gamma)^2 - \Phi^2 \tag{2.51-d}$$

$$\Phi = H_1 - \lambda_{E_1} (L_{max}^2 - W^2\cos^2\gamma) KV/qsW + \lambda_{h_3} V \sin \gamma \tag{2.51-e}$$

It is demonstrated in Appendix B that (2.51-a) will always have real roots of opposite sign; thus λ_{γ_4} is chosen such that

$$\text{sign } \{\lambda_{\gamma_4}\} = - \text{sign } \{\gamma_3 - \gamma\} \tag{2.52}$$

Given this value for λ_{γ_4}, μ is computed using (2.53) placing μ in the quadrant appropriate to sign $\{\gamma_3-\gamma\}$.

It should be noted that the arbitrary separation of h and γ dynamics in the third and fourth boundary layers fails to account for the coupling that naturally exists between these states. A method is given in Appendix D for choosing k in (2.12) so that this problem is alleviated.

SECTION 3

FEEDBACK IMPLEMENTATION

This section describes the feedback implementation of the control solution formed from the singular perturbation outer and boundary layer solutions described in Section 2. Five topics are covered: organization of climb and descent legs, an alternate proportional vertical lift scheme, thrust and lift control during descent, avoidance of singularities in the control solution, and the overall organization of the actual feedback implementation.

3.1 Climb and Descent Legs

Long range intercept trajectories, ignoring initial turning and other transients, have three stages. The first stage is a climb to cruise at the long range optimal cruise energy (E_o^*). The second stage is a cruise leg. The third stage can take one of two forms. If the target altitude is below the altitude for long range cruise, it is a descent leg. It is important to note that climb and descent in this report refer to gain and loss of <u>energy</u> - not <u>altitude</u>. For example, altitude decreases during a portion of the climb profile. If the target altitude is above the long range cruise altitude, the terminal stage is a zoom climb (constant energy altitude gain) maneuver.

Short range intercepts are defined as occurring when the intercept range is less than the range required to fly a long range climb and descent. In this case, the optimal trajectory would consist of climb and descent that meet at an energy level less than E_o^* at an altitude and velocity on the zero-energy-rate boundary for $T = T_{max}$, or on the dynamic pressure or Mach constraint boundary (see Fig. 1). Henceforth, these lower energy points will be referred to as pseudo cruise points, E_o.

An important element in the control design is the decision logic required for determining whether an intercept path is long or short range. In the short range case, the logic must select a pseudo cruise energy level such that the horizontal range for climb and descent matches the predicted intercept range. In the long range case, E_o^* is used and a cruise leg is inserted to match the predicted range to intercept. Descent is initiated when the horizontal range for descent from E_o matches the predicted range to intercept.

As was mentioned in Section 2, the climb, cruise and descent solutions are independent of intercept geometry and target parameters. The calculations are performed off-line, and the results stored in the form $h_c(E,E_o)$ for climb and $h_d(E)$ for descent, where E_o represents selected pseudo cruise energy levels. For the long range case we have $h_c(E,E_o^*)$. Several climb altitude profiles for the F-8 aircraft are illustrated in Figure 6. The descent profile is independent of the selected cruise energy because satisfaction of (2.31) for h_d results in values on the dynamic pressure boundary.

The time, $t_c(E,E_o)$, and horizontal distance, $r_c(E,E_o)$, required to climb from E to E_o were determined by computing the integrals:

$$t_c(E,E_o) = \int_E^{E_o} (1/\dot{E})dE \tag{3.1}$$

$$r_c(E,E_o) = \int_E^{E_o} (V_1/\dot{E})dE \tag{3.2}$$

where

$$V_1 = \sqrt{(E-h_1(E,E_o))2g} \tag{3.3}$$

and $\dot{E}$ is the energy rate computed at $h_c(E,E_o)$. Tabular data for $h_c(E,E_o)$, $t_c(E,E_o)$ and $r_c(E,E_o)$ is presented in Table 1 for E_o^* and several pseudo cruise energies.

The expressions used in calculating altitude and range for descent are slightly different from those used in calculating altitude and range for climb, since in descent, flight path angle is too large to be ignored. We have:

$$t_d(E) = \int_{E_o^*}^{E} (1/\dot{E})dE \tag{3.4}$$

$$r_d(E) = \int_{E_o^*}^{E} (\dot{r}_d/\dot{E})dE \tag{3.5}$$

where

$$\dot{r}_d = V_1 \cos \gamma_d \tag{3.6}$$

$$V_1 = \sqrt{[E-h_d(E)]2g} \tag{3.7}$$

$$\gamma_d = \sin^{-1}\{(dh_d/dE)\dot{E}/V_1\} \tag{3.8}$$

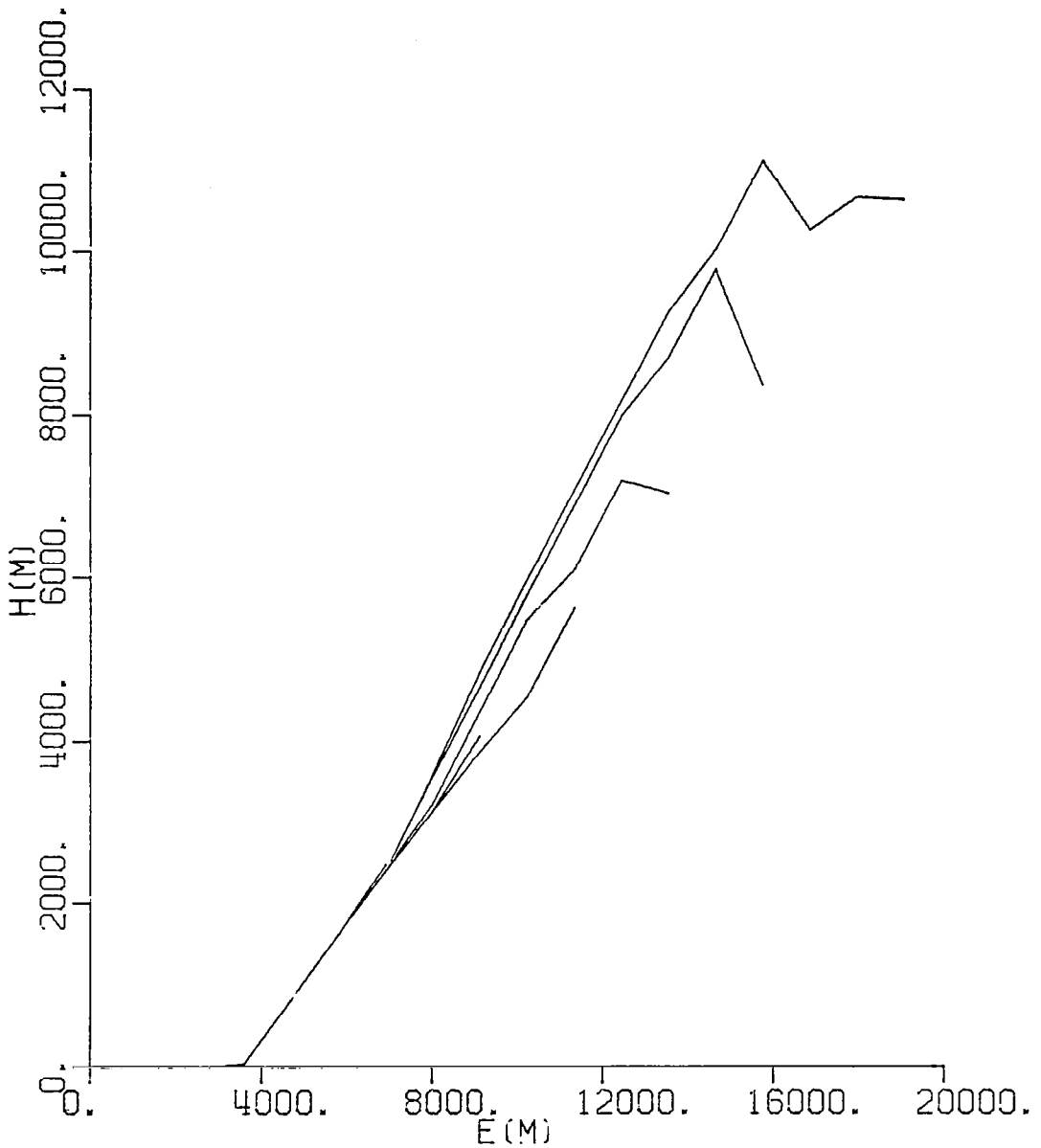

Figure 6. Several climb altitude profiles for the F-8 aircraft.

TABLE 1

F-8 CLIMB ALTITUDE, TIME AND RANGE
AS FUNCTIONS OF ENERGY

ASCENT VARIABLES, CRUISE ENERGY= 4696.05 M

ENERGY(M)	H(M)	TIME(SEC)	RANGE(M)
279.45	0.0	55.0058	10342.0
1383.60	0.0	34.4565	7888.8
2487.75	0.0	21.4960	5389.9
3591.90	30.48	10.4930	2720.8
4696.05	820.36	0.0	0.0
5800.20	0.0	0.0	0.0
6904.35	0.0	0.0	0.0
8008.50	0.0	0.0	0.0
9112.65	0.0	0.0	0.0
10216.80	0.0	0.0	0.0
11320.95	0.0	0.0	0.0
12425.10	0.0	0.0	0.0
13529.25	0.0	0.0	0.0
14633.39	0.0	0.0	0.0
15737.55	0.0	0.0	0.0
16841.70	0.0	0.0	0.0
17945.85	0.0	0.0	0.0
19049.99	0.0	0.0	0.0

ASCENT VARIABLES, CRUISE ENERGY= 6904.35 M

ENERGY(M)	H(M)	TIME(SEC)	RANGE(M)
279.45	0.0	76.8073	16350.4
1383.60	0.0	56.2579	13897.2
2487.75	0.0	43.2975	11398.3
3591.90	30.48	32.2945	8729.2
4696.05	822.96	21.8001	6009.3
5800.20	1615.44	11.1350	3118.5
6904.35	2477.75	0.0	0.0
8008.50	0.0	0.0	0.0
9112.65	0.0	0.0	0.0
10216.80	0.0	0.0	0.0
11320.95	0.0	0.0	0.0
12425.10	0.0	0.0	0.0
13529.25	0.0	0.0	0.0
14633.39	0.0	0.0	0.0
15737.55	0.0	0.0	0.0
16841.70	0.0	0.0	0.0
17945.85	0.0	0.0	0.0
19049.99	0.0	0.0	0.0

TABLE 1 (CONTINUED)

ASCENT VARIABLES, CRUISE ENERGY= 9112.65 M

ENERGY(M)	H(M)	TIME(SEC)	RANGE(M)
279.45	0.0	107.9332	25825.6
1383.60	0.0	87.3839	23372.3
2487.75	0.0	74.4234	20873.4
3591.90	30.48	63.4204	18204.4
4696.05	822.96	52.9260	15484.5
5800.20	1615.44	42.2609	12593.7
6904.35	2407.92	31.1056	9437.3
8008.50	3139.44	17.7964	5471.5
9112.65	4065.64	0.0	0.0
10216.80	0.0	0.0	0.0
11320.95	0.0	0.0	0.0
12425.10	0.0	0.0	0.0
13529.25	0.0	0.0	0.0
14633.39	0.0	0.0	0.0
15737.55	0.0	0.0	0.0
16841.70	0.0	0.0	0.0
17945.85	0.0	0.0	0.0
19049.99	0.0	0.0	0.0

ASCENT VARIABLES, CRUISE ENERGY= 11320.95 M

ENERGY(M)	H(M)	TIME(SEC)	RANGE(M)
279.45	0.0	194.4020	54474.5
1383.60	0.0	173.8526	52021.2
2487.75	0.0	160.8922	49522.3
3591.90	30.48	149.8892	46853.3
4696.05	822.96	139.3948	44133.4
5800.20	1615.44	128.7297	41242.6
6904.35	2407.92	117.5744	38086.2
8008.50	3139.44	104.2652	34120.5
9112.65	3870.96	84.9084	28070.4
10216.80	4541.52	51.5031	17163.0
11320.95	5626.88	0.0	0.0
12425.10	0.0	0.0	0.0
13529.25	0.0	0.0	0.0
14633.39	0.0	0.0	0.0
15737.55	0.0	0.0	0.0
16841.70	0.0	0.0	0.0
17945.85	0.0	0.0	0.0
19049.99	0.0	0.0	0.0

TABLE 1 (CONTINUED)

ASCENT VARIABLES, CRUISE ENERGY= 13529.25 M

ENERGY(M)	H(M)	TIME(SEC)	RANGE(M)
279.45	0.0	237.1549	67539.1
1383.60	0.0	216.6056	65085.9
2487.75	0.0	203.6451	62586.9
3591.90	30.48	192.6421	59917.9
4696.05	822.96	182.1478	57198.0
5800.20	1615.44	171.4827	54307.2
6904.35	2407.92	160.3274	51150.8
8008.50	3230.88	147.3731	47332.3
9112.65	4358.64	131.9121	42741.9
10216.80	5486.40	114.7642	37635.2
11320.95	6096.00	92.6095	30741.9
12425.10	7193.28	62.4630	21150.7
13529.25	7034.38	0.0	0.0
14633.39	0.0	0.0	0.0
15737.55	0.0	0.0	0.0
16841.70	0.0	0.0	0.0
17945.85	0.0	0.0	0.0
19049.99	0.0	0.0	0.0

ASCENT VARIABLES, CRUISE ENERGY= 15737.55 M

ENERGY(M)	H(M)	TIME(SEC)	RANGE(M)
279.45	0.0	275.9463	78177.2
1383.60	0.0	255.3971	75724.0
2487.75	0.0	242.4366	73225.1
3591.90	30.48	231.4336	70556.0
4696.05	822.96	220.9393	67836.1
5800.20	1615.44	210.2742	64945.3
6904.35	2407.92	199.1189	61789.0
8008.50	3566.16	187.1362	58435.7
9112.65	4663.44	173.9817	54709.5
10216.80	5791.20	159.2435	50510.3
11320.95	6888.48	142.5676	45719.5
12425.10	7985.76	123.3140	40147.4
13529.25	8717.28	99.3018	32953.4
14633.39	9784.08	68.3067	23472.8
15737.55	8370.48	0.0	0.0
16841.70	0.0	0.0	0.0
17945.85	0.0	0.0	0.0
19049.99	0.0	0.0	0.0

TABLE 1 (CONCLUDED)

ASCENT VARIABLES, CRUISE ENERGY= 19049.99 M

ENERGY(M)	H(M)	TIME(SEC)	RANGE(M)
279.45	0.0	628.5549	210690.6
1383.60	0.0	608.0056	208237.4
2487.75	0.0	595.0452	205738.5
3591.90	30.48	584.0422	203065.4
4696.05	822.96	573.5481	200349.5
5800.20	1615.44	562.8831	197458.7
6904.35	2407.92	551.7278	194302.4
8008.50	3596.64	539.8125	190987.3
9112.65	4846.32	527.1221	187502.6
10216.80	5974.08	513.2688	183662.9
11320.95	7071.36	497.5857	179272.1
12425.10	8168.64	479.4856	174160.9
13529.25	9265.92	458.2539	168122.7
14633.39	10027.92	431.6506	160315.6
15737.55	11125.20	397.0964	149984.7
16841.70	10271.76	343.9612	132477.7
17945.85	10668.00	244.0769	95683.5
19049.99	10636.09	0.0	0.0

where E is the energy at initiation of descent. Tabular values for $h_d(E)$, $t_d(E)$ and $r_d(E)$ are provided in Table 2. Climb times and ranges from the current energy to the cruise energy are obtained by interpolating and differencing the values in Table 1. A similar procedure is used for descent using Table 2. For example,

$$t_d(E_c,E_f) = t_d(E_f) - t_d(E_c) \tag{3.9}$$

$$r_d(E_c,E_f) = r_d(E_f) - r_d(E_c) \tag{3.10}$$

In general, E_f is not known a priori and must be determined such that $h(t_f) = h_T(t_f)$. A terminal constraint must be satisifed:

$$h_d(E_f) = h_T + V_T \sin \gamma_T \, t_{go} \tag{3.11}$$

where t_{go} is the estimated time remaining until intercept. Referring to Figure 1, we initiate descent when

$$r_d(E_o,E_f) \cos (\beta_o-\lambda) \geq R + (V_T \cos \gamma_T \sin \lambda) t_d(E_o,E_f) \tag{3.12}$$

is satisfied, where R is the current horizontal range.

3.2 Proportional Vertical Lift

An option was included in the control logic for stopping the singular perturbation solution after the second boundary layer, and using a suboptimal proportional control for vertical lift. We first define a desired flight path angle

$$\gamma_D = (h_2-h)/\tau_1 V + \dot{E}\,(dh_1/dE)/V_1 \,, \quad V_1 = \sqrt{(E-h_1)2g} \tag{3.13}$$

The second term in (3.13) is an approximation to the flight path angle for following the first boundary layer climb path. The proportional vertical lift (L_{1p}) is computed based on a desired flight path angle rate proportional to $(\gamma_D-\gamma)$:

$$\dot{\gamma}_D = (\gamma_D-\gamma)/\tau_2 = (L_{1p}-W\cos\gamma)/mV \tag{3.14}$$

Solving for L_{1p} we have

$$L_{1p} = mV(\gamma_D-\gamma)/\tau_2 + W\cos\gamma \tag{3.15}$$

TABLE 2

F-8 DESCENT ALTITUDE, TIME AND RANGE
AS FUNCTIONS OF ENERGY

DESCENT VARIABLES, CRUISE ENERGY= 19100.07 M

ENERGY(M)	H(M)	TIME(SEC)	RANGE(M)
3586.93	0.0	357.6738	107306.4
4499.47	677.40	270.8616	83918.9
5412.00	1331.60	198.3982	63759.6
6324.54	1976.64	143.5021	47992.5
7237.08	2604.15	108.2608	37554.1
8149.62	3212.69	87.5223	31231.0
9062.16	3814.46	74.0457	27015.2
9974.69	4390.52	63.7786	23719.3
10887.23	4957.39	55.3226	20935.3
11799.77	5506.95	48.1671	18520.0
12712.30	6030.09	41.5890	16232.8
13624.85	6553.26	35.1294	13919.1
14537.38	7055.07	28.8112	11585.8
15449.92	7531.21	22.6819	9252.1
16362.46	8006.49	16.7482	6929.9
17275.00	8463.37	10.9957	4614.5
18187.54	8896.07	5.4142	2303.1
19100.07	9317.89	0.0	0.0

The controls L and μ are then computed as

$$L = \sqrt{L_{1p}^2 + L_{22}^2} \tag{3.16}$$

$$\mu = \tan^{-1}(L_{22}/L_{1p}) \tag{3.17}$$

A block diagram of these calculations is given in Figure 7. The characteristic equation for the resulting transfer function is

$$\tau_1\tau_2 s^2 + \tau_1 s + 1 = 0 \tag{3.18}$$

The undamped natural frequency (ω_n) and the damping ratio (ζ) for this second order system are

$$\omega_n = 1/\sqrt{\tau_1\tau_2} \tag{3.19}$$

$$\zeta = \sqrt{\tau_1/2\tau_2} \tag{3.20}$$

The values chosen for the above were $\omega_n = 0.1$ rad/s and $\zeta = 0.8$, respectively. This resulted in values for τ_1 and τ_2 of 15.0 and 6.0 s respectively.

3.3 Thrust and Lift Control During Descent

In the ideal case of a fully optimal control solution, there would be insignificant maneuvering and throttle variation during descent. There is, however, significant turning in the zero order solution implemented. This is primarily due to two factors. First, since the aircraft follows the dynamic pressure constraint boundary during most of the descent, and since the flight-path angle is non-zero, the intercept heading changes from the optimal cruise heading value. Because of this, it is necessary to update the intercept heading during descent using (2.24) and the horizontal component of aircraft velocity. Second, target maneuvers that occur after the initiation of descent necessitate heading changes. The former problem could be greatly reduced by correcting the outer solution to first order in E, in a manner similar to the procedure followed in [16].

In order to insure intercept under all conditions, it is necessary to modulate both thrust and L_{22} during descent. In the case of L_{22} maximum lift should always be used during descent in maintaining the intercept heading, due to the fact that λ_{E_1} in (2.32) becomes positive during descent. In practice, a proportional control law is used

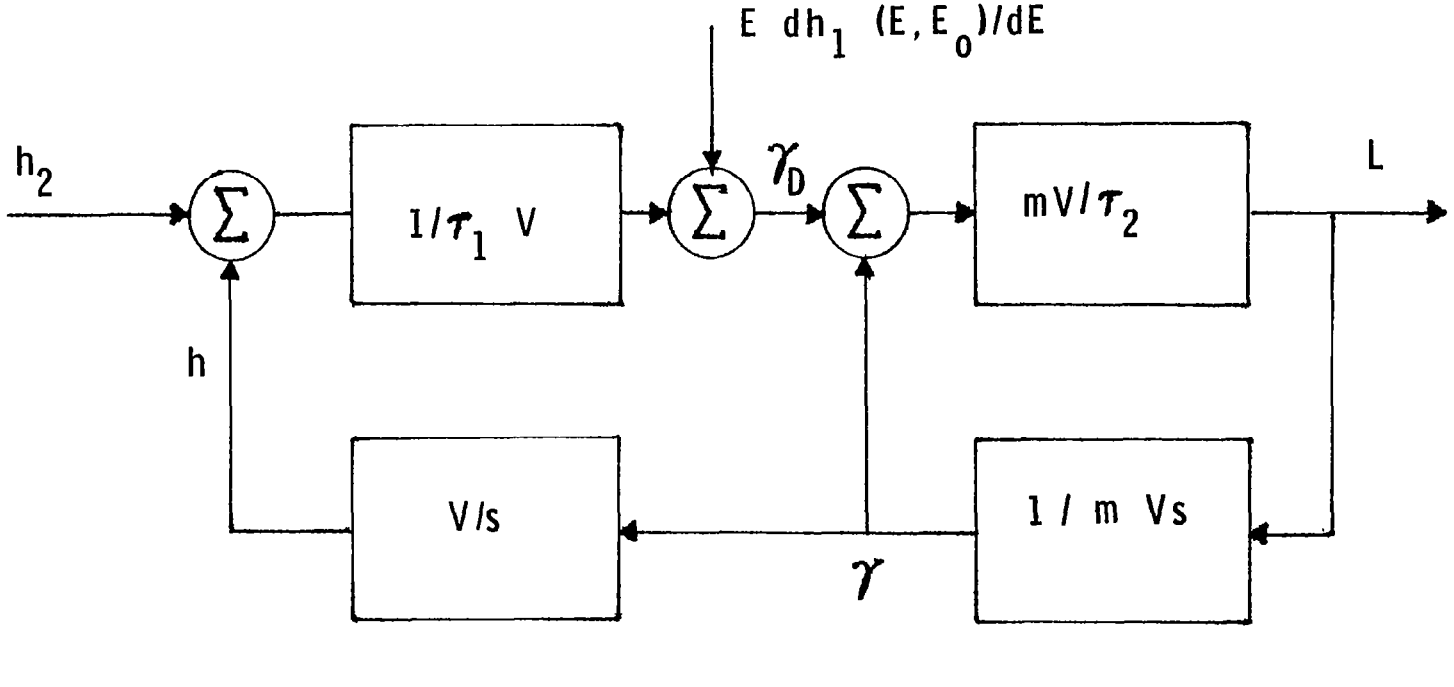

Figure 7. Proportional vertical lift calculations.

for small heading errors.

Thrust modulations are used to control rate of descent to ensure that $h=h_T$ at intercept. Two correction terms are introduced:

$$T = T_d + \delta T_1 + \delta T_2 \tag{3.21}$$

where T_d is the nominal descent thrust from (2.28, 2.29). The second term corrects for the fact that L does not equal W during descent, since this is assumed in generating the t_d and r_d tabular data. Thus, δT_1 compensates for the increased drag due to lift variations.

$$\delta T_1 = K(L^2-W^2)/qs \tag{3.22}$$

The second component compensates for the current mismatch (δR)in range, where from (3.12), replacing E_o by E

$$\delta R = R + (V_T \cos \gamma_T \sin\lambda)t_d(E, E_f)-r_d(E, E_f)\cos(\beta_o-\lambda) \tag{3.23}$$

A proportional control law was derived, defining

$$\dot{\delta R} = -K_3 \delta R \tag{3.24}$$

Noting that

$$\dot{\delta R} = (dr_d(E,E_f)/dE)\cos(\beta_o-\lambda)\dot{\delta E} \tag{3.25}$$

and

$$\dot{\delta E} = \delta T_2 V/W \tag{3.26}$$

one can solve for δT_2 as

$$\delta T_2 = K_3 W\delta R/V\cos(\beta_o-\lambda)(dr_d(E,E_f)/dE) \tag{3.27}$$

In order to allow for thrust variation, T_{min} was set equal to $T_{mil}/2$, where T_{mil} is the military thrust level.

It should be noted that a portion of the descent path calls for $T_d = T_{max}$. Referring to Figure 8, note that upon initiating descent, for $E_o > E_s$, the commanded altitude on the descent path is such that $V_1(E_o) > V_o(E_o)$. As shown in Appendix A, this means that λ_{E_1} remains negative until $V_1(E) < V_o(E_o)$, which from (2.28) implies that $T = T_{max}$.

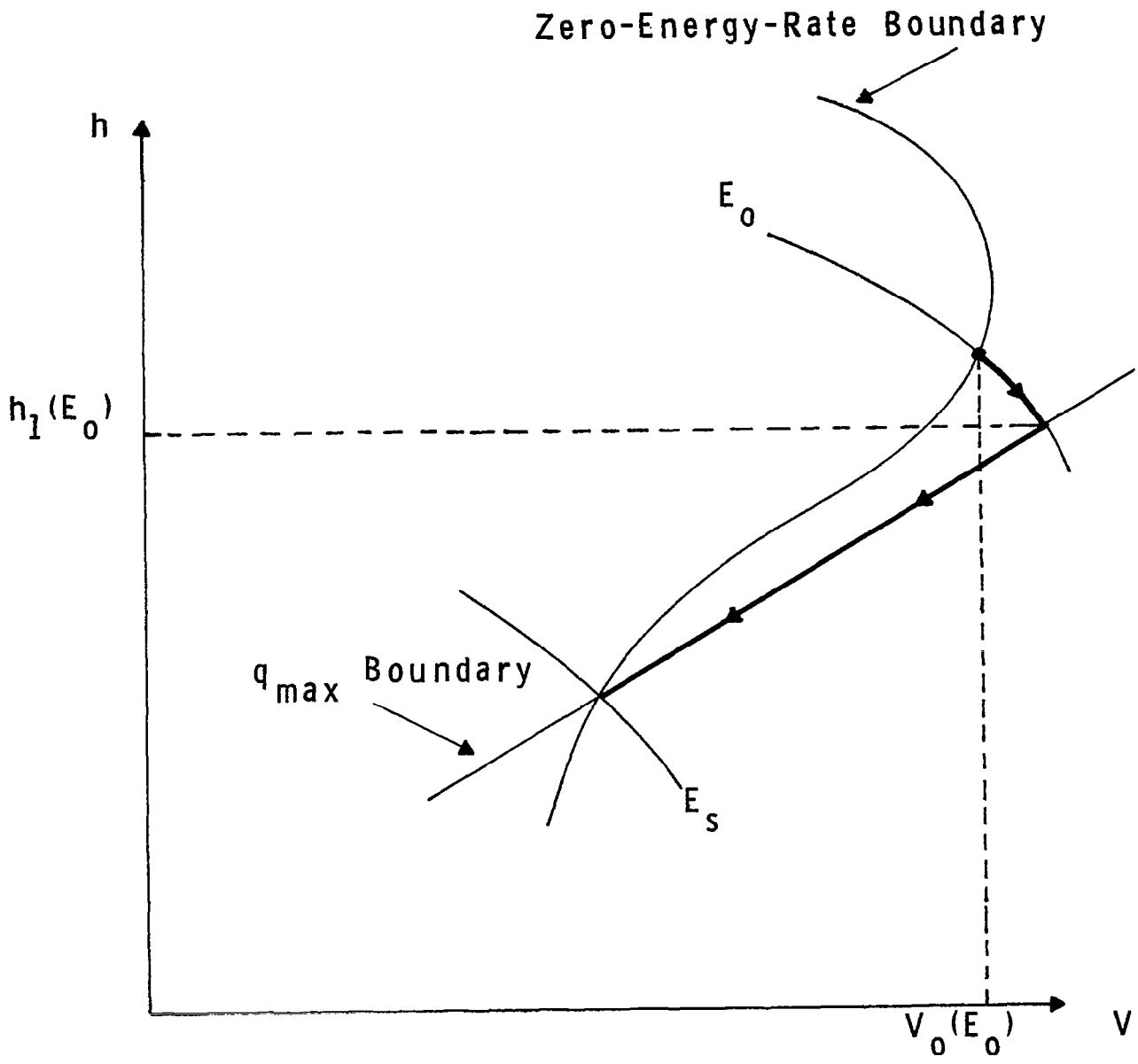

Figure 8. Transition to descent.

3.4 Summary of Control Calculations

A summary of the control calculations including proportional vertical lift is presented in Figure 9. The organization of the additional calculations for the full zero-order solution is given by Figure 10. All on-line calculations are referenced by equation numbers. The purpose of the range matching block is to establish the proper cruise or pseudo cruise energy level, E_o. During climb, the costates are calculated on-line and $h_c(E,E_o)$ is taken from tabular data. All turn parameters are calculated on-line. During descent, $h_d(E,E_f)$ is drawn from tabular data, and thrust and lift are calculated as described in Section 3.3.

3.5 Avoidance of Numerical Singularities

Numerical difficulties evidenced by discontinuities in the control solution were encountered when the aircraft altitude, heading and/or flight path angle approached their optimal values for the second and third boundary layer solutions. These discontinuities occurred when certain functions approached an indeterminate (zero over zero) form as the optimum state values were approached. For example, the argument being minimized in (2.36) approaches an indeterminate form as heading error approaches zero. The corrective measures took the form of first-order Taylor series expansions and approximations taking advantage of the asymptotic character or the boundary layer solutions. A more detailed description is given in Appendix F.

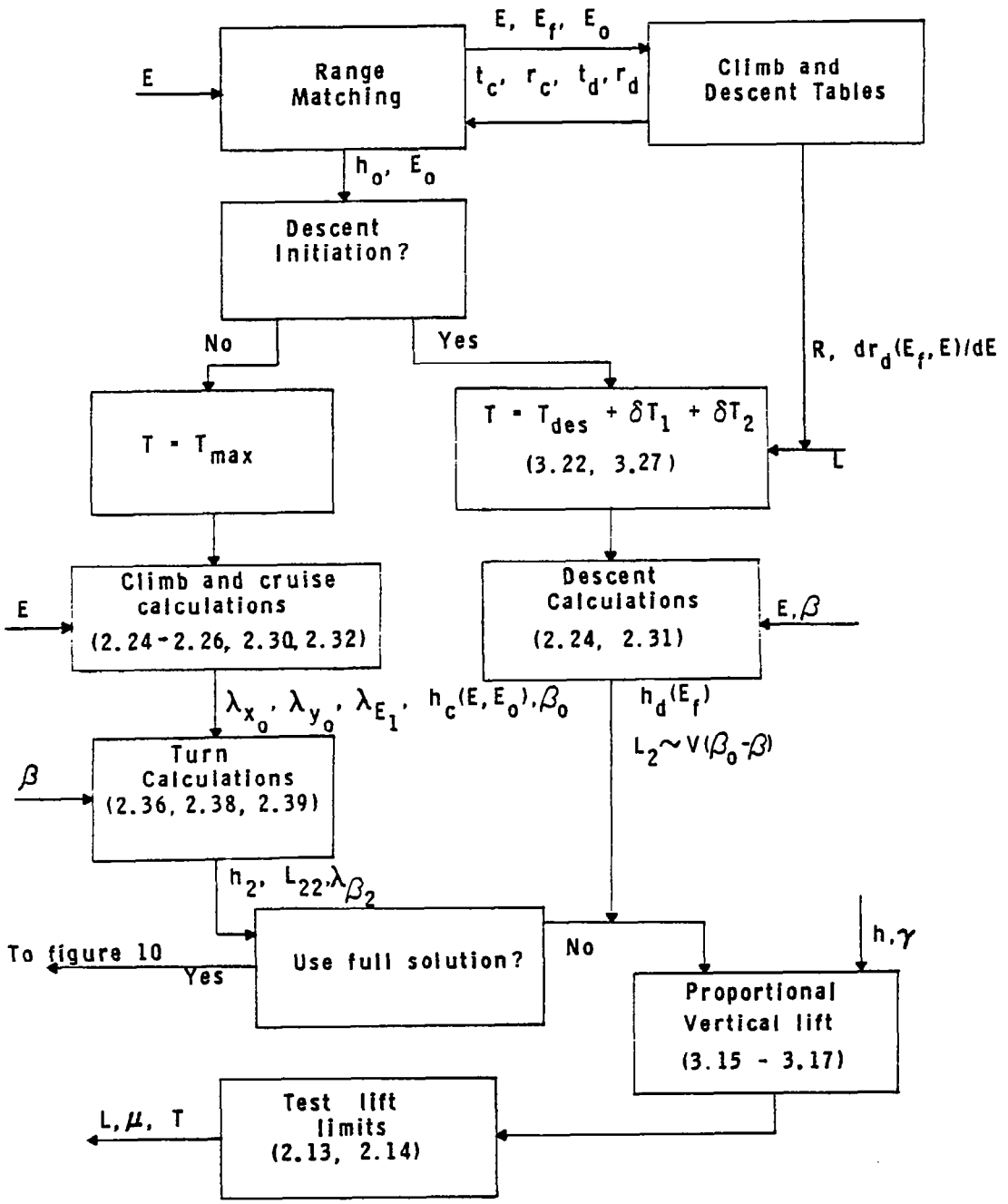

Figure 9. Summary of control calculations with proportional vertical lift.

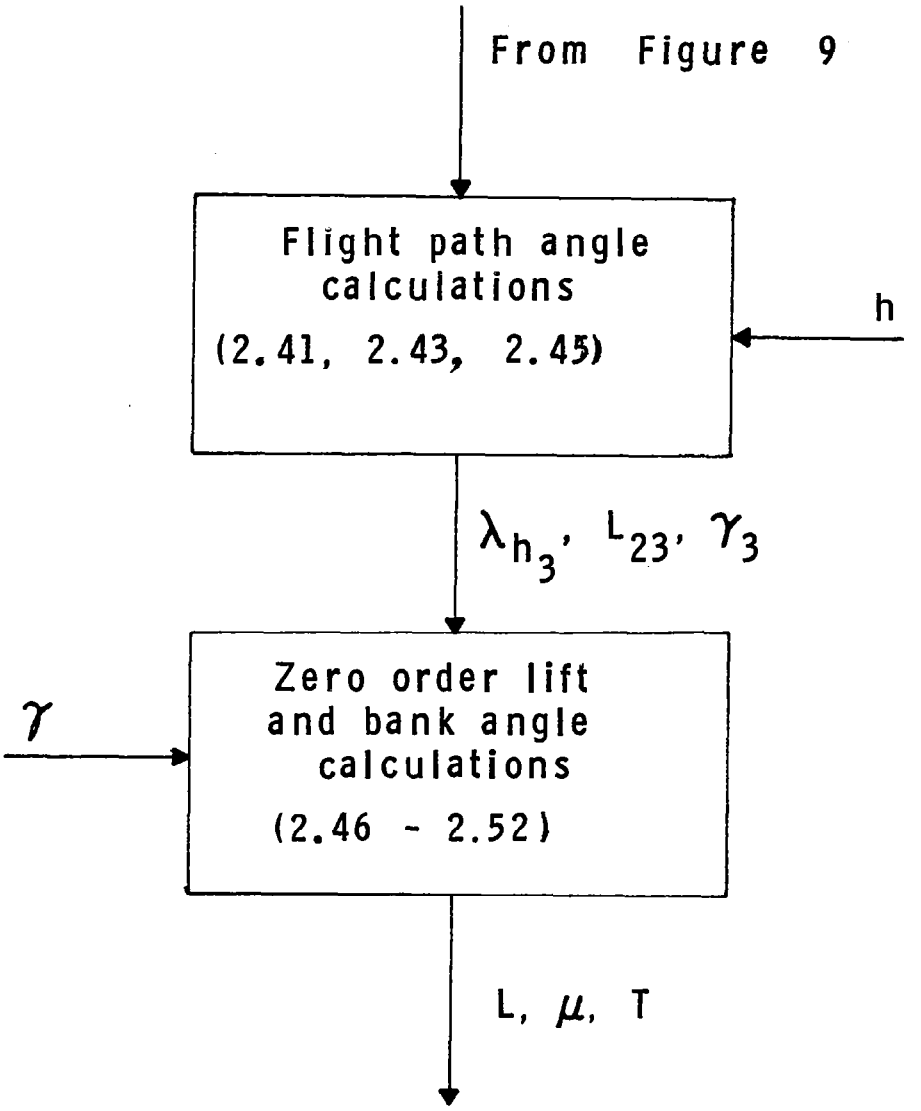

Figure 10. Zero order lift and bank angle calculations.

SECTION 4

POINT-MASS MODEL OF THE F-8 AIRCRAFT

This section describes the procedure by which the F-8 was modelled at trim conditions and presents the results of that effort. The intercept control law has been built on the assumption that the aircraft behaves as a point mass. The aerodynamic model takes the form:

$$D = qs\ C_{D_o} + (\eta/C_{L_\alpha})\ L^2/qs = qs\ C_D \tag{4.1}$$

$$L = qs\ C_{L_\alpha}(\alpha-\alpha_o) \tag{4.2}$$

Thus, implementation of this model for the F-8 required that values of C_{L_α}, C_{D_o} and η be available at trim. These values were generated from the F-8 aerodynamic data in [24] in the manner described below.

First, by linear interpolation of moment data about the pitching axis, elevator deflections corresponding to trim (δ_{e_T}) over a range of angle-of-attack (α) were determined at selected Mach numbers. Next, C_{L_α} was graphically estimated by determining the slope of a straight line passed through points corresponding to C_L as a function of α, again at selected Mach numbers. Since α is small through most of a long range intercept trajectory, the approximation was biased to give greater accuracy to small α. This procedure also resulted in a non-zero "angle-of-attack at zero lift" (α_o). Values of C_{L_α} and α_o as functions of Mach number are shown in Table 3. The graphical C_{L_α} estimates are displayed in Figures 11 through 17. The original drag coefficient data is tabularized as a function of elevator deflection, angle of attack and Mach number. The parameter C_{D_o} was calculated by interpolating the drag coefficient data at trim conditions (δe_T, α_o) for various Mach numbers. Values obtained for C_{D_o} are shown as a function of Mach in Table 3. Finally, η was calculated based on the parabolic drag model in (4.1). Values of $(C_D-C_{D_o})$ were plotted against $(\alpha-\alpha_o)$ on log-log paper and a "best fit" line with a slope of 2.0 was passed through the points, again favoring lower values of α. Then, from values of $(C_D-C_{D_o})$ and $(\alpha-\alpha_o)$ at a point on the line, η was calculated by using (4.2) in (4.1) to eliminate L and solving for η:

$$\eta = (C_D-C_{D_o})/C_{L_\alpha}(\alpha-\alpha_o)^2 \tag{4.3}$$

The plots used in the estimation of η are displayed in Figures 18 to 24. and the resulting values of η are given in Table 3.

TABLE 3

SUMMARY OF F-8 TRIM AERO DATA

MACH	α_o (rad)	C_{L_α}	C_{D_o}	η
.18	.0192	3.366	.0149	.446
.6	.0105	3.518	.0142	.580
.85	.0140	4.09	.0152	.734
.9	.0143	4.29	.0166	.807
.98	.0105	4.18	.0291	.748
1.1	.0105	4.24	.040	.733
1.2	.0105	3.58	.039	.722

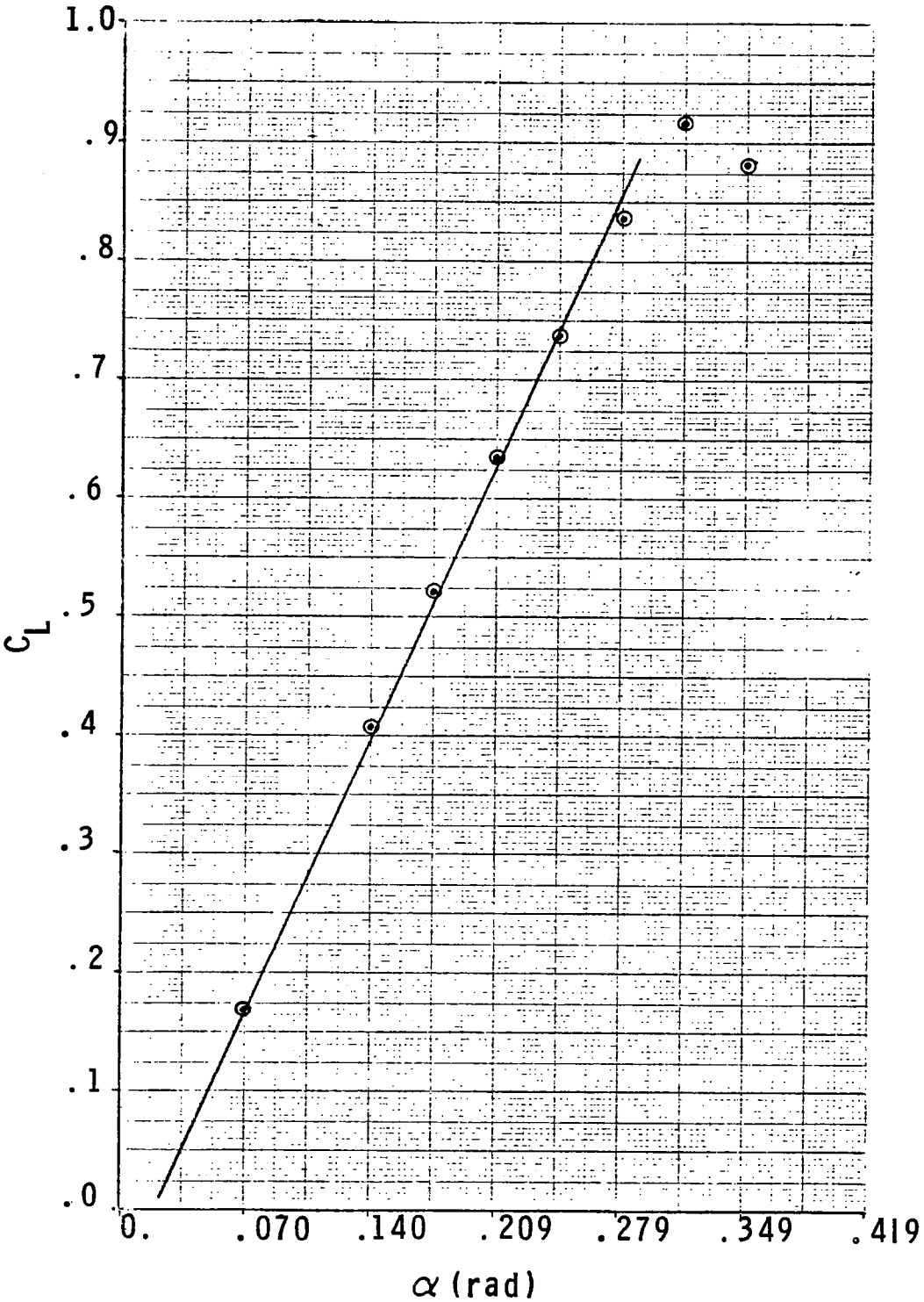

Figure 11. C_L as a function of α for M = 0.18 .

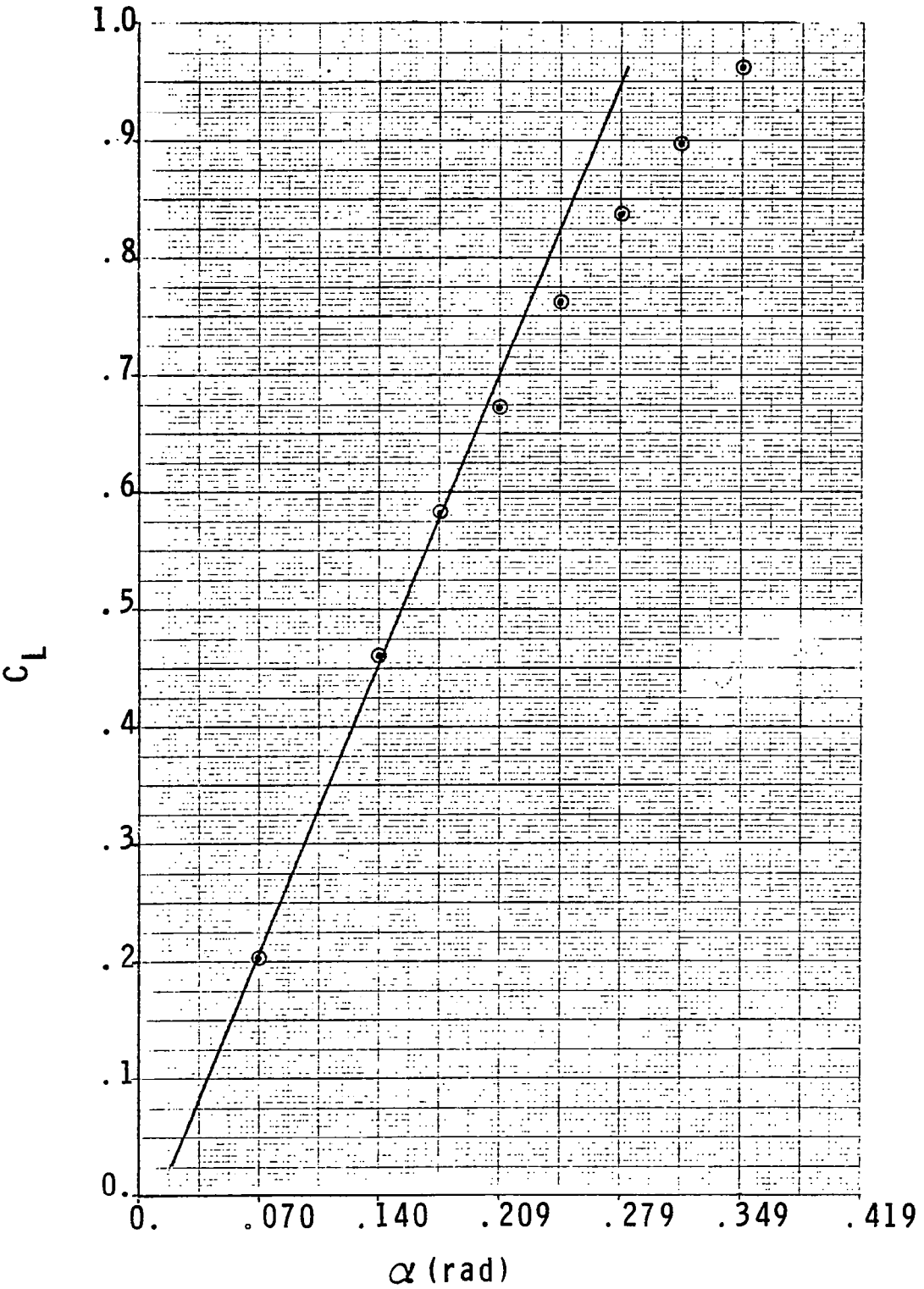

Figure 12. C_L as a function of α for M = 0.6 .

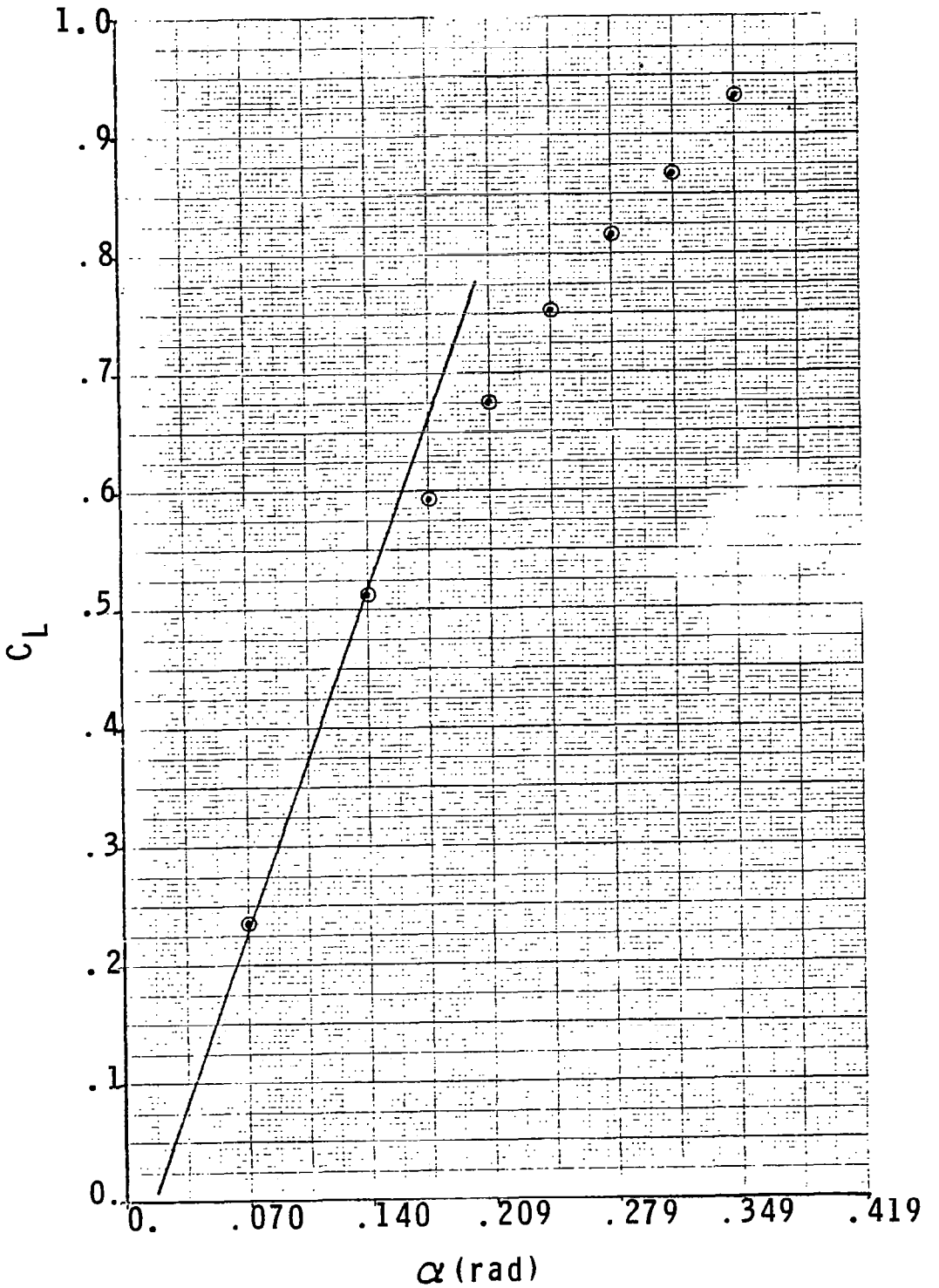

Figure 13. C_L as a function of α for M = 0.85 .

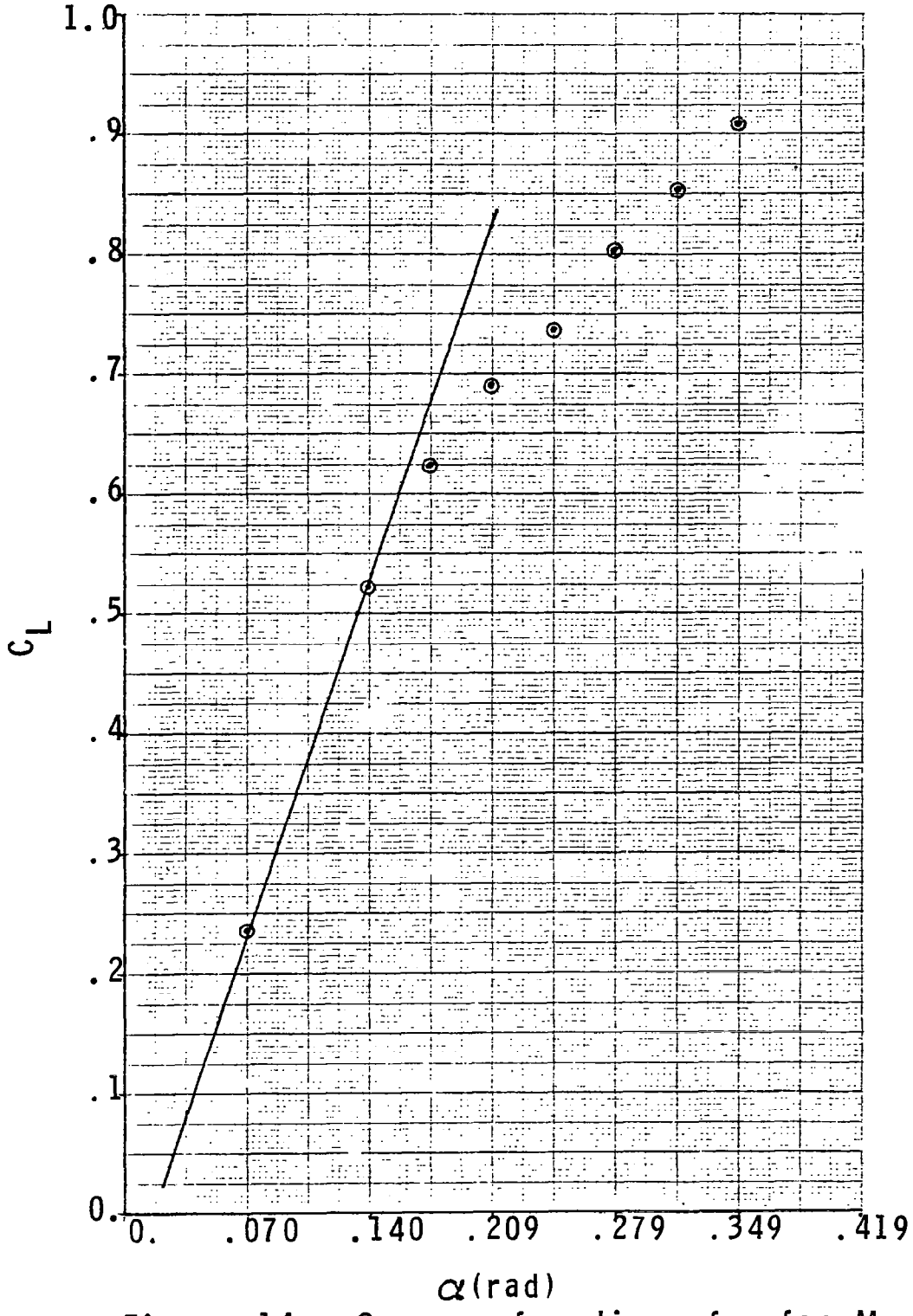

Figure 14. C_L as a function of α for M = 0.9 .

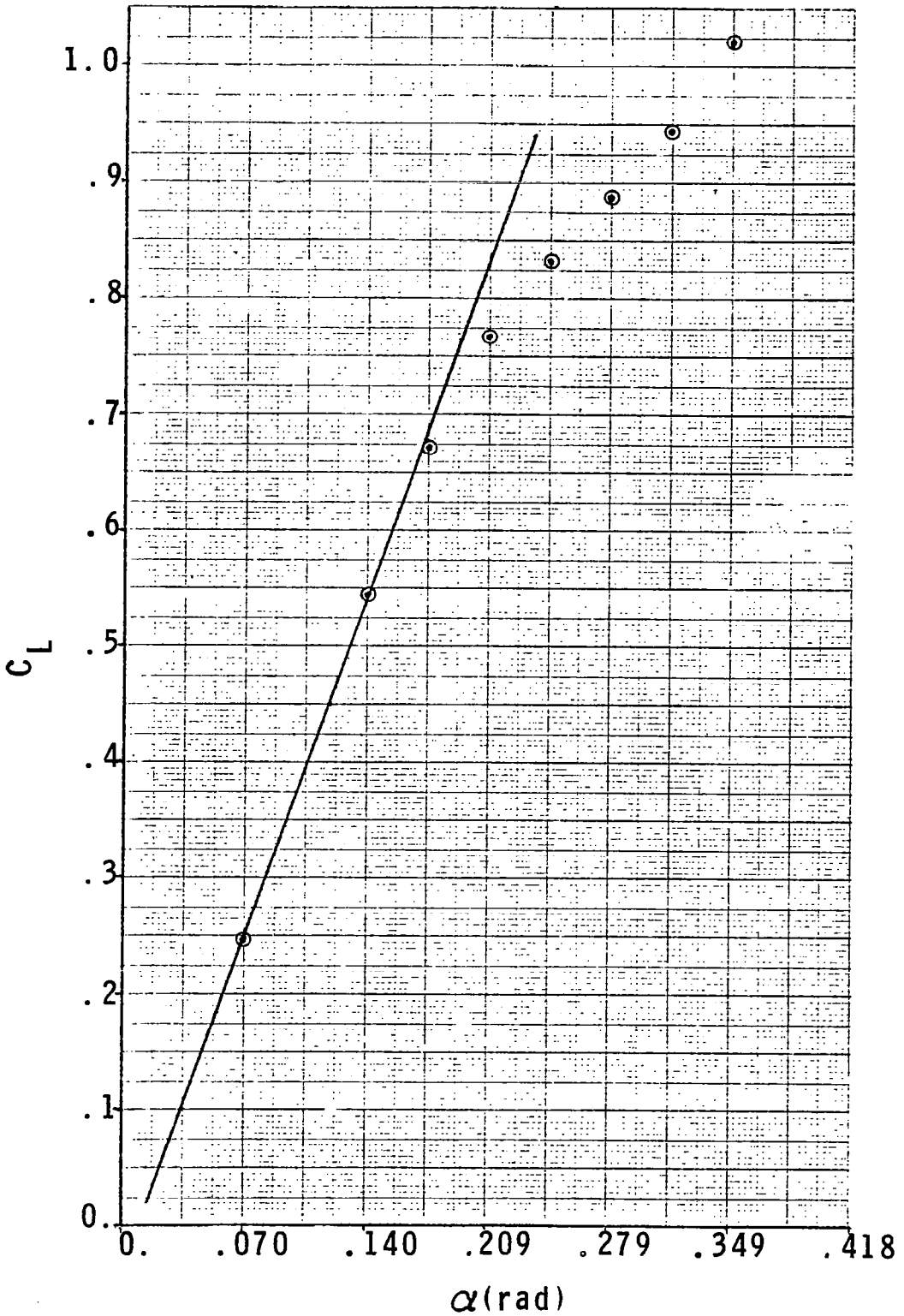

Figure 15. C_L as a function of α for M = 0.98 .

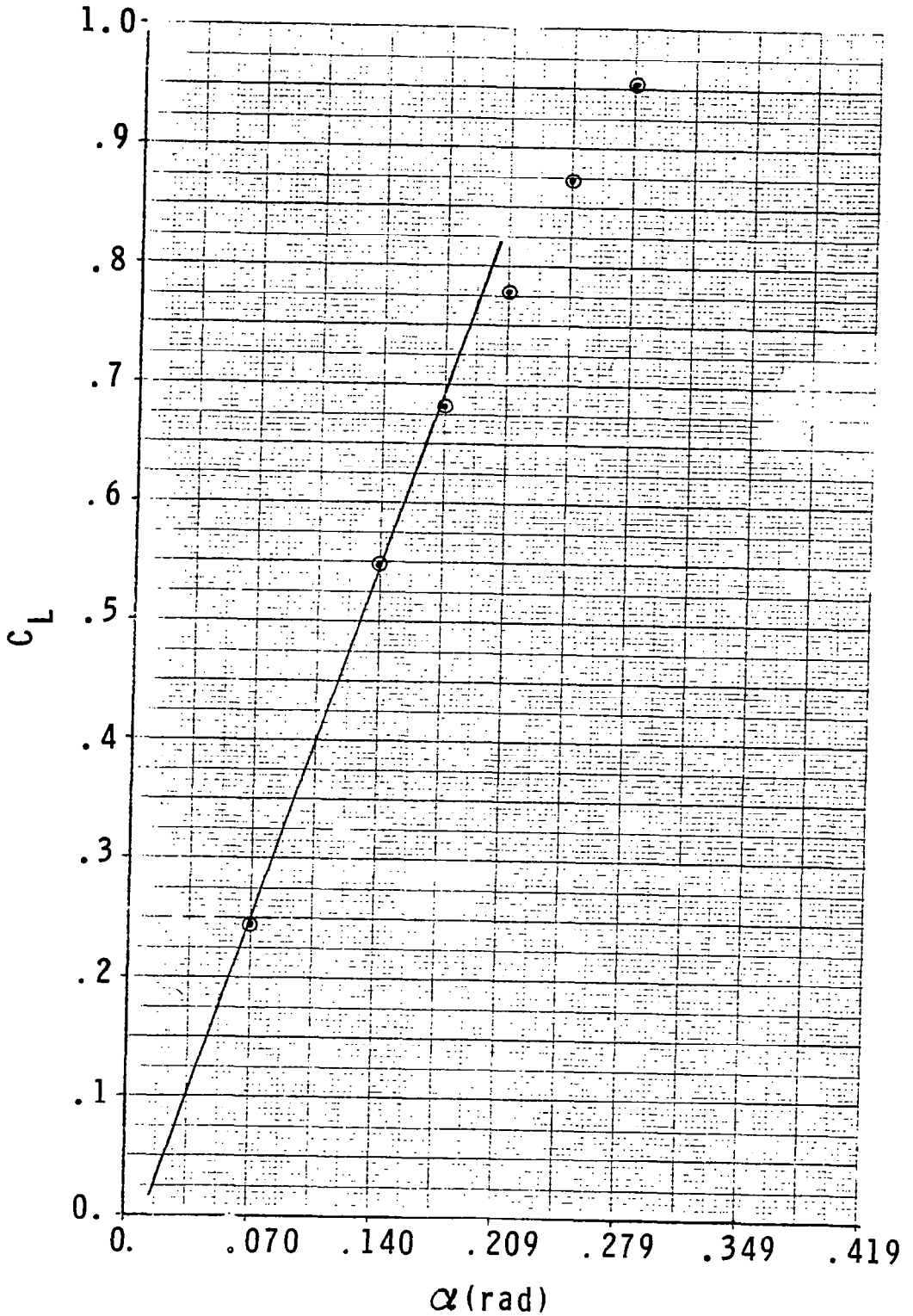

Figure 16. C_L as a function of α for M = 1.1 .

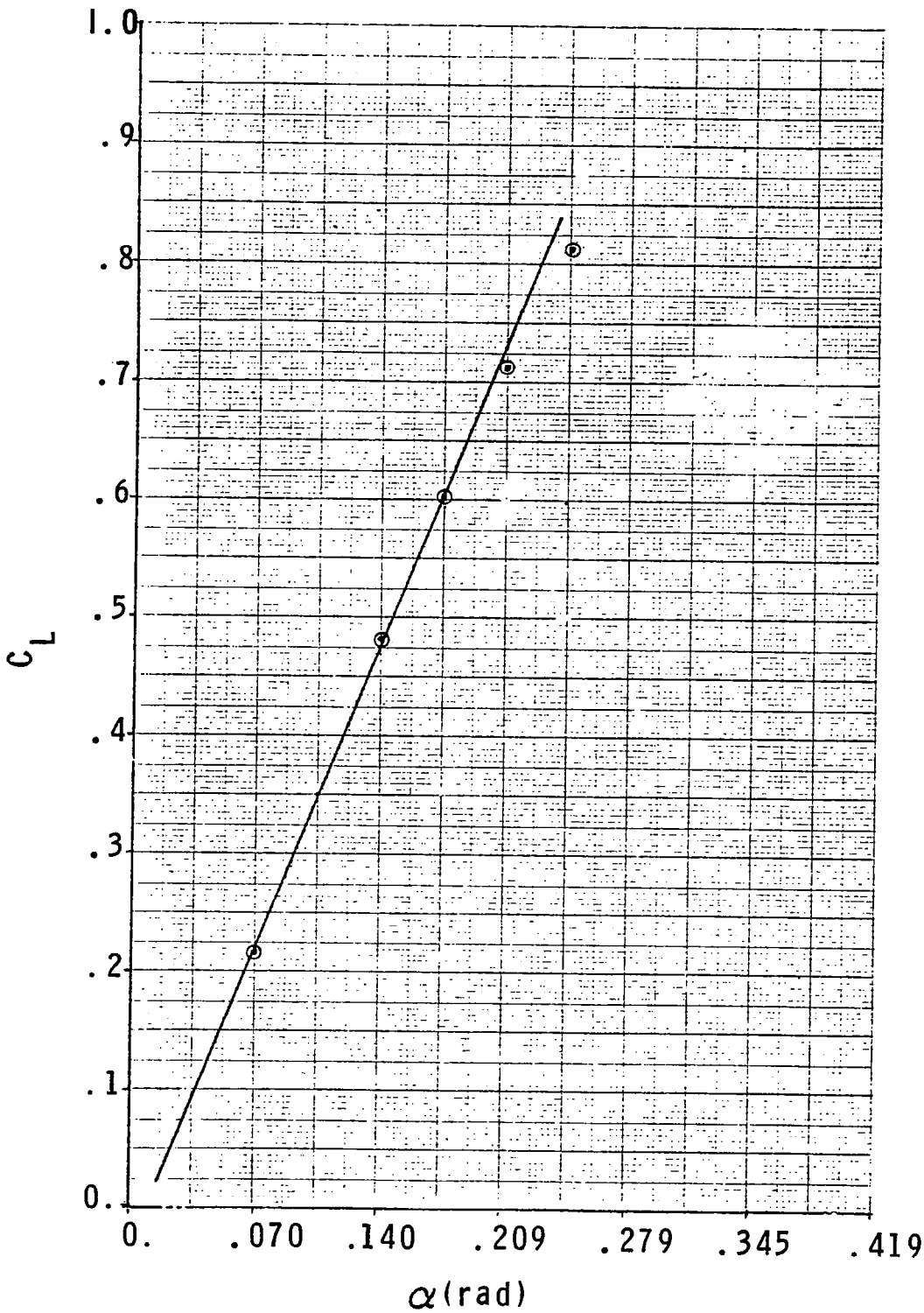

Figure 17. C_L as a function of α for M = 1.2 .

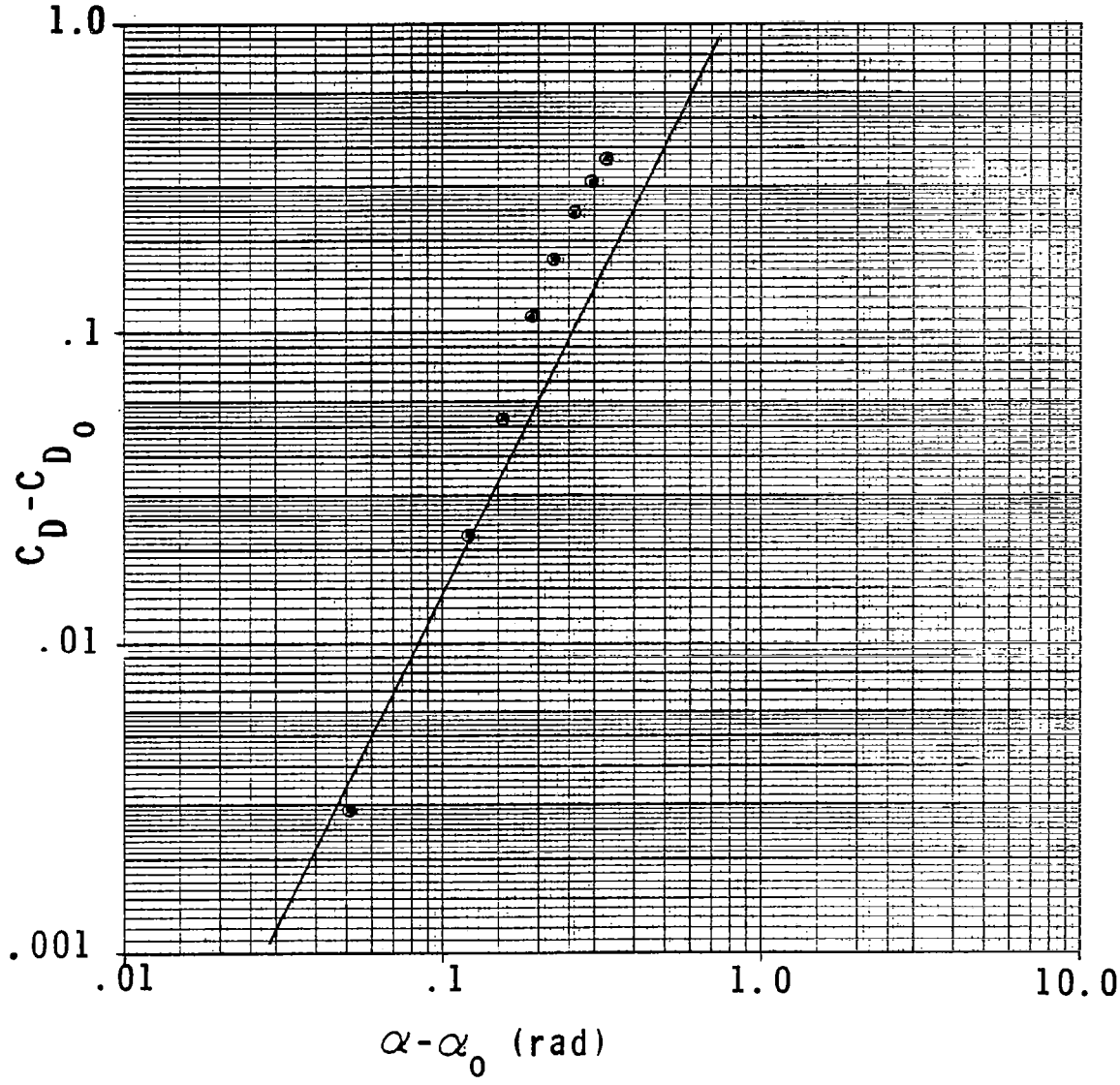

Figure 18. $(C_D - C_{D_o})$ as a function of $(\alpha - \alpha_o)$ at M = 0.18

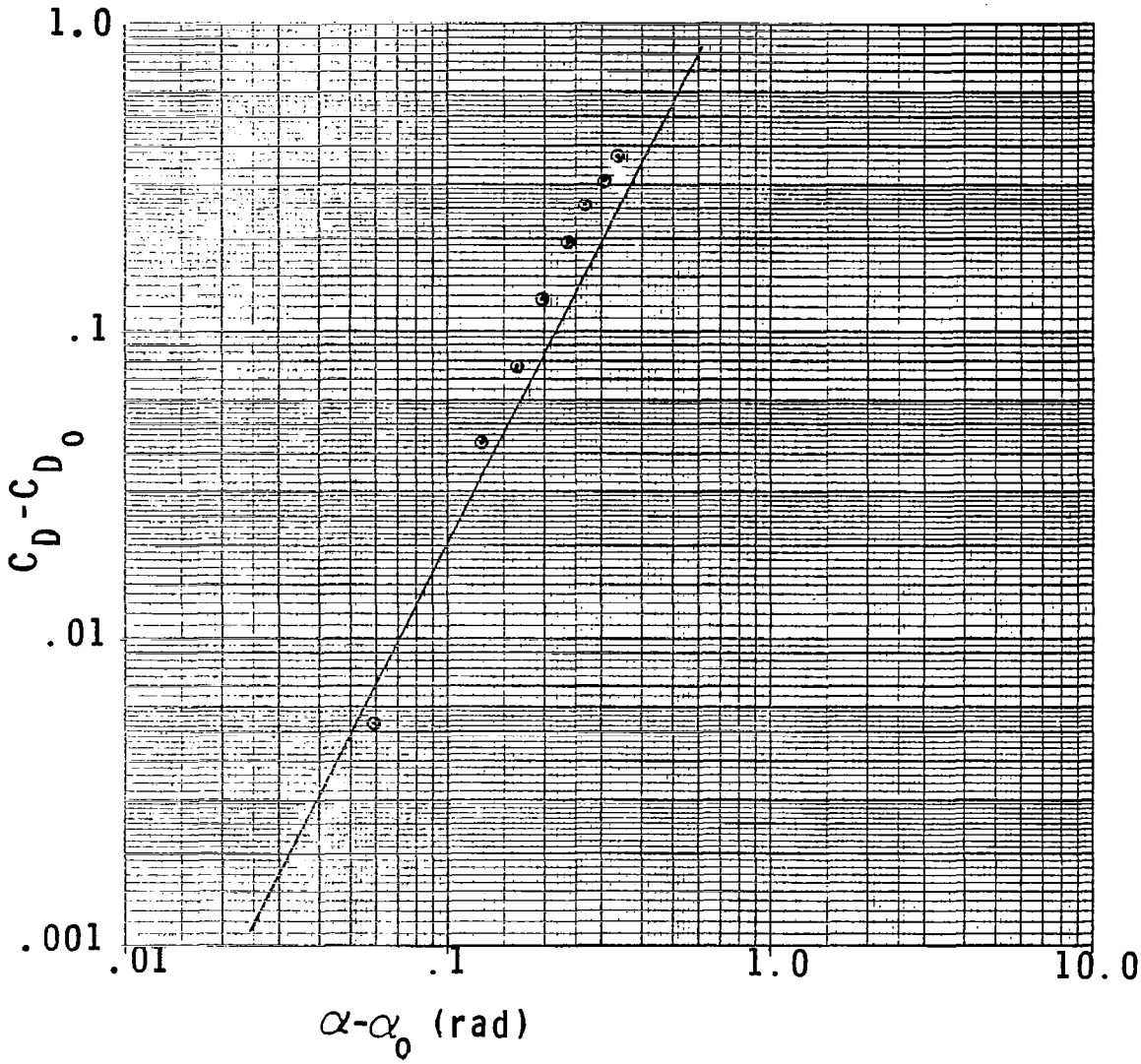

Figure 19. $(C_D - C_{D_o})$ as a function of $(\alpha - \alpha_o)$ at M = 0.6.

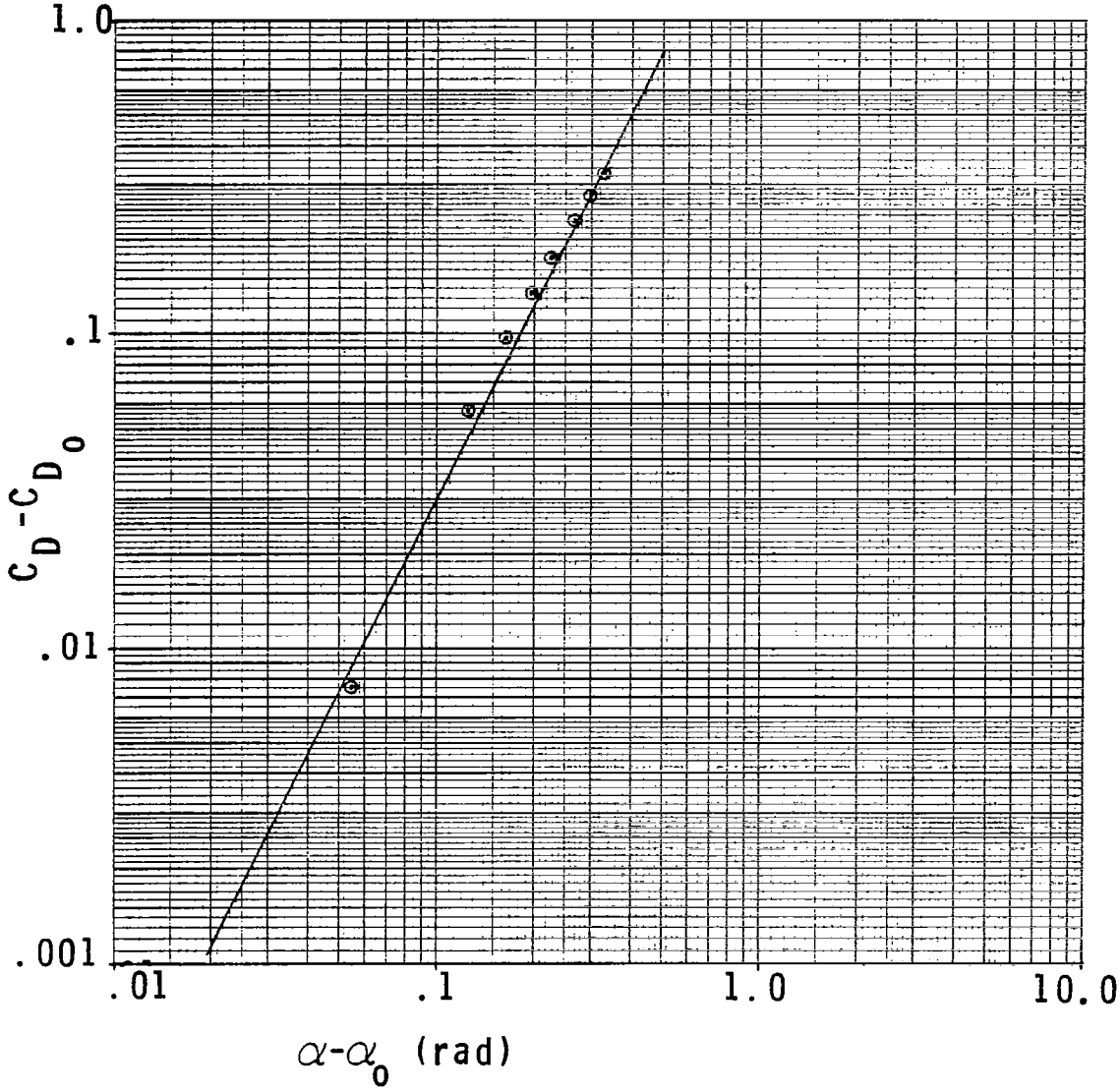

Figure 20. $(C_D - C_{D_0})$ as a function of $(\alpha - \alpha_0)$ at M = 0.85.

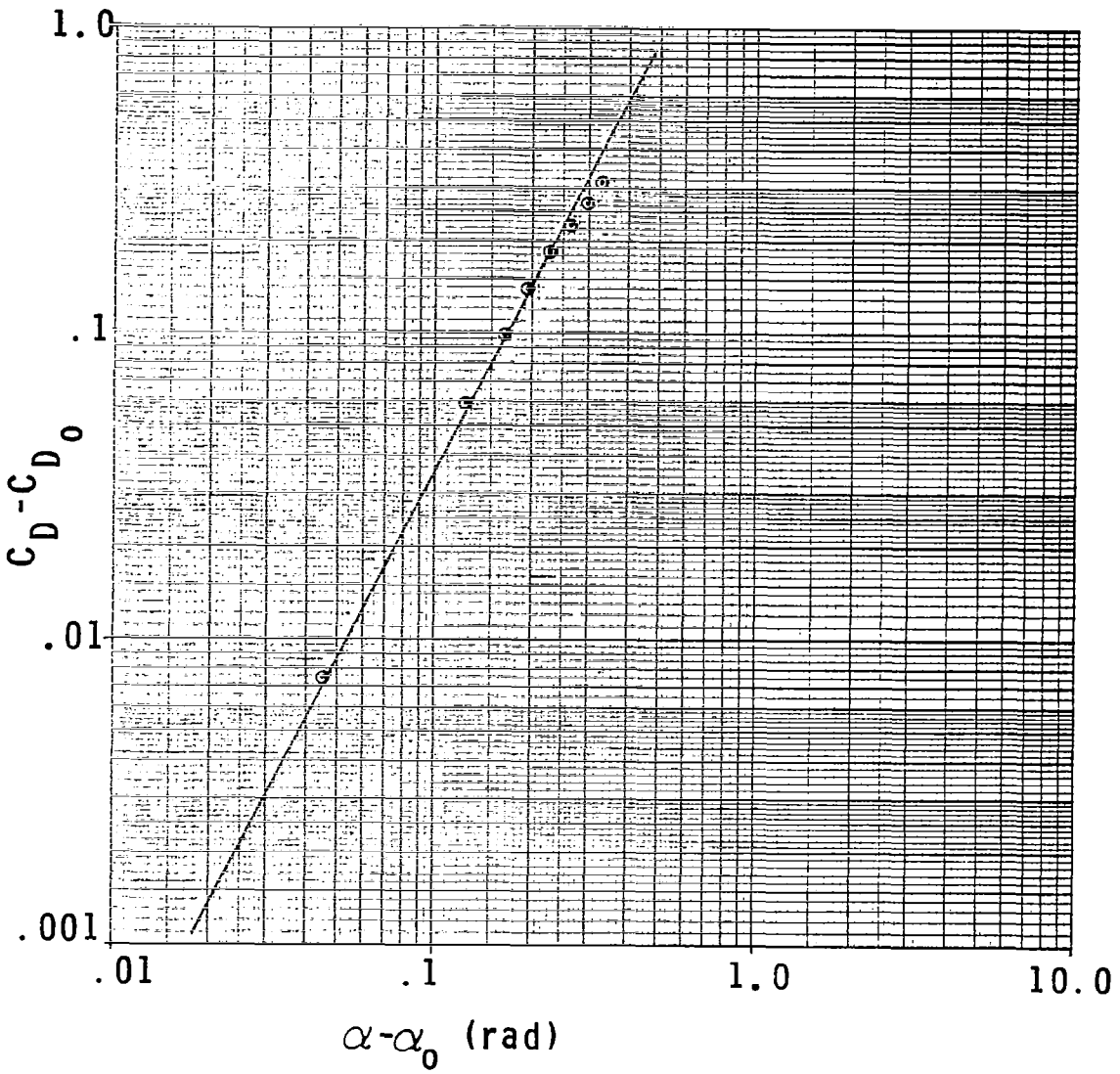

Figure 21. $(C_D - C_{D_0})$ as a function of $(\alpha - \alpha_0)$ at M = 0.9

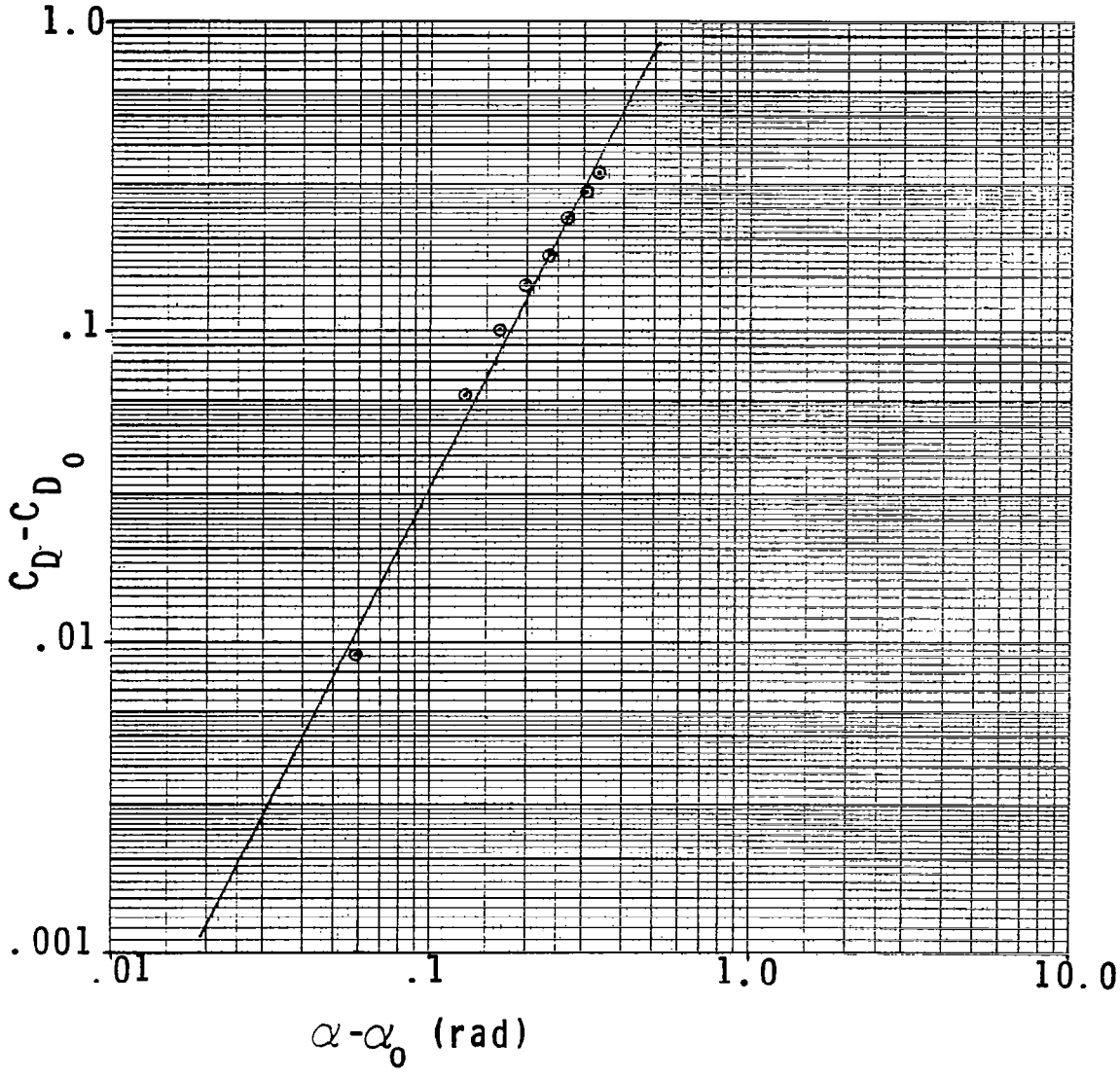

Figure 22. $(C_D - C_{D_0})$ as a function of $(\alpha - \alpha_0)$ at M = 0.98.

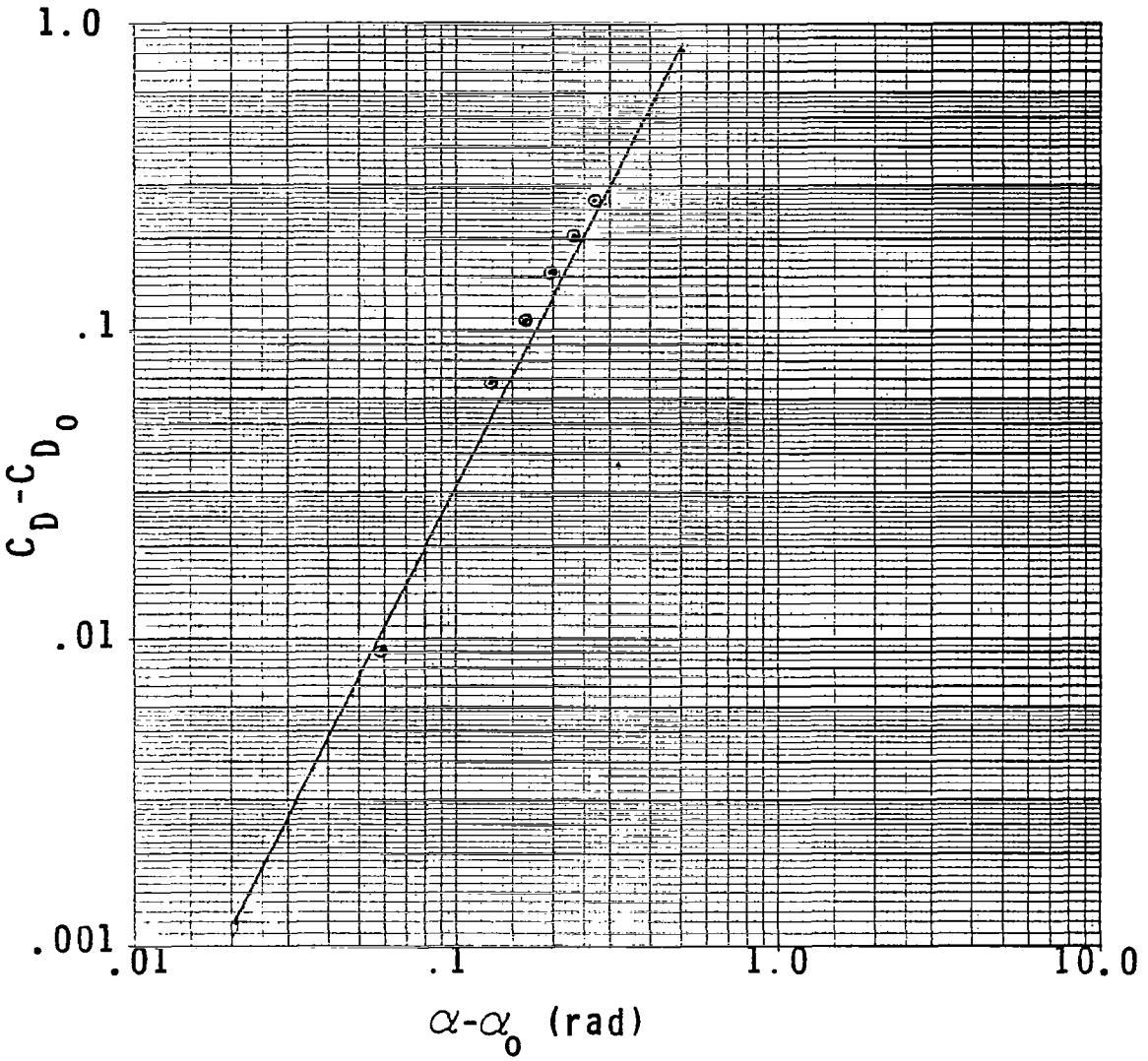

Figure 23. $(C_D - C_{D_o})$ as a function of $(\alpha - \alpha_o)$ at M = 1.1 .

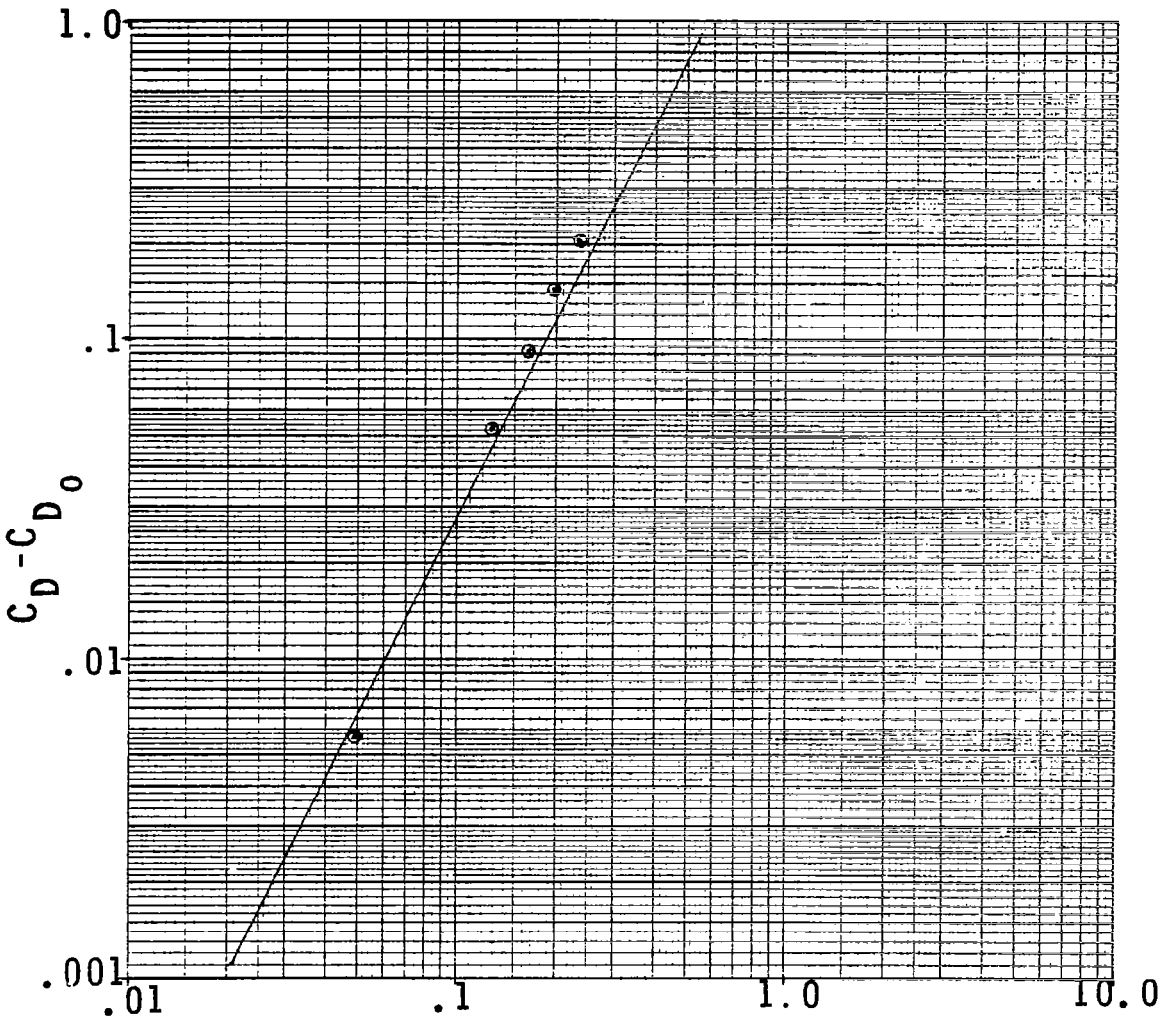

Figure 24. $(C_D - C_{D_0})$ as a function of $(\alpha - \alpha_0)$ at M = 1.2 .

Section 5

NUMERICAL RESULTS

This section documents the numerical tests conducted to verify the analytical results described in Section 2, and to test the control design described in Section 3. The aircraft simulated in this study was the F-8C, modelled as described in Section 4. The computer used in generating numerical data was the IBM 370/168. This machine has a 32 bit word size, a basic machine cycle time of 8 ns, and performs 3×10^6 floating point operations per second. Main storage access time averages 480 ns. Computation of the full zero-order solution required 0.07 seconds per update and 50198 bytes of core space. Control computation with proportional vertical lift substituted for the third and fourth boundary layer solutions required 0.03 seconds per update and 43724 bytes of core space. The difference in time and space requirements is primarily due to the numerical search (2.43) in the third boundary layer.

Five test cases were utilized for demonstration and evaluation of the control logic corresponding to a full zero-order solution. The initial conditions, intercept time and final range are summarized in Table 4.

Cases 1 through 3 share the same sort of initial geometry, though with varying initial ranges to the target. In each case, the target flies at a fixed altitude, heading and velocity. These cases were chosen to display the effect of the range matching calculation, and hence involve very little maneuvering. In all three cases, the initial heading error is small and the aircraft is at the first boundary layer optimal altitude for its initial energy. Figure 25 illustrates the resulting ground tracks. All three cases display a slight degree of turning throughout the climb and descent portions of their trajectories. This is due to the fact that the outer solution optimal heading calculation (2.24) is based on the assumption

TABLE 4

SUMMARY OF INITIAL AND FINAL CONDITIONS FOR TEST CASES

Case	x(m)	y(m)	h(m)	β(rad)	V(m/s)
1	0.	0.	3048.	0.	295.92
2	0.	0.	3048.	0.	295.92
3	0.	0.	3048.	0.	295.92
4	0.	0.	3048.	0.	295.92
5	0.	0.	9144.	0.	212.31

Case	x_T(m)	Y_T(m)	h_T(m)	β_T(rad)	V_T(m/s)
1	140208.	-80772.	3048.	1.0472	232.56
2	93023.	-53209.	3048.	1.0472	232.56
3	46698.	-27000.	3048.	1.0472	232.56
4	0.	1335.7	3048.	3.1416	274.32
5	0.	1335.7	6096.	3.1416	274.32

Case	t_f(s)	$r(t_f)$(m)
1	618.05	34.901
2	434.72	34.008
3	239.98	34.287
4	120.09	17.247
5	150.69	126.25

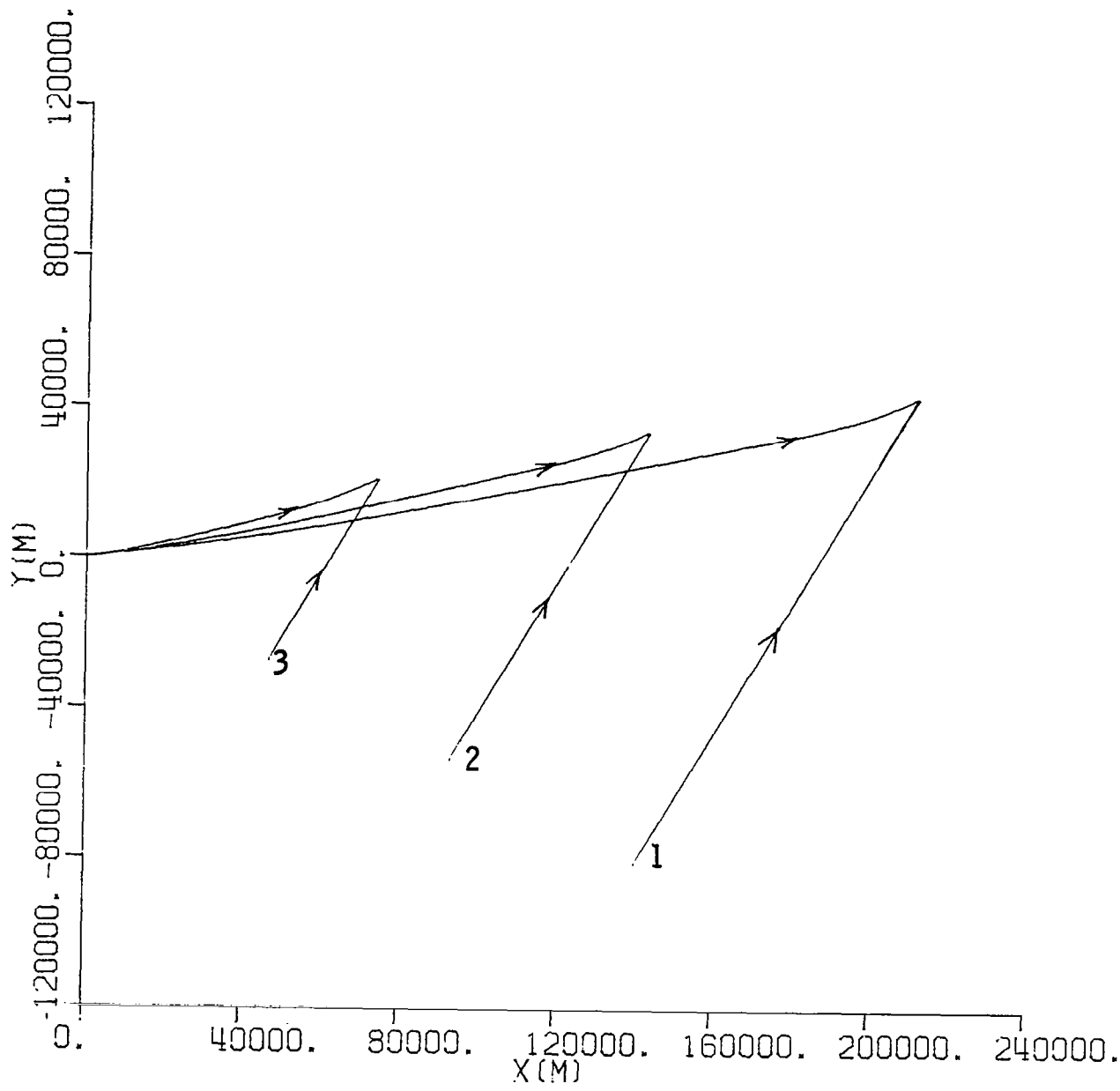

Figure 25. Ground tracks for cases 1-3.

that the aircraft flies at its cruise velocity throughout its trajectory, ignoring the fact that lower velocities are encountered during climb and descent. During climb, this variation in heading is insignificant; however, it is more noticeable during descent. This is due to the more rapidly changing line-of-sight angle (λ in Fig. 1) encountered as the target moves across the aircraft's path at relatively close range.

Figure 26 displays histories of actual and reference altitudes (h_1) for Cases 1 through 3. Case 1 is a full long range intercept; the aircraft climbs to (E_o^*, h_o^*) before descending to the target. Cases 2 and 3 are short range intercepts in that the trajectories never achieve the optimal cruise energy; instead, they reach lower pseudo cruise energies prior to descent initiation. Note that both short range intercepts contain apparent cruise legs. This is because the choice of pseudo cruise energy levels was restricted to a set of discrete values. If a continuum of pseudo cruise energies was allowed, the short range trajectories would consist of a climb to cruise immediately followed by a descent to the target. It can also be seen that the aircraft altitude tends to lag behind the reference altitude during climb in all three cases. This is because the control solution is based on a zero order singular perturbation analysis, which results in a type zero control law. Hence, a nearly constant error results when following the ramp-like altitude reference during climb. Inclusion of first-order correction terms in the control solution would be necessary to eliminate these errors. It is interesting to note the discontinuity at $t = 29s$ in the reference altitude for Case 3. This occurred because the aircraft was lagging the reference altitude during climb, thus travelling faster than it should have at all energy levels, and closing range with the target at a faster pace than appropriate for the climb path. Finally, the range to the target became sufficiently shortened that it became

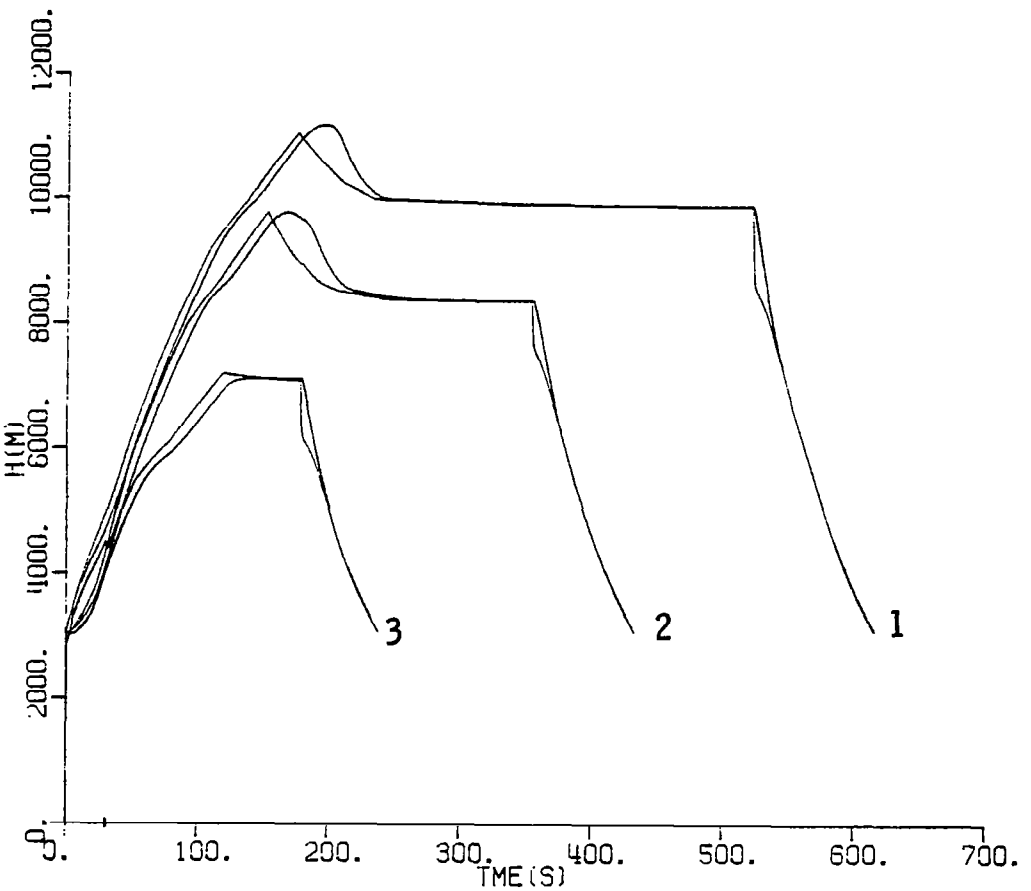

Figure 26. Command and actual altitude profiles for cases 1-3.

necessary to range match to a lower pseudo cruise energy level. A discontinuity in reference altitude can also be observed at the beginning of descent for all three cases. This can be attributed to the energy state model of the aircraft and the fact that, while the aircraft's optimal cruise point is defined by (2.20), the descent path is defined, via (2.31), as the altitude and energy corresponding to the q_{max} boundary. In the F-8 aircraft, these points do not coincide at the pseudo cruise energies encountered in Cases 1 through 3.

Figure 27 displays aircraft altitude as a function of velocity for Case 2. It can be seen that the energy gain during climb occurred at almost constant velocity. Figure 28 displays actual and reference flight path angle (γ_3) histories for Case 2. Figure 29 shows lift and bank angle profiles for the same case. The beginning of descent is clearly marked in Figure 28 by a sudden decrease in the reference flight path angle. The resulting control profiles call for near maximum lift and inverted flight to rotate the flight path angle. This amounts to a zoom dive to the descent path. Figure 30 displays the thrust history for Case 2. During descent, ripples can be seen in both lift and thrust. These arise from the proportional vertical lift calculation used during the descent leg. The reference flight path angle, γ_D from (3.13), is dependent on the term $\dot{E}(dh_1/dE)/V$. The derivative is calculated by a first order difference expression directly from the tabular descent data listed in Table 2. The ripples in γ_D, and hence in lift (3.15), occur when the aircraft altitude passes across intervals between the discrete points comprising the descent data. These ripples affect the thrust through δT_1 in (3.21) and (3.22). The average variation is a consequence of the range matching taking place during descent. The accuracy of this

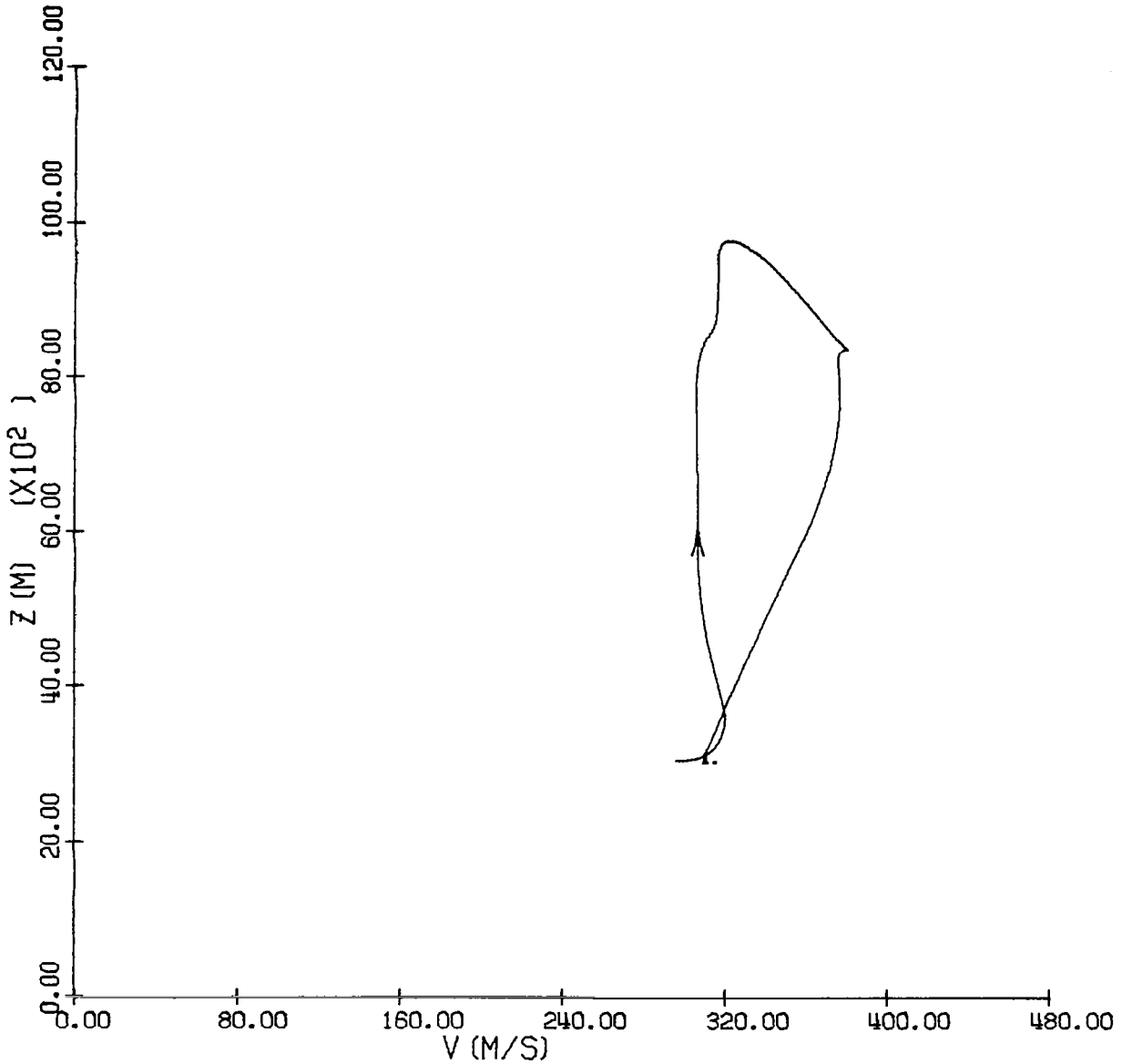

Figure 27. Altitude versus velocity for case 2.

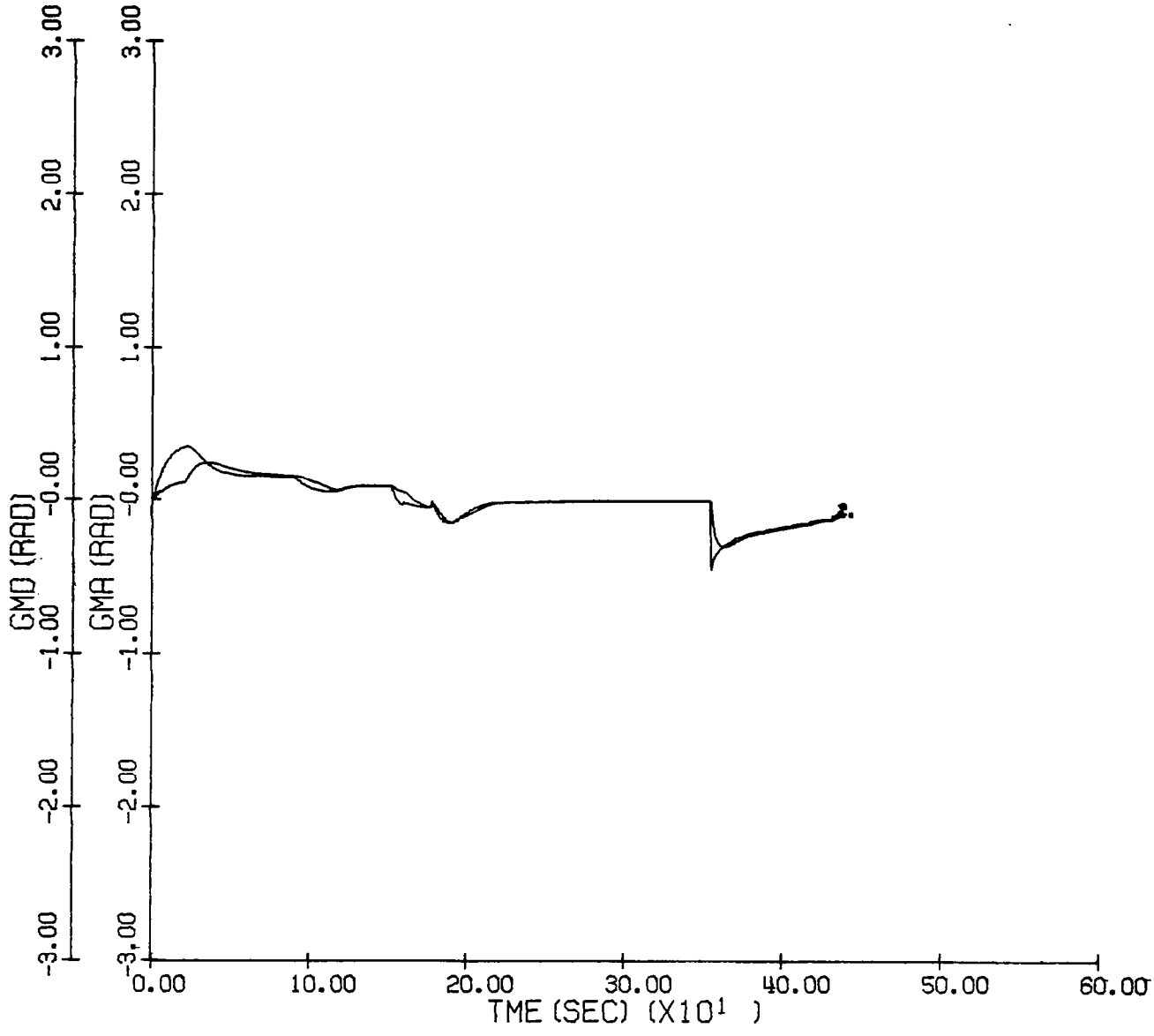

Figure 28. Command and actual flight path angle profile for case 2.

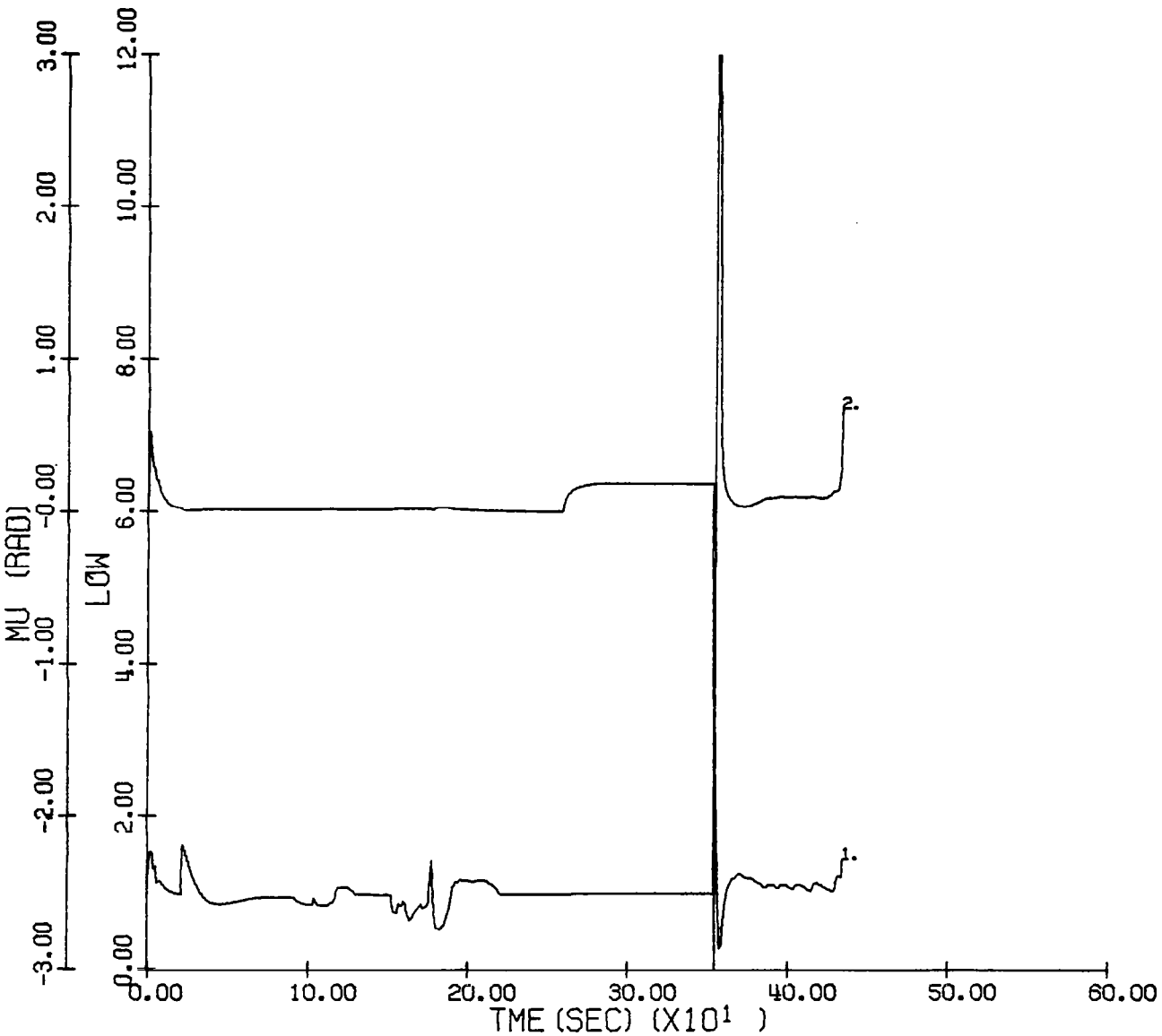

Figure 29. Lift and bank angle profile for case 2.

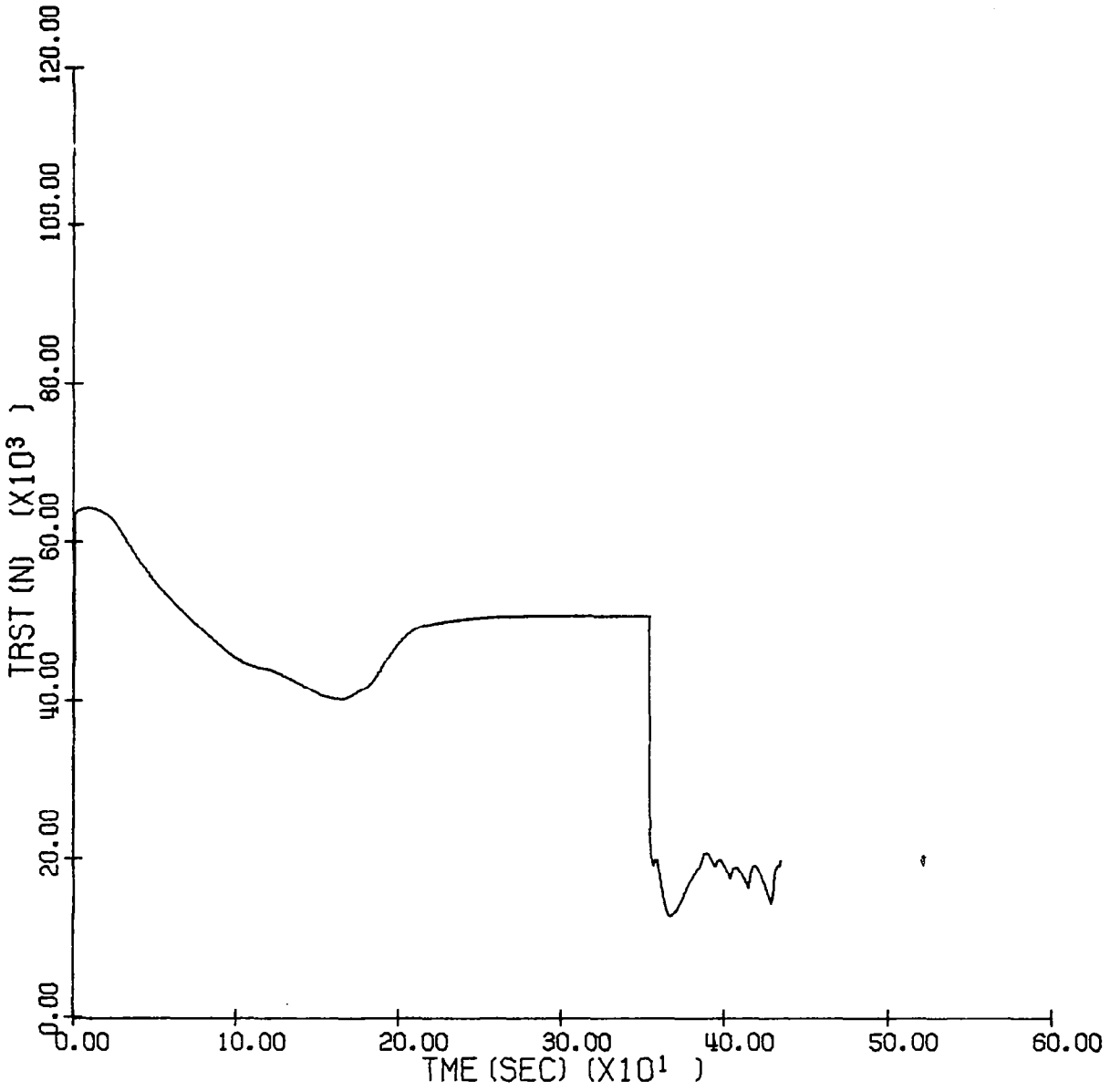

Figure 30. Thrust profile for case 2.

approach is demonstrated by the small values for $r(t_f)$ in Table 4.

Figure 31 displays the ground track for Case 4. In this case, the aircraft is initially at the first boundary layer optimal altitude for its initial energy, offset laterally from the target by a distance corresponding to the diameter of a turn for the aircraft at the highest sustainable turn rate for the initial conditions. The target moves at a constant altitude and velocity at a heading opposite from the controlled aircraft's initial heading. This case illustrates a combined initial turn and climb behavior, followed by a descent under near tail chase conditions. Figure 32 gives the actual and reference altitude histories for this case. Note that during the initial hard turn, the aircraft performs a "high speed yo-yo" maneuver, moving up in altitude (above the climb path) to trade speed for enhanced turning performance. During this phase, the reference altitude from the second boundary layer (h_2) deviates markedly from the first boundary layer optimal altitude (h_1), due to the initial heading error. Within thirty seconds, however, the heading error has been brought down to a small value, resulting in the reference altitude asymptotically approaching the altitude called for from the first boundary layer solution. Note that the sudden change in reference altitude around $t = 10$ s is consistent with the behavior of the second boundary layer solution as displayed in Figure 4, where a sudden jump to the corner velocity altitude takes place for large heading errors at low to midrange energy levels. Figure 33 shows the altitude versus velocity profile for Case 4. Figures 34 and 35 display the reference and actual flight path angle profiles, and the lift and bank angle profiles for this case.

Figure 36 is the ground track for Case 5. This case involved both a large initial heading error and a 6096 m offset from the climb path. This case was selected to demonstrate high altitude turning behavior, and

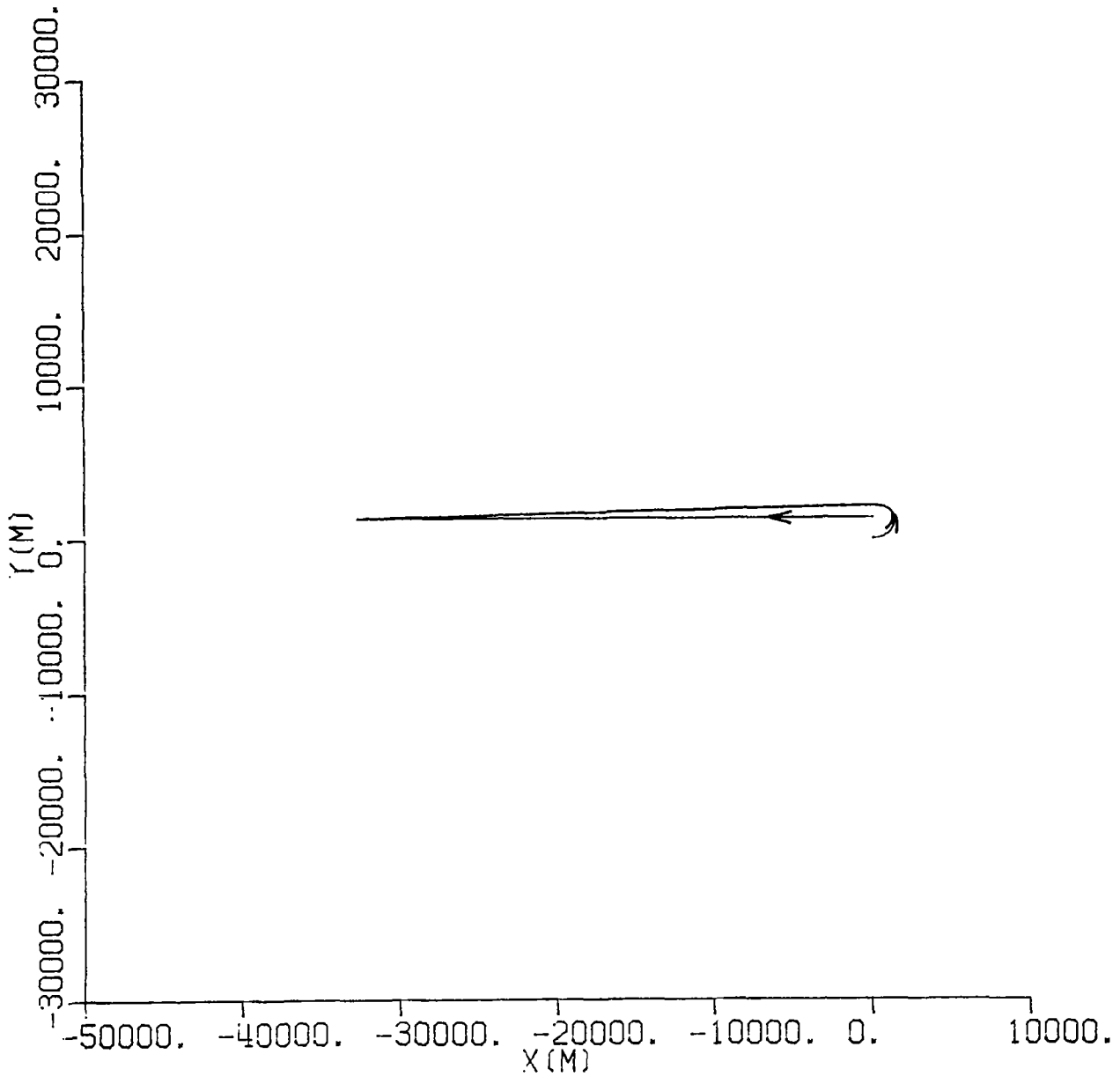

Figure 31. Ground track for case 4.

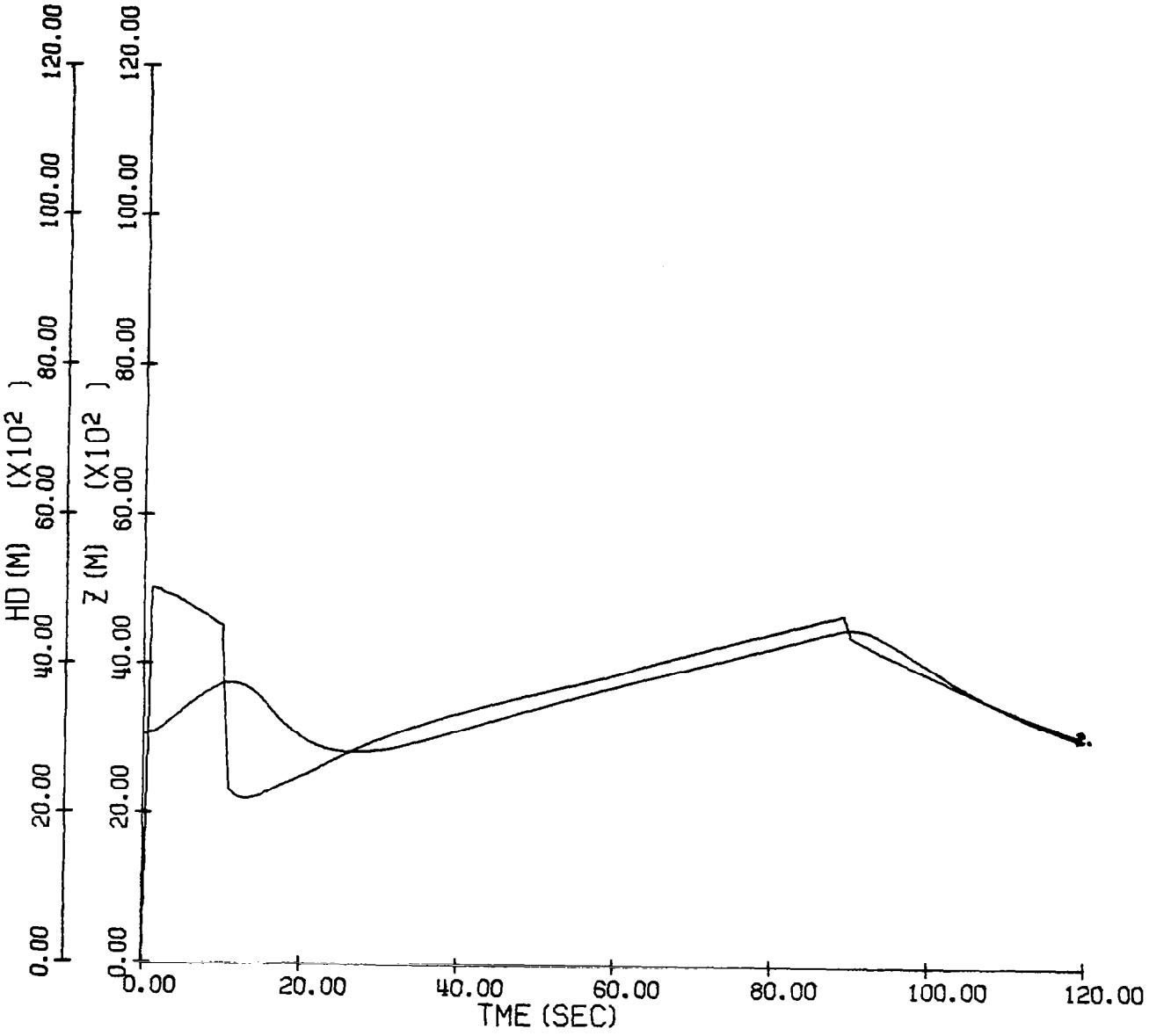

Figure 32. Command and actual altitude profile for case 4.

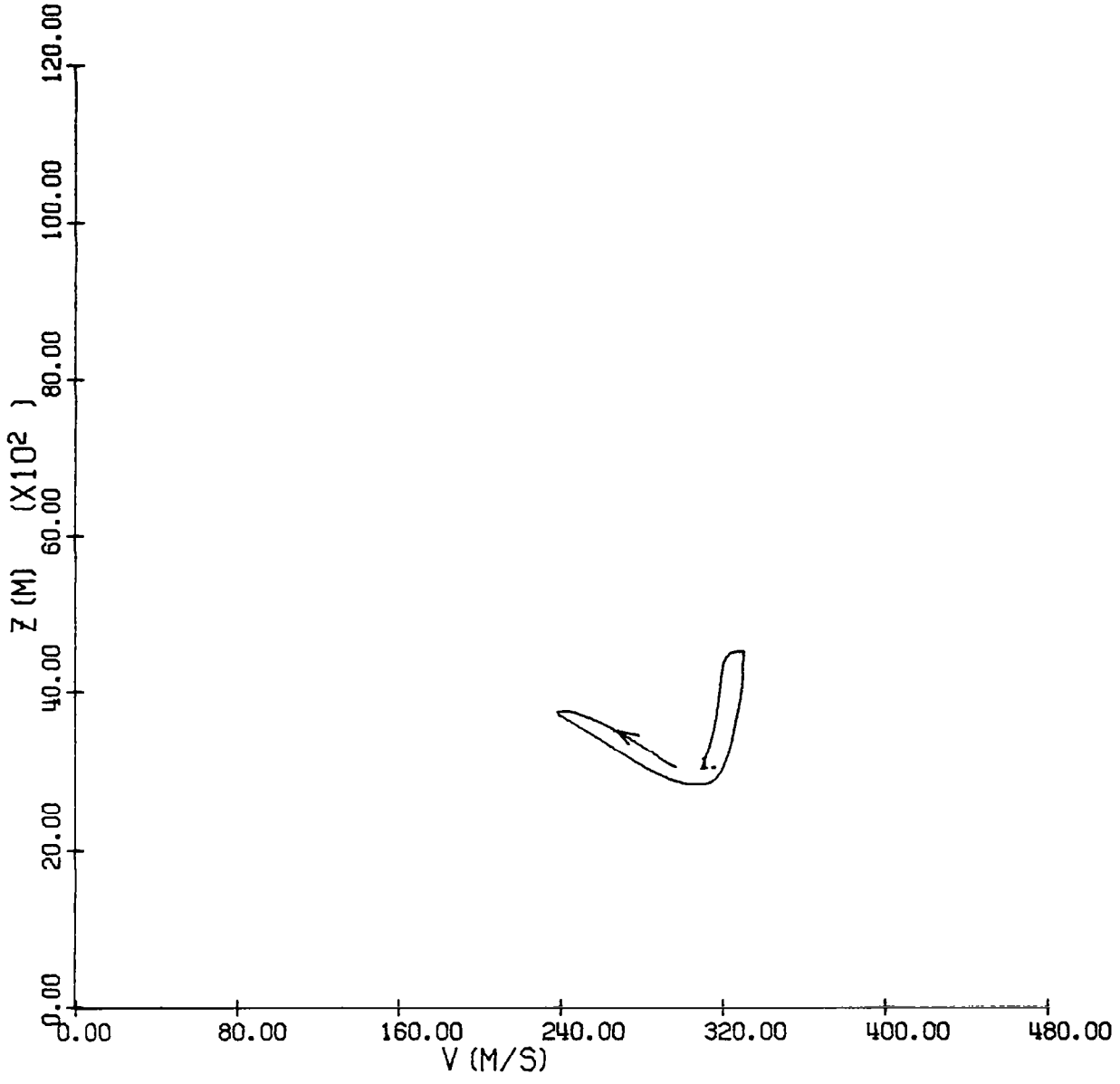

Figure 33. Altitude versus velocity for case 4.

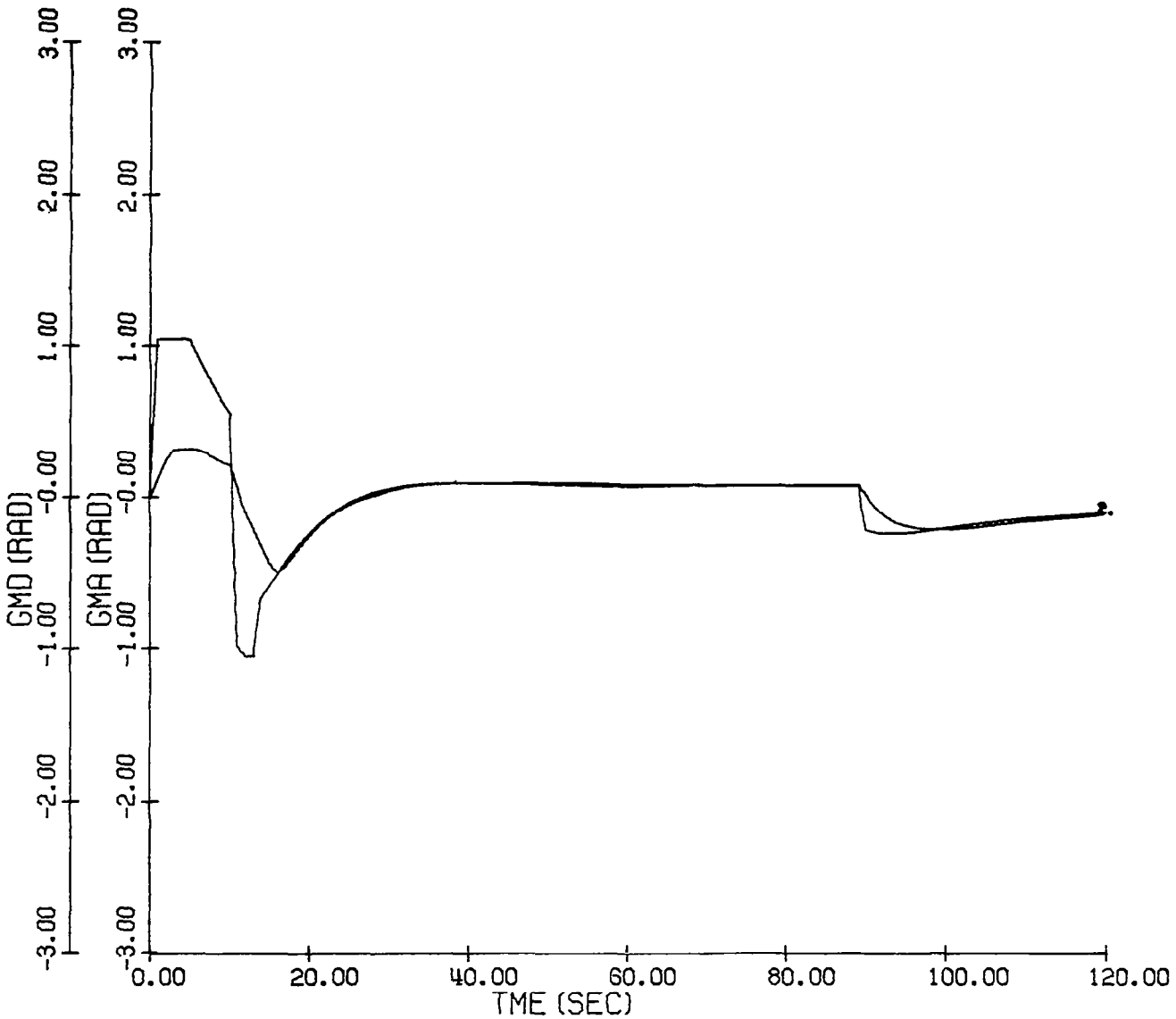

Figure 34. Command and actual flight path angle profile for case 4.

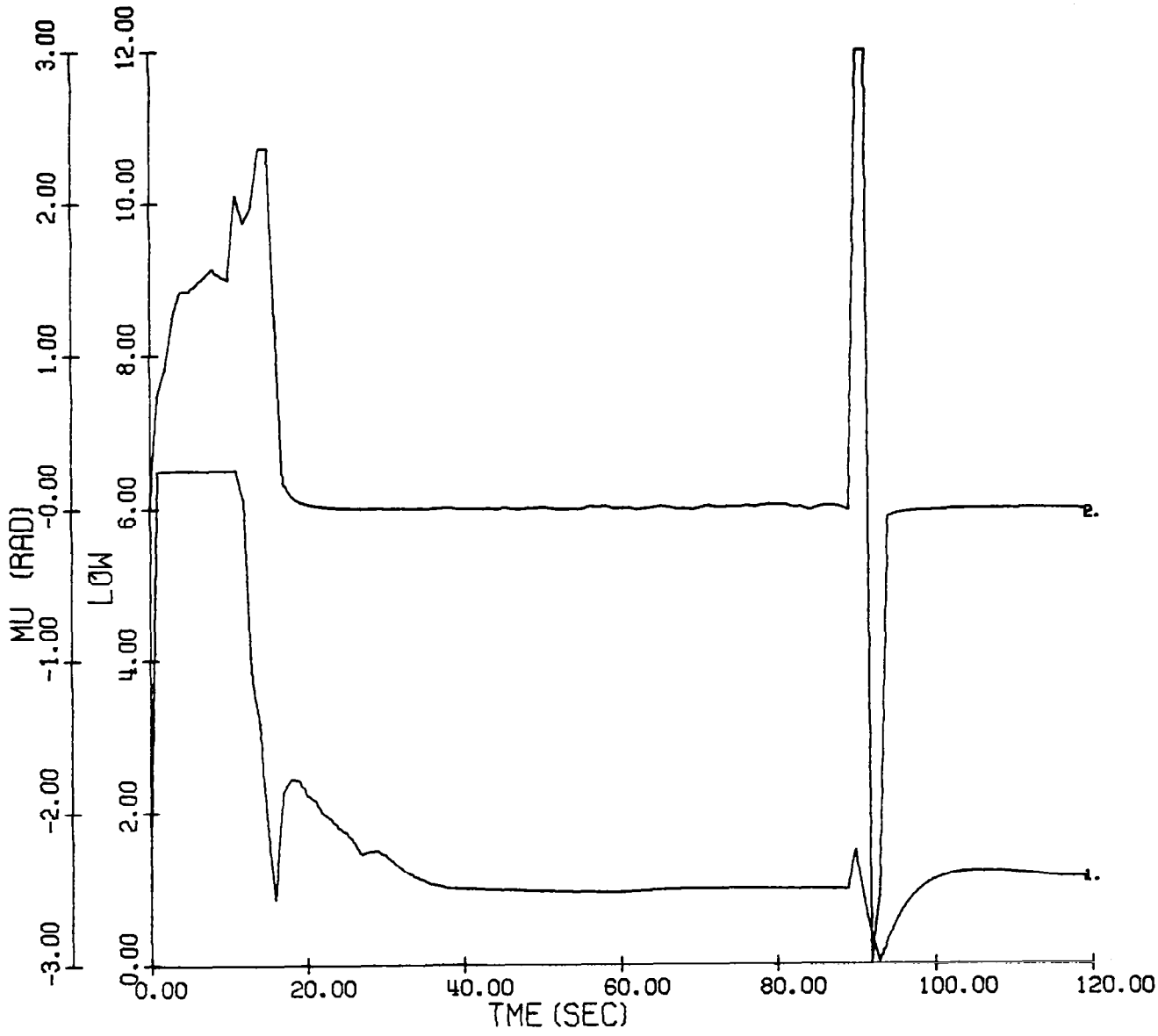

Figure 35. Lift and bank angle profile for case 4.

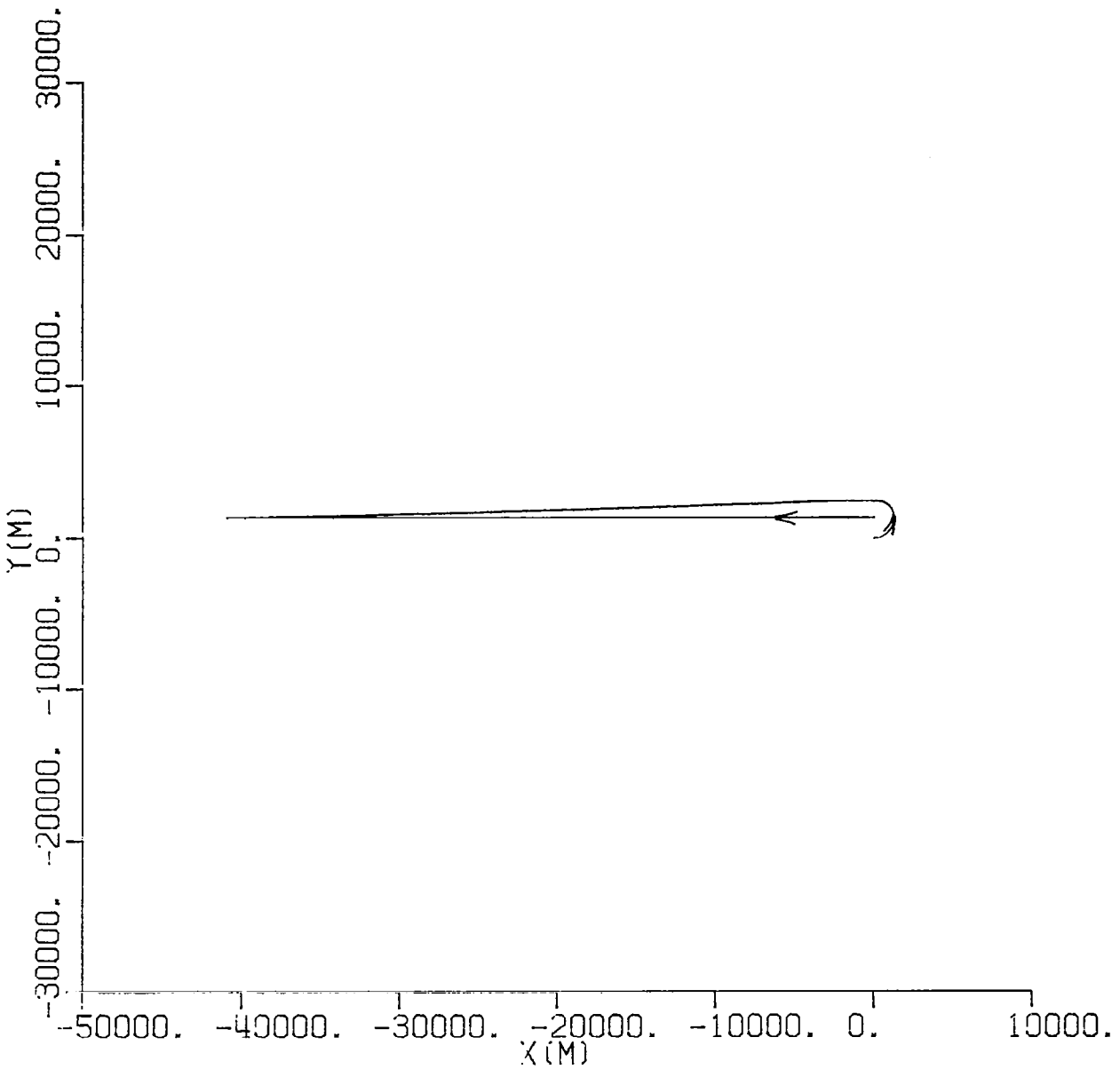

Figure 36. Ground track for case 5.

the balance in allocation of resources for reduction of heading and altitude errors. The horizontal plane geometry for this case is similar to that of Case 4, with the target moving in the same manner, though at a higher altitude. Again, the aircraft is initially separated from the target by a distance corresponding to the diameter of a turn made at the highest sustainable turn rate for the aircraft's initial conditions. Figure 37 gives the actual and reference altitude histories for this case. It can be seen that initially more emphasis is given to reducing heading error. In Figure 38, altitude is shown as a function of velocity. Figures 39 and 40 are the reference and actual flight path angle histories, and the lift and bank angle profiles.

Comparing the lift histories for cases 4 and 5, one notes that in Case 4 the low altitude turning behavior is characterized by a liberal use of maximum lift (Fig. 35), which indicates that zeroing of heading error, under the circumstances, is of greater importance than gaining energy. On the other hand, for Case 5, lower values of lift are called for (Fig. 40). This is in agreement with Figure 3, which shows that the control solution for the second boundary layer tends to inhibit the use of lift at higher energies.

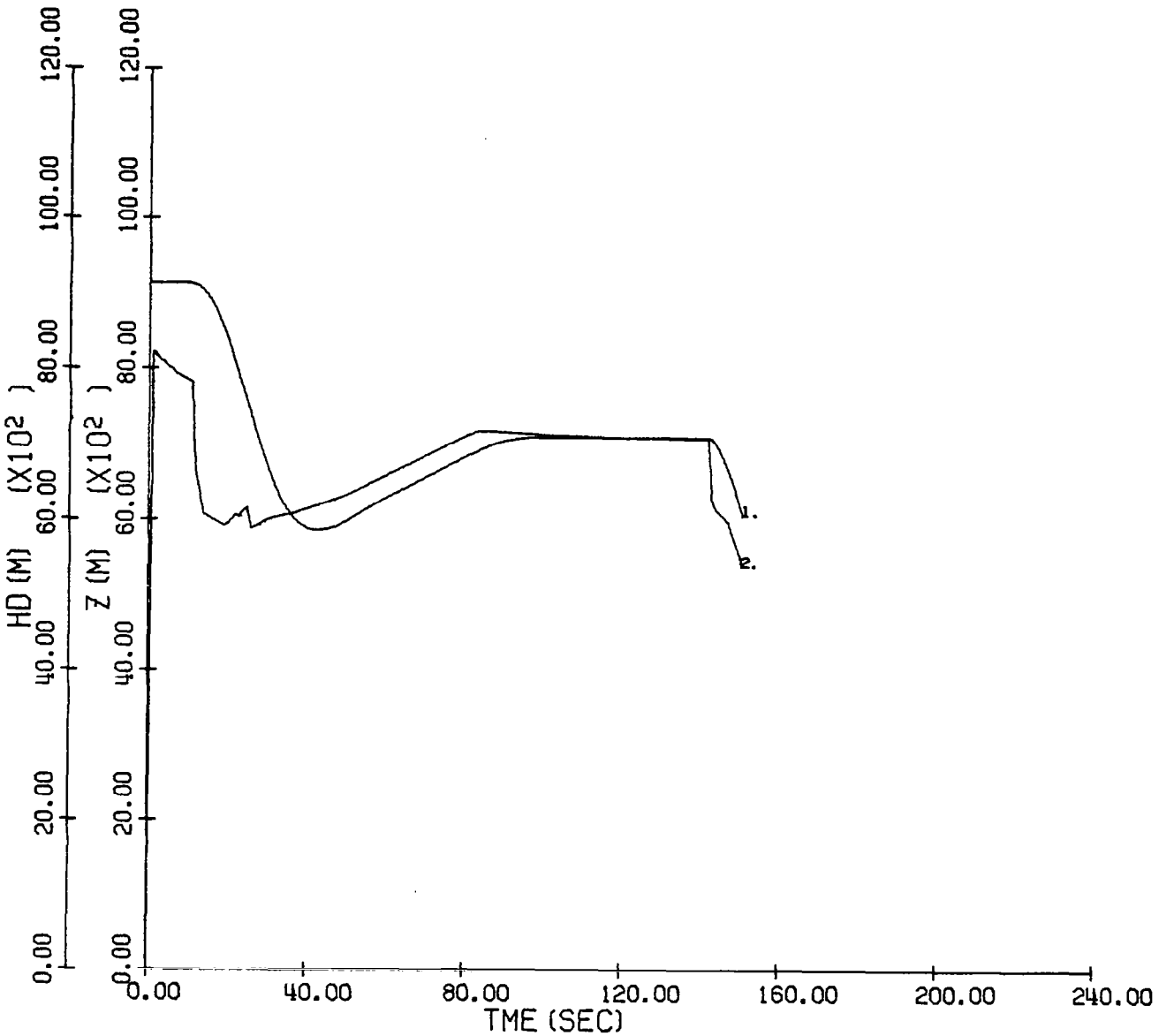

Figure 37. Command and actual altitude profile for case 5.

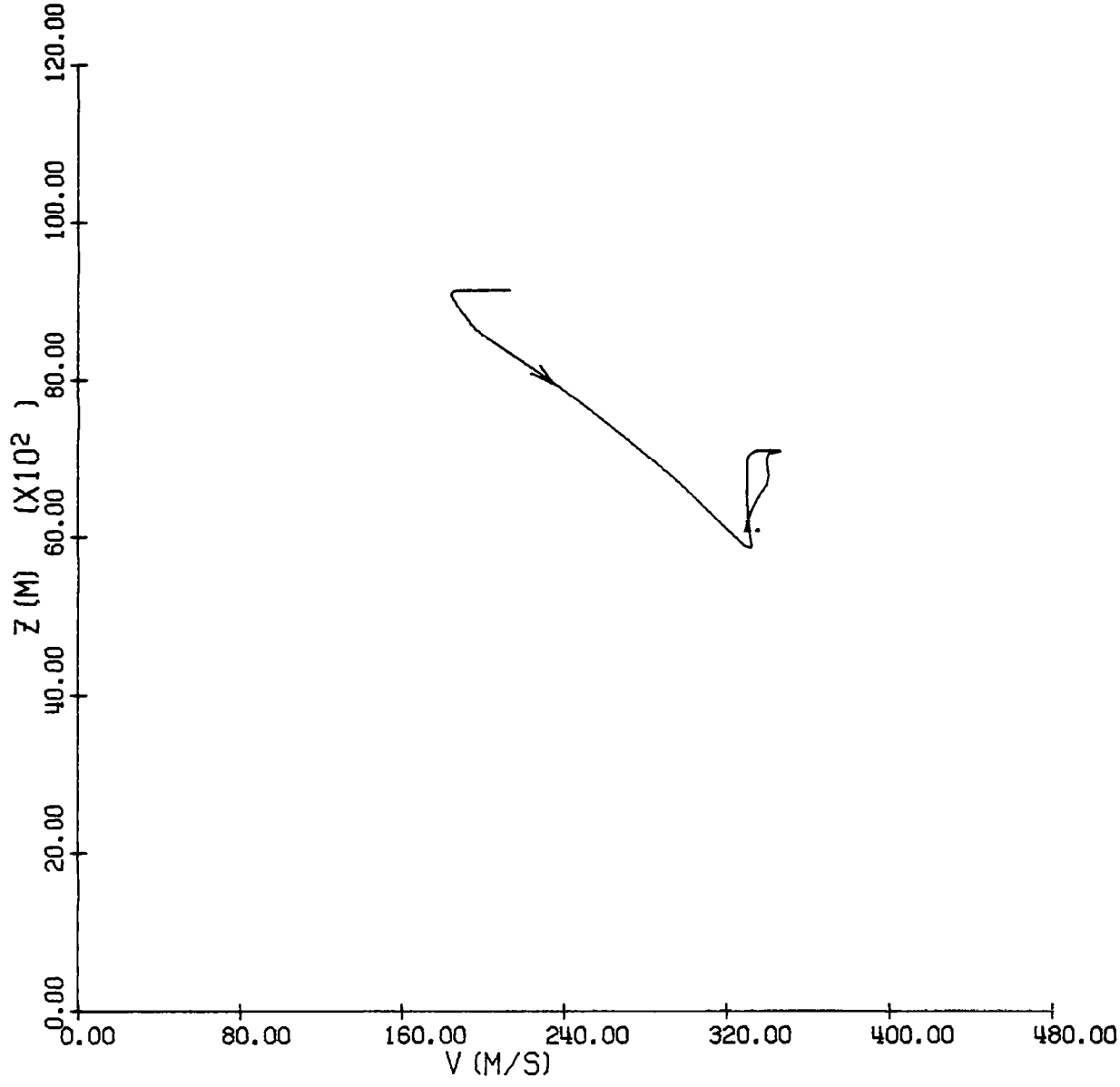

Figure 38. Altitude versus velocity for case 5.

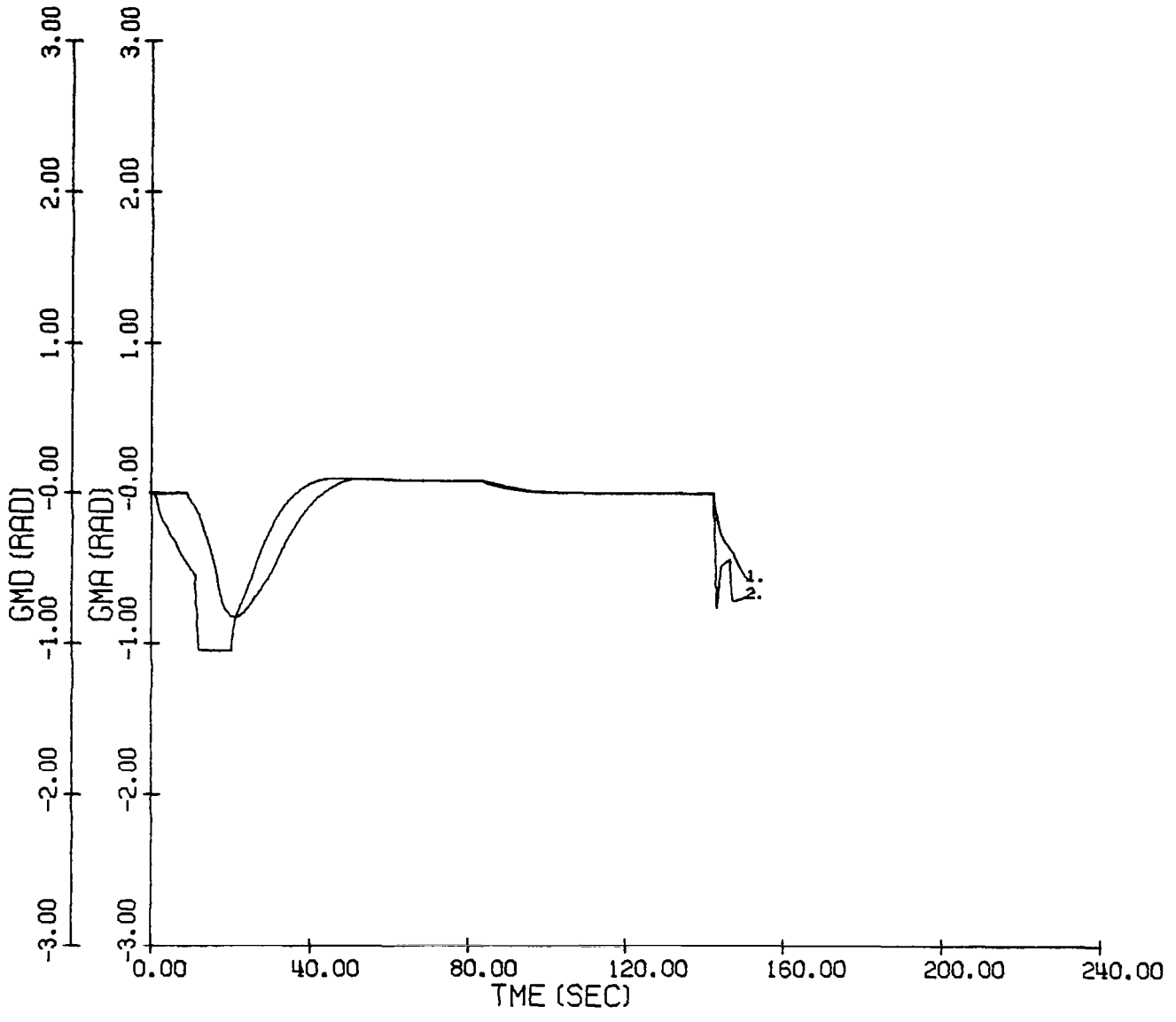

Figure 39. Command and actual flight path angle profile for case 5.

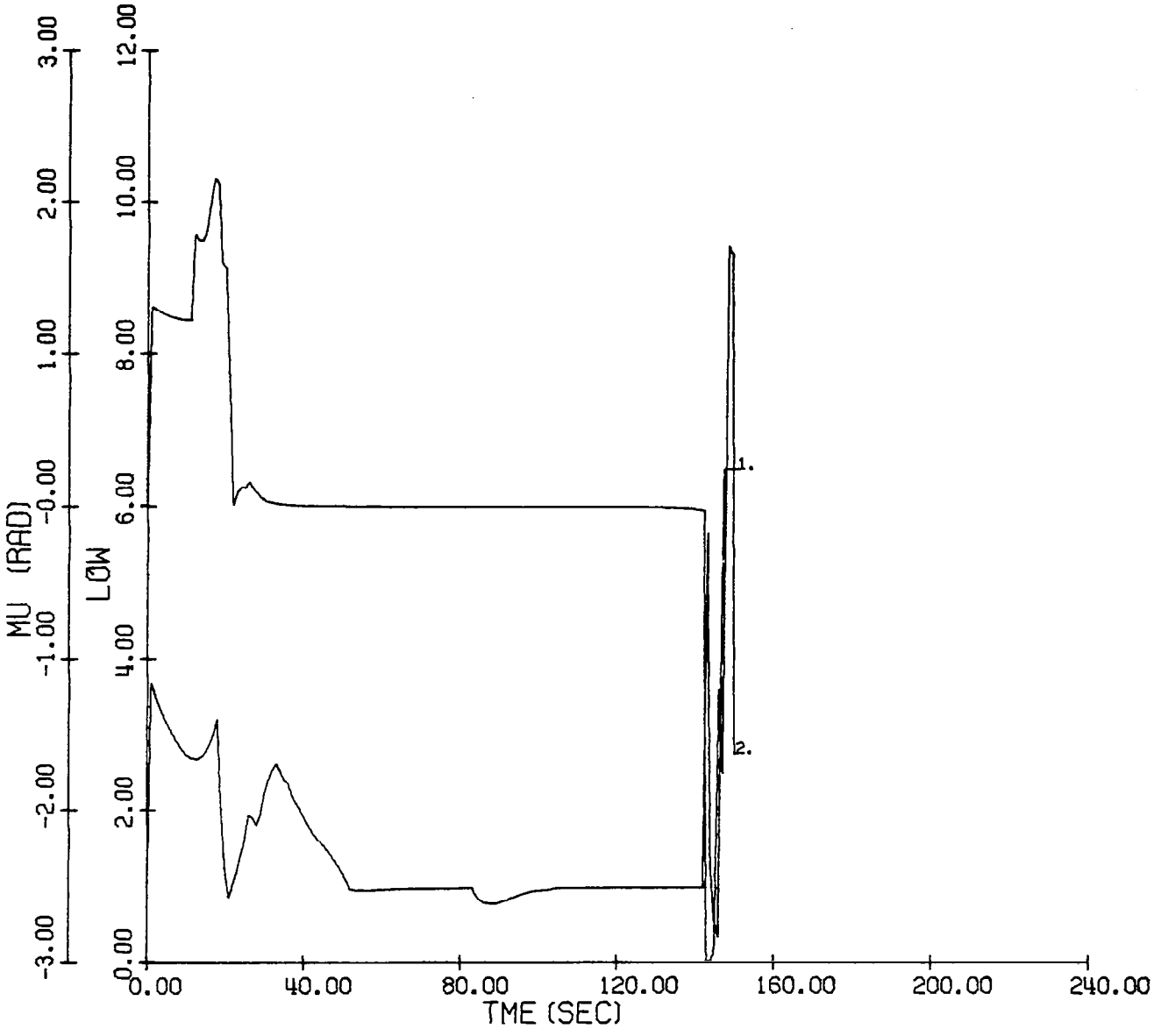

Figure 40. Lift and bank angle profile for case 5.

SECTION 6

CONCLUSIONS AND RECOMMENDATIONS

It has been demonstrated that singular perturbation methods are an effective tool for developing computer algorithms for on-line optimal aircraft controls. The computation time and storage requirements appear to be within the capabilities of present day flight computers. This evaluation is based on a minimum time intercept problem. Extensions to other performance indices and other forms of terminal constraints should be possible.

An essential aspect in obtaining implementable solutions is the ability to order the individual state variables on separate time scales. This requires considerable insight to the dynamics of optimal flight so that a suitable ordering can be made at the outset. The ordering selected here should be applicable to a variety of problem formulations. In general, not all state variables will have separable dynamics. However, this study has illustrated two techniques for overcoming this difficulty. For short range intercept problems, the position and energy dynamics are coupled, and the problem was corrected by constraining the cruise energy level. In general, altitude and flight path angle dynamics are highly coupled for all intercept conditions. In this case, penalizing flight path angle variations is effective in accounting for this coupling.

A second aspect that may be a stumbling block in singular perturbation analysis (at least from the perspective of real time control) is the need to define the terminal boundary layer initiation times. The number of these layers is dependent on the number of boundary layer state variables that are constrained at the terminal time. This definition requires a boundary layer integration, which in the case of minimum time intercept can be performed off-line. In other formulations, boundary layer integration can have a large impact on the requirements for real time implementation. When they cannot be done off-line, then an attempt should be made to expand the necessary conditions to second order and obtain an analytic expression for the integral.

Based on the results of this study, we offer the following recommendations:

1. Flight Testing - As mentioned in Section 1, the control algorithm has been tested at the NASA Langley real time simulation facility. Hence, a logical next step would be an actual flight test. Such an effort would require very little in terms of modifications to the control algorithm, and could make use of the F-8 fly-by-wire test bed at the NASA Dryden facility. It should be noted that, as a result of the piloted simulation effort at Langley, many of the issues relating to interfacing with displays have been addressed.

2. Effect of Wind - To date, the effect of wind on the performance of the control solution has neither been evaluated nor compensated for. Obviously, this topic would have to be addressed before a practical implementation of the controller could take place.

3. Higher Order Solutions - The control law is currently a zero-order approximation to the optimal control. In climb, this results in a significant lag in following the desired climb profile. This can be corrected by introducing first-order correction terms into the first boundary layer solution. Similarly, errors in the outer solution optimal heading, arising from the rapidly changing velocity and non-zero flight path angles in the descent boundary layer, would be reduced by correcting the cruise heading to first-order to account for these effects. These corrections would primarily affect the off-line computations.

4. Other Performance Indices - Performance indices other than minimum time need to be investigated. For example, a logical extension is to consider a weighted combination of time and fuel consumption. This would encompass most mission objectives. It should be noted in this context that the strict minimum time case is highly specialized in that the outer and first boundary solutions for h and V are independent of geometry and target velocity.

5. Bank Angle Computation - In situations where the lift magnitude is small, large fluctuations result from small variations in the bank angle command in the horizontal and vertical lift components. In the context of a practical implementation, this amounts to an excessive pilot effort in return for a minor trajectory correction. Hence, development of a suboptimal strategy to correct this shortcoming is called for.

APPENDIX A

OPTIMIZATION OF POSITION, ENERGY AND HEADING DYNAMICS

This appendix provides a detailed derivation of the zero-order control solutions optimizing position, energy and heading dynamics. The state equations, for the coordinate frame shown in Figure 1, are

$$\dot{x} = V \cos\gamma \cos\beta \tag{A.1}$$

$$\dot{y} = V \cos\gamma \cos\beta - V_T \cos\gamma_T \tag{A.2}$$

$$\varepsilon\dot{E} = (T-D)V/W \tag{A.3}$$

$$\varepsilon^2\dot{\beta} = L \sin\mu/mV \cos\gamma \tag{A.4}$$

$$\varepsilon^3\dot{h} = V \sin\gamma \tag{A.5}$$

$$\varepsilon^4\dot{\gamma} = (L \cos\mu - W\cos\gamma)/mV \tag{A.6}$$

The following conditions must be satisfied for optimality:

$$\dot{\lambda}_x = -\partial H/\partial x \quad , \quad \dot{\lambda}_y = -\partial H/\partial y \tag{A.7}$$

$$\varepsilon\dot{\lambda}_E = -\partial H/\partial E \tag{A.8}$$

$$\varepsilon^2\dot{\lambda}_\beta = -\partial H/\partial\beta \tag{A.9}$$

$$\varepsilon^3\dot{\lambda}_h = -\partial H/\partial h \tag{A.10}$$

$$\varepsilon^4\dot{\lambda}_\gamma = -\partial H/\partial\gamma \tag{A.11}$$

$$L, \mu, T = \arg\min_{L,\mu,T} H(\underline{x}, \underline{\lambda}, \underline{u}) \tag{A.12}$$

$$H = \underline{\lambda}^T\dot{\underline{x}} + 1 + k\sin^2\gamma + \text{constraints} \tag{A.13}$$

where the minimization in (A.12) is subject to the constraints (2.13-2.16). The Hamiltonian in (A.13) is defined for the performance index in (2.12).

A.1 Outer Solution

Taking the limit in (A.1 - A.11) as $\varepsilon\to 0$ we have the following zero-order necessary conditions for the outer solution:

$$T_o = D_o, \ \mu_o = 0, \ \gamma_o = 0, \ L_o = W \tag{A.14}$$

$$\partial H_o/\partial E = \partial H_o/\partial h = \partial H_o/\partial\beta = 0 \tag{A.15}$$

$$H_o = \lambda_{x_o} V\cos\beta + \lambda_{y_o}(V\sin\beta - V_T \cos\gamma_T) + 1 + \text{constraints} = 0 \tag{A.16}$$

where D_o is drag for $L_o = W$ and is defined in (2.22). Note from (A.15) that E, h and β take the role of control variables as we let $\varepsilon \to 0$ and (A.8 - A.11). This implies that E, h and β minimize H_o. At the same time, the original controls now become constraints in (A.14). The optimal heading β_o is derived as follows. From (A.15) we have

$$\partial H_o/\partial\beta = -\lambda_{x_o} V\sin\beta + \lambda_{y_o} V\cos\beta = 0 \tag{A.17}$$

or that

$$\tan\beta_o = \lambda_{y_o}/\lambda_{x_o} \tag{A.18}$$

implying, from (A.7), that the optimal heading is constant. Referring to Figure 1, the geometrical requirement for intercept in the horizontal plane is

$$V\sin(\beta-\lambda) = V_T \cos\gamma_T \cos\lambda \tag{A.19}$$

where λ is the line-of-sight angle.

The optimal cruise point (h_o, E_o) is derived in the following manner. We use (A.18) to eliminate λ_y from (A.16) resulting in

$$H_o = \lambda_{x_o} V/\cos\beta - \lambda_{x_o} V_T\cos\gamma_T\tan\beta + 1 + \text{constraints} = 0 \tag{A.20}$$

This gives

$$\lambda_{x_o}/\cos\beta = -1/(V-V_T\cos\gamma_T\sin\beta) < 0 \tag{A.21}$$

From the intercept condition (A.19), it can be seen that the denominator of (A.21) must be positive. Applying this condition to (A.20) and minimizing H_o gives:

$$h_o,\ E_o = \arg\max_{h,E}(V-V_T\cos\gamma_T\sin\beta)\ \Big|_{T_\delta=D_o} \tag{A.22}$$

Despite the seeming dependency of the solution of (A.22) on V_T, γ_T and β, it can be shown that h_o and E_o are independent of target parameters and intercept geometry. Denoting the quantity being maximized in (A.22) as η, we will show that $\partial\eta/\partial V > 0$ for all values of V. It follows that (A.22) reduces to finding h and E that maximizes V subject to the constraints (A.14) and also (2.13-2.16). Examining the variation of (A.22) and the intercept condition (A.19) we have

$$\delta\eta = \delta V - V_T \cos\gamma_T \cos\beta_o \, \delta\beta \tag{A.23}$$

and

$$\delta V \sin(\beta_o - \lambda) + V_o \cos(\beta_o - \lambda)\delta\beta = 0 \tag{A.24}$$

respectively. Eliminating $\delta\beta$ in (A.23) and (A.24) we have

$$\delta\eta/\delta V = 1 + V_T \cos\gamma_T \cos\beta_o \tan(\beta_o - \lambda)/V_o \tag{A.25}$$

Making use of (A.19) to eliminate V_o in (A.25), we obtain

$$\delta\eta/\delta V = 1 + \cos\beta_o \sin^2(\beta_o - \lambda)/\cos(\beta_o - \lambda)\cos\lambda \tag{A.26}$$

For intercept to occur, $(\beta_o - \lambda)$ must lie in the interval $(-\pi/2, \pi/2)$, implying that $\cos(\beta_o - \lambda) > 0$. Further, from Figure 1, $\cos\beta_o/\cos\lambda > 0$. Note also that if $\lambda = \beta_o = \pm\pi/2$, then the second term in (A.26) is zero.

After determining h_o, E_o that maximize V subject to the constraint $T_o = D_o$, β_o is computed from (A.19) for the maximum cruise velocity, $V = V_o$; then the position costate can be determined from (A.18) and (A.21):

$$\lambda_{x_o} = -\cos\beta_o/(V - V_T \cos\gamma_T \sin\beta_o) \tag{A.27}$$

$$\lambda_{y_o} = -\sin\beta_o/(V - V_T \cos\gamma_T \sin\beta_o) \tag{A.28}$$

Note that (A.18) should not be used directly in calculating λ_{y_o} given λ_{x_o}, due to the indeterminate form that results at $\beta_o = \pm\pi/2$.

A.2 First Boundary Layer Solution

Using the time transformation $\tau = t/\varepsilon$ and letting $\varepsilon \to 0$, the necessary conditions for the first boundary layer become:

$$\mu_1 = 0, \quad \gamma_1 = 0, \quad L_1 = W \tag{A.29}$$

$$\partial H_1/\partial h = \partial H_1/\partial\beta = \partial H_1/\partial T = 0 \tag{A.30}$$

$$H_1 = \lambda_{x_o} V\cos\beta + \lambda_{y_o}(V\sin\beta - V_T\cos\gamma_T)$$
$$+ \lambda_{E_1}(T - D_o)V/W + 1 + \text{constraints} = 0 \tag{A.31}$$

Although (A.30) and (A.31) represent four nonlinear equations in four unknowns, their solution is quite straightforward.

The first boundary layer optimal heading comes from (A.30):

$$\partial H_1/\partial\beta = -\lambda_{x_o} V\sin\beta + \lambda_{y_o} V\cos\beta = 0 \tag{A.32}$$

giving

$$\beta_1 = \tan^{-1}(\lambda_{y_o}/\lambda_{x_o}) = \beta_o \tag{A.33}$$

Because T appears linearly in (A.31), we have

$$T_1 = T_{max}(h,V) \quad \text{for} \quad \lambda_{E_1} < 0 \tag{A.34}$$

$$T_1 = T_{min}(h,V) \quad \text{for} \quad \lambda_{E_1} > 0 \tag{A.35}$$

The minimization with respect to h is obtained by recognizing, as described in Appendix E, that $\partial H_1/\partial h = 0$ and $H_1 = 0$ is equivalent to

$$h_1 = \arg\min_h \left. -\frac{(T_{max}-D_o)V/W}{H_o(E,h)} \right|_{E = E_{current}} \tag{A.36}$$

for $\lambda_{E_1} < 0$, and

$$h_1 = \arg\min_h \left. \frac{(T_{min}-D_o)V/W}{H_o(E,h)} \right|_{E = E_{current}} \tag{A.37}$$

for $\lambda_{E_1} > 0$. The term $H_o(E,h)$ is the outer solution Hamiltonian evaluated at the current values of E and h. The expressions (A.36) and (A.37) roughly correspond to climb and descent, respectively. The first boundary layer costate is obtained from (A.31):

$$\lambda_{E_1} = \left. -WH_o(E,h)/V(T-D_o) \right|_{\substack{h = h_1 \\ T = T_1}} \tag{A.38}$$

As was the case with the outer solution, it is possible to obtain h_1 in a form independent of target parameters. Use of the condition $H_o(h_o,E_o)=0$

provides

$$1 - \lambda_{y_o} V_T \cos \gamma_T = -\lambda_{x_o} V_o / \cos\beta_o \tag{A.39}$$

Substituting (A.39) in (A.36) and (A.37), using the inequality in (A.21), and then eliminating multiplicative constant terms results in:

$$h_1 = \arg \min_h \left. \frac{(T_{max} - D_o)V}{V - V_o} \right|_{E = E_{current}} \tag{A.40}$$

for $\lambda_{E_1} < 0$, and for $\lambda_{E_1} > 0$:

$$h_1 = \arg \min_h \left. \frac{-(T_{min} - D_o)V}{V - V_o} \right|_{E = E_{current}} \tag{A.41}$$

It should be noted that $h_1(E_o)$, where E_o is a cruise or pseudo cruise energy level, will generally differ between climb and descent; hence the aircraft must execute a constant energy transition arc from cruise to descent altitude, as discussed in Section 3. Also of interest here is the fact that T_1 may not switch from T_{max} to T_{min} immediately upon the initiation of descent. This can be seen by substituting (A.39) in (A.38), giving

$$\lambda_{E_1} = -W \lambda_{x_o} (V - V_o)/V \, (T - D_o)\cos \beta_o \Big|_{h = h_1} \tag{A.42}$$

During climb $T_1 > D_o$ and $\lambda_{E_1} < 0$; thus, $T_1 = T_{max}$ during climb. After the initiation of descent, for large values of E_o, $T_{max} < D_o$ and initially, $V > V_o$, so we still have that $\lambda_{E_1} < 0$. Because of this, the optimality condition is $T_1 = T_{max}$ in descent until $V < V_o$, as illustrated in Figure 8. For $V < V_o$, the optimality condition is $T_1 = T_{min}$. Note from Figure 8 that if $E_o < E_s$, then $V < V_o$ initially on the descent path, and thrust should immediately switch to T_{min}.

A.3 Second Boundary Layer Solution

The heading dynamics are accounted for by introducing the time transformation $\tau = t/\varepsilon^2$ and once again letting $\varepsilon \to 0$. The necessary conditions for

optimality are

$$\gamma_2 = 0 \ , \ L^2 = W^2 + L_{22}^2 \tag{A.43}$$

$$\partial H_2/\partial h = \partial H_2/\partial T_2 = \partial H_2/\partial L_{22} = 0 \tag{A.44}$$

$$H_2 = H_1(E,h,\beta) + \lambda_{\beta_2} L_{22}/mV - \lambda_{E_1} VK L_{22}^2/qsW + \text{constraints} = 0 \tag{A.45}$$

where L_{22} is the second boundary layer horizontal lift and $H_1(E,h,\beta)$ is the first boundary layer Hamiltonian evaluated at second boundary layer conditions. Equations (A.44) and (A.45) give four nonlinear equations in four unknowns.

If we assume that all turning takes place near the initial time we have that $\lambda_{E_1} < 0$ so that the optimal thrust during turning is

$$T_2 = T_{max}\ (h_2, V_2) \tag{A.46}$$

where h_2 is the second boundary layer optimal h and V_2 is

$$V_2 = \sqrt{(E-h_2)2g}\ \Big|_{E = E_{current}} \tag{A.47}$$

Solving for the optimal horizontal lift, using (A.44) and (A.45), we obtain

$$\partial H_2/\partial L_{22} = -2\lambda_{E_1} KL_{22}\ V/qsW + \lambda_{\beta_2}/mV = 0 \tag{A.48}$$

Using (A.48) to eliminate λ_{β_2} in (A.45) results in

$$L_{22} = \sqrt{-qsWH_1(E,h,\beta)/VK\lambda_{E_1}}\ \cdot \text{sign}\ (\beta_o - \beta) \tag{A.49}$$

We also note from (A.48) that

$$\text{sign}(L_{22}) = \text{sign}(\lambda_{\beta_2}) \tag{A.50}$$

Substitution of these results in (A.45) and use of the minimization procedure detailed in Appendix E results in the following solution for h_2:

$$h_2 = \arg \min_h \{-\rho/H_1(E,h,\beta)KV\}\Big|_{\beta=\beta_{current}} \tag{A.51}$$

subject to the constraints (A.44) and (2.13-2.16). Having computed the second boundary layer controls, the costate λ_{β_2} is determined:

$$\lambda_{\beta_2} = 2H_1(E,h,\beta)mV/L_{22} \Big|_{h=h_2} \tag{A.52}$$

APPENDIX B

OPTIMIZATION OF ALTITUDE AND FLIGHT PATH ANGLE DYNAMICS

This appendix provides a detailed derivation of the zero-order control solutions optimizing altitude and flight path angle dynamics. The state equations and necessary conditions have already been summarized (A.1-A.13).

B.1 Third Boundary Layer Solution

The third boundary layer problem arises from applying the time transformation $\tau = t/\epsilon^3$ to (A.1-A.12) and letting $\epsilon \to 0$. Here, the zero-order necessary conditions for optimality are:

$$L_{13} = W \cos \gamma \tag{B.1}$$

$$\partial H_3/\partial \gamma = \partial H_3/\partial L_2 = 0 \tag{B.2}$$

$$H_3 = H_1(h,E,\beta,\gamma) - \lambda_{E_1} L_2^2 KV/qsW + \lambda_{\beta_2} L_2 g/WV \cos \gamma$$

$$\lambda_{h_3} V\sin\gamma + \nu_1(\gamma_{max}^2 - \gamma^2) + \nu_2(L_{max}^2 - W^2\cos^2\gamma - L_2^2) = 0 \tag{B.3}$$

where $H_1(h,E,\beta,\gamma)$ is the first boundary layer Hamiltonian evaluated at current values of h,E,β and γ; that is

$$H_1(h,E,\beta,\gamma) = (\lambda_{x_o}\cos\beta + \lambda_{y_o}\sin\beta)V\cos\gamma - \lambda_{y_o} V_T \cos\gamma_T + \lambda_{E_1}(T-D_o)V/W + 1 + k\sin^2\gamma \tag{B.4}$$

where

$$D_o = qsC_{D_o} + KW^2\cos^2\gamma/qs \tag{B.5}$$

The parameters λ_{x_o}, λ_{y_o}, λ_{E_1}, and λ_{β_2} are known from the outer, and first and second boundary layer solutions. Satisfaction of (B.2) for L_2 yields:

$$\partial H_3/\partial L_2 = -2\lambda_{E_1} L_2^2 KV/qsW + \lambda_{\beta_2} g/WV\cos\gamma - 2\nu_2 L_2 = 0 \qquad (B.6)$$

Note that $\nu=0$ off the lift constraint, in which case the horizontal lift solution is given by

$$L_{23} = \lambda_{\beta_2} qsg/2\lambda_{E_1} KV^2 \cos\gamma_3 \qquad (B.7)$$

On the constraint boundary, $L_{23}^2 = L_{max}^2 - W^2\cos^2\gamma$ and ν can be determined as a function of γ. In either case, L_{23} and γ can be determined as functions of γ and other known parameters. Hence, we need only combine (B.7) with the first of (B.2) and (B.3) to compute optimal γ_3 and its corresponding costate λ_{h_3}. To do this, we follow the procedure described in Appendix E, writing

$$\gamma_3 = \arg\max_{\gamma} \{\sin\gamma/H_2(h,E,\beta,\gamma)\}\cdot \text{sign}\,(h_2-h) \qquad (B.8)$$

where H_2 is the second boundary layer Hamiltonian

$$H_2 = H_1 - \lambda_{E_1} L_{23}^2 KV/qsW + \lambda_{\beta_2} L_{23} g/WV\cos\gamma \qquad (B.9)$$

For L_{23} in (B.9), (B.7) is evaluated at the search value of γ in (B.8). The maximization in (B.8) is performed over the range $0 \le \gamma \le \gamma_{max}$, where we have used the fact that $\text{sign}(\lambda_{h_3}) = -\text{sign}(\gamma) = \text{sign}(h-h_2)$ where h_2 is the optimum altitude from the second boundary layer. Having determined γ_3 and L_{23}, λ_{h_3} can be computed using (B.2):

$$\lambda_{h_3} = -\{H_1(h,E,\beta,\gamma_3) - \lambda_{E_1} L_{23}^2 KV/qsW + \lambda_{\beta_2} L_{23} g/WV\cos\gamma_3\}/V\sin\gamma_3 \qquad (B.10)$$

B.2 Fourth Boundary Layer Solution

For solutions off the lift constraint bound we write the fourth boundary layer Hamiltonian as

$$H_4 = H_3(h,E,\beta,\gamma) - \lambda_{E_1} K(2\delta L_{14} W\cos\gamma + \delta L_{14}^2) + 2(\delta L_{24} L_{23} + L_{24}^2)V/qsW$$
$$+ \lambda_{\beta_2} \delta L_{24} g/WV\cos\gamma + \lambda_{\gamma_3} \delta L_{14} g/WV = 0 \qquad (B.11)$$

where δL_{14} and δL_{24} are perturbations in the controls from the third boundary layer solutions:

$$\delta L_{14} = L_{14} - W\cos\gamma \tag{B.12}$$

$$\delta L_{24} = L_{24} - L_{23} \tag{B.13}$$

Using the conditions $H_4 = 0$, $\partial H_4/\partial \delta L_{14} = 0$ and $\partial H_4/\partial \delta L_{24} = 0$ we obtain the following solutions

$$\delta L_{24} = \lambda_{\beta_2} gqs/2\lambda_{E_1} KV^2\cos\gamma - L_{23} \tag{B.14}$$

$$\delta L_{14} = [-H_3(h,E,\beta,\gamma)qs\ W/\lambda_{E_1} KV-\delta L_{24}^2]^{1/2} \cdot \text{sign}(\gamma_3-\gamma) \tag{B.15}$$

The final lift and bank angle equations are:

$$L = \{(W\cos\gamma + \delta L_{14})^2 + (L_{23} + \delta L_{24})^2\}^{1/2} \tag{B.16}$$

$$\mu = \tan^{-1}(L_{24}/L_{14}) \tag{B.17}$$

If L in (B.16) exceeds L_{max} we set $L = L_{max}$ and reformulate the necessary conditions in order to determine the optimum bank angle.

$$L_{14} = L_{max} \cos\mu \tag{B.18}$$

$$L_{24} = L_{max} \sin\mu \tag{B.19}$$

we obtain, via $\partial H_4/\partial\mu = 0$:

$$\tan\mu = \lambda_{\beta_2}/\lambda_{\gamma_4} \cos\gamma \tag{B.20}$$

The procedure for and considerations involved in determining λ_{γ_4} are detailed in Section B.3.

It can readily be shown that the fourth boundary layer solution asymptotically approaches that of the third. From (B.7) and (B.14), we have

$$\delta L_{24} = \lambda_{\beta_2} qsg(1/2\lambda_{E_1} KV^2\cos\gamma - 1/2\lambda_{E_1} KV^2 \cos\gamma_3) \tag{B.21}$$

Since (B.21) is continuous it will asymptotically approach zero as $\gamma \to \gamma_3$. Examining the form of (B.15), it can be seen that δL_{14} also go to zero as $\gamma \to \gamma_3$, since $H_3(h,E,\beta,\gamma)$ goes to zero, as does δL_{24}.

B.3 Calculation of the Fourth Boundary Layer Costate

The costate λ_{γ_4} is determined by a quadratic equation obtained by substituting (B.20) in (B.11):

$$A\lambda^2_{\gamma_4} + B\lambda_{\gamma_4} + C = 0 \tag{B.22}$$

where

$$A = g^2(L_{max}{}^2/W^2 - \cos^2\gamma)/V^2 \tag{B.23}$$

$$B = 2\Phi g \cos\gamma/V \tag{B.24}$$

$$C = (\lambda_{\beta_2} L_{max} g/VW\cos\gamma)^2 - \Phi^2 \tag{B.25}$$

$$\Phi = H_1(h,E,\beta,\gamma,\ L=L_{max}) + \lambda_{h_3} V\sin\gamma \tag{B.26}$$

where H_1 has been defined in (B.4).

The roots of (B.22) are as follows:

$$\lambda_{\gamma_4} = (-B \pm \sqrt{B^2-4AC})/2A \tag{B.27}$$

where the term under the radical is

$$B^2-4AC = 4\{(\Phi L_{max} g/VW)^2 - (\Phi L_{max} g/VW) - (\lambda_{\beta_2} L_{max} g^2/WV^2)^2$$

$$+ (\lambda_{\beta_2} (L_{max} g/VW)^2/\cos\gamma)^2\} \tag{B.28}$$

Because we require real-valued roots for (B.22) the term (B.28) must remain nonnegative, or

$$\Phi^2 + \{1-(L_{max}/W\cos\gamma)^2\}\ (\lambda_{\beta_2} g/V)^2 \geq 0 \tag{B.29}$$

or

$$\Phi^2 \geq (L_{max}^2 - W^2 \cos^2 \gamma)(\lambda_{\beta_2} g/VW\cos\gamma)^2 \tag{B.30}$$

In the third boundary layer it can be seen that

$$L_{2_{max}}^2 = L_{max}^2 - W^2\cos^2\gamma \tag{B.31}$$

Also, the third boundary layer Hamiltonian in (B.3), evaluated at the conditions under consideration is

$$H_3 = \Phi + \lambda_{\beta_2} L_{2_{max}} g/VW \cos \gamma \geq 0 \tag{B.32}$$

The product $\lambda_{\beta_2} \cdot L_2$ is always negative, so (B.30) can be rewritten:

$$\Phi \geq |\lambda_{\beta_2} L_{2_{max}} g/VW \cos \gamma| \tag{B.33}$$

Combining (B.31) and (B.33), we can see that the inequality in (B.30) is guaranteed.

It can also be shown that the roots of (B.22) have opposite sign sense. This is required to make a selection from the two solutions for λ_{γ_4} in (B.27) The importance of the sign sense of λ_{γ_4} can be appreciated by noting that

$$\lambda_{\gamma_4} = \partial J/\partial\gamma \tag{B.34}$$

where J is the performance index (2.12). Since γ_3 is the optimal flight path angle, we have from (B.34) that

$$\delta J = \lambda_{\gamma_4}(\gamma-\gamma_3) \geq 0 \tag{B.35}$$

This indicates that λ_{γ_4} must have the same sign as $(\gamma-\gamma_3)$. To show that (B.27) always produces roots of opposite sign, note from (B.23) that $A \gtrless 0$ since $L_{max} \geq W$ within the flight envelope. Also, (B.25) and (B.33) indicate that $C \leq 0$, implying that $AC \leq 0$ in (B.28). Because of this, the term under

the radical in (B.27) has a dominating magnitude in that expression, guaranteeing real roots of opposing sign.

APPENDIX C

ORDERING OF ENERGY AND HEADING DYNAMICS

This appendix justifies the ordering selected for energy and heading dynamics. We will examine the eigenvalues associated with a linearized boundary value problem in which E and β dynamics are both considered on the same time scale ($\tau = t/\varepsilon$, in the context of Section 2). In this case, the necessary conditions during climb are:

$$dE/d\tau = (T_{max}-D)V/W \qquad d\lambda_E/d\tau = -\partial H/\partial E \tag{C.1}$$

$$d\beta/d\tau = L_2/mV \qquad d\lambda_\beta/d\tau = -\partial H/\partial \beta \tag{C.2}$$

$$\partial H/\partial h = 0 \qquad \partial H/\partial L_2 = 0 \tag{C.3}$$

$$H = \lambda_{x_o} V \cos\beta + \lambda_{y_o}(V \sin\beta - V_T \cos\gamma_T) + \lambda_E(T_{max}-D)V/W + \lambda_\beta L_2/mV + 1 = 0 \tag{C.4}$$

where λ_x and λ_y are defined in (2.20) through (2.26), and

$$D = qsC_{D_o} + K(W^2 + L_2^2)/qs \tag{C.5}$$

The second of equations (C.3) gives

$$L_2 = (\rho sg/4K\lambda_E)\lambda_\beta \tag{C.6}$$

Consider an expansion of the above conditions about the optimal climb solution at the optimal heading, so that we have

$$\bar{\lambda}_E = \lambda_{E_1}(E) \qquad \bar{\lambda}_\beta = 0$$

$$\bar{h} = h_1(E) \qquad \partial H/\partial h = 0 \qquad \bar{L}_2 = 0$$

$$d\bar{E}/d\tau = \dot{E}_1(E) \qquad \bar{\beta} = \beta_o \tag{C.7}$$

All of the nominal values in (C.7) are associated with the first boundary layer solution in Section 2. The linearized dynamics resulting from (C.1) through (C.3), (C.5) and (C.6), using primes to indicate $d(\cdot)/d\tau$, are:

$$\delta E' = (\delta E'/\partial E)\delta E + (\partial E'/\partial h)\delta h = (\partial \dot{E}_1/\partial E)\delta E \tag{C.8a}$$

$$\delta \lambda_E' = -(\partial \dot{E}_1/\partial E)\delta \lambda_E + f(E,\bar{h})\delta E \tag{C.8b}$$

$$\delta \beta' = (\bar{\rho} sg/\bar{\lambda}_E Km V_1)\delta \lambda_\beta \tag{C.9a}$$

$$\delta \lambda_\beta' = (\lambda_x/\cos \bar{\beta})V_1 \ \delta \beta \tag{C.9b}$$

where δh has been eliminated by using the first equation in (C.3). The function $f(E,\bar{h})$ does not affect the eigenvalues of (C.8). Note that (C.8) and (C.9) are decoupled. The eigenvalues of (C.8) are

$$p_E = \pm(\partial \dot{E}_1/\partial E) \tag{C.10}$$

and for (C.9), they are

$$p_\beta = \pm\sqrt{(\lambda_x/\cos \bar{\beta})\bar{\rho} sg/\bar{\lambda}_E Km} \tag{C.11}$$

where $(\lambda_x/\cos \bar{\beta})$ and $\bar{\lambda}_E$ come from (2.25) and (2.32), respectively; Further, both quantities are always negative. It can be seen from Table 5 that, for the problem described in this report, β is clearly a faster variable than E. Note that in the case where relative position dynamics are ignored [12], we have that $\lambda_x = 0$ and that E is the faster variable.

TABLE 5

COMPARISON OF EIGENVALUES ALONG CLIMB PATH FOR AN F-4 AIRCRAFT

Energy (M)	P_E(1/s)	P_β(1/s)
6705.6	± 0.0200	± 0.317
12192.0	± 0.0186	± 0.178
18288.0	± 0.0023	± 0.164
24384.0	± 0.0090	± 0.152
29870.4	± 0.00115	± 0.763
30480.0	0*	∞*

*For the F-4, $\partial E_1/\partial E = \lambda_{E_1} = 0$ in cruise due to the Mach limit.

APPENDIX D

SEPARATION OF ALTITUDE AND FLIGHT PATH ANGLE DYNAMICS

Optimization of h and γ dynamics is a classical problem in flight mechanics. This problem's difficulty lies in the fact that these dynamics are highly coupled if viewed separately from position and energy dynamics. This appendix presents summary analysis of the h and γ dynamics in the context of relative position dynamics and demonstrates that, while not completely decoupled, they can still be optimized by singular perturbation methods. A more detailed development may be found in [25].

D.1 Formulation

In order to simplify the discussion, (2.1 - 2.6) will be specialized to motion in a vertical plane, with $\beta_o = \pi/2$ and $V_T = 0$. For this problem the outer and first boundary layer solutions are as in Section 2 and Appendix A, with $\lambda_{x_o} = 0$ and $\lambda_{y_o} = -1/V_o$. Satisfaction of boundary conditions on h and γ requires further boundary layer analysis of these dynamics, using L and T as control variables. It has been shown [7] that if h and γ are chosen on the same time scale:

$$\varepsilon^2 \dot{h} = V \sin \gamma \tag{D.1}$$

$$\varepsilon^2 \dot{\gamma} = (L - W \cos \gamma)/mV \tag{D.2}$$

a nonlinear TPBVP results, the solution of which is not available in feedback form. In hope of obtaining a valid feedback solution, we are led to consider a further separation of h and γ dynamics, amending (D.2) so that γ varies on a faster time scale than h.

$$\varepsilon^3 \dot{\gamma} = (L - W \cos \gamma)/mV \tag{D.3}$$

The validity of the approximation implied in (D.3) will be examined by analyzing the eigenvalues of the linearized closed loop dynamics along the climb path. These eigenvalues will be compared to the eigenvalues for the linearized closed loop dynamics resulting from the control solution when h and γ are modeled according to (D.1) and (D.2). It is shown that a close match can be obtained by properly selecting k in (2.12).

D.2 Eigenvalue Analysis

We first consider an expansion of the second boundary layer necessary conditions for the formulation in (D.1) and (D.2). After eliminating the control as a function of states and adjoints, the following fourth order linear system results:

$$\frac{d}{d\tau}\begin{bmatrix} \delta h \\ \gamma \\ \lambda_h \\ \delta\lambda_\gamma \end{bmatrix} = \begin{bmatrix} 0 & V_1 & 0 & 0 \\ g\bar{h}/V_1\bar{\rho} & 0 & 0 & g/V_1\bar{\lambda}_\gamma \\ K_1 & 0 & 0 & -g\bar{\rho}_h/V_1\bar{\rho} \\ 0 & K_2 & -V_1 & 0 \end{bmatrix}\begin{bmatrix} \delta h \\ \gamma \\ \lambda_h \\ \delta\lambda_\gamma \end{bmatrix} \tag{D.4}$$

where

$$\bar{h} = h_1(E) \qquad K_1 = -\partial^2 H_1/\partial h^2\Big|_{\bar{h}} \lesssim 0$$

$$\bar{\lambda}_\gamma = 4m\,\lambda_{E_1} K/\bar{\rho}s < 0 \qquad K_2 = \lambda_{y_o} V_1 - \bar{\lambda}_\gamma\, g/V_1 < 0$$

$$\bar{\rho} = \rho(\bar{h})$$

$$\bar{\rho}_h = \partial\rho/\partial h\Big|_{\bar{h}} \qquad V_1 = \sqrt{2g(E-\bar{h})}$$

$$H_1 = \lambda_{y_o} V + \lambda_{E_1}(T-D_o)V/W + 1 + k\sin^2\gamma \tag{D.5}$$

The eigenvalues of (D.4) are the roots of

$$s^4 + a\,s^2 + b = 0 \tag{D.6}$$

where

$$a = g(g/V_1^2 - 2\bar{\rho}_h/\bar{\rho}) - \lambda_{y_o} g/\bar{\lambda}_\gamma \tag{D.7}$$

$$b = g\,V_1\,K_1/\bar{\lambda}_\gamma \gtrsim 0 \tag{D.8}$$

and are arranged symmetrically about the real and imaginary axes. Since it is always possible to suppress two of these modes by appropriate choice of initial conditions on λ_h and $\delta\lambda_\gamma$, a necessary condition for the existence of an asymptotically stable boundary layer solution is that none of the eigenvalues are strictly imaginary. This follows if

$$4b > a^2 \tag{D.9}$$

or

$$b > 0 \text{ and } a < 0 \tag{D.10}$$

An analysis similar to the above was conducted in [7], where relative position dynamics were ignored. In this case, $\lambda_{y_o} = 0$ so that, from (D.7), $a > 0$. Thus, the conclusion regarding existence of a boundary layer solution depends on (D.9), which must be tested for individual aircraft types. When relative position dynamics are included, the last term in (D.7) is dominant, and $a < 0$. Furthermore, it can easily be shown that, for the conditions in (D.10), the damping ratio is greater than 0.707.

We now consider the boundary layer dynamics for (D.1) and (D.2), but for the feedback control solution of Appendix B specialized to the same planar problem. This implies we are using the approximation in (D.3). When the closed loop dynamics are linearized about the climb path, we obtain the following second order system:

$$\begin{aligned} d\,(\delta h)/d\tau &= V_1\,\gamma \\ d\,\gamma/d\tau &= \delta L/m\,V \end{aligned} \tag{D.11}$$

where

$$\begin{aligned} \delta L &= -K_3\,\gamma - K_4\,\delta h \\ K_3 &= K_5(-\lambda_{y_o} V_1 + 2\,\lambda_{E_1} KWV_1/q_1\,s + 2k) \\ K_4 &= K_5(\lambda_{y_o} g^2/V_1^3 + \lambda_{E_1} \bar{\dot{E}}_{hh}) \\ K_5 &= \sqrt{-q_1\,s\,W/2\,\lambda_{E_1}\,K\,V_1} \\ \bar{\dot{E}}_{hh} &= \partial^2 \dot{E}/\partial h^2\Big|_{\bar{h}} \\ q_1 &= \bar{\rho}\,V_1^2\,/\,2 \end{aligned} \tag{D.12}$$

The eigenvalues of the closed loop system are given by the roots of

$$s^2 + K_3\,s/mV_1 + K_4/m = 0 \tag{D.13}$$

D.3 Numerical Comparison of Eigenvalues

Table D.1 displays the eigenvalues of (D.6) and (D.13) for k=0, and those of (D.13) for k=0.89 for five different energy levels along the climb path. F-8 aircraft data was used for this comparison. Note that for k=0, the damping ratio obtained using (D.13) is approximately half of that obtained from (D.6). Though not apparent from Table 6, the natural frequencies in all cases are equal.

From the second of (D.12), it is apparent that k only affects the damping ratio and not the natural frequency of the closed loop dynamics corresponding to (D.13). Thus, for a given energy level, it is possible to choose k so that the eigenvalue of (D.13) match those of (D.6). For example, in the case of the F-8 aircraft at E = 9112m, the eigenvalues are matched by selecting k = 0.89. The calculation at other energy levels is summarized in the last column of Table 6. Note that a reasonably good approximation to the eigenvalues of (D.6) is obtained at all energy levels. A better approximation results when k is chosen so that the eigenvalues are matched at E = 13528m. This approach to approximating the optimization of h and γ is closely related to a state constrained matching approach used in [12]; however, the form of the solution here is much more appropriate for real time implementation. Trajectory results for k=0 and k=0.89 are given in [25].

TABLE 6

COMPARISON OF EIGENVALUES FOR h, γ BOUNDARY LAYER DYNAMICS

Energy Level (m)	Equation(D.6)	Eigenvalues (1/s) Equation(D.13), k=0	Equation (D.13); k=0.89
9112	-.156 ± i .108	-.082 ± i .171	-.156 ± i .108
11320	-.114 ± i .078	-.064 ± i .123	-.123 ± i .063
13528	-.089 ± i .068	-.048 ± i .100	-.093 ± i .062
15737	-.069 ± i .064	-.032 ± i .089	-.064 ± i .070
17945	-.084 ± i .072	-.038 ± i .105	-.067 ± i .090

APPENDIX E

MINIMIZATION OF A HAMILTONIAN FUNCTION WITH ONE UNKNOWN COSTATE

This appendix documents a method for minimizing a Hamiltonian function with one unknown costate, the procedure having been used in minimizing the Hamiltonian for the outer solution and first through third boundary layers of the analysis in this report.

Given the Hamiltonian function

$$H(x) = f(x) + \lambda\, g(x) = 0 \tag{E.1}$$

The sufficient conditions for the existence of a minimum for (E.1) are

$$\partial H/\partial x = f_x + \lambda g_x = 0 \tag{E.2}$$

$$\partial^2 H/\partial x^2 = f_{xx} + \lambda g_{xx} > 0 \tag{E.3}$$

In a free time problem where t does not explicitly appear in H, it is also necessary that H=0. Using (E.1), this leads to

$$\lambda = -f/g\ , \qquad g \neq 0 \tag{E.4}$$

Using (E.4) in (E.2) and (E.3), we obtain:

$$\partial H/\partial x = f_x - (f/g)g_x = 0 \tag{E.5}$$

$$\partial^2 H/\partial x^2 = f_{xx} - (f/g)g_{xx} > 0 \tag{E.6}$$

Define the function

$$L = g/f \tag{E.7}$$

Taking the first and second partials

$$\partial L/\partial x = [fg_x - gf_x]/f^2 \tag{E.8}$$

$$\partial^2 L/\partial x^2 = [fg_{xx} - gf_{xx}]/f^2 - 2f_x(\partial L/\partial x)/f \tag{E.9}$$

Setting (E.8) equal to zero gives the same condition as in (E.2) and (E.4). Condition (E.6) can be rewritten

$$gf_{xx} - fg_{xx} > 0 \quad , \quad g > 0$$

$$gf_{xx} - fg_{xx} < 0 \quad , \quad g < 0 \qquad \text{(E.10)}$$

Using $\partial L/\partial x = 0$ in (E.9), it can be seen that the following will be equivalant to (E.10):

$$\partial^2 L/\partial x^2 < 0 \quad , \quad g > 0$$

$$\partial^2 L/\partial x^2 > 0 \quad , \quad g < 0 \qquad \text{(E.11)}$$

From the foregoing, we can conclude that

$$\max \{L\} \quad , \quad g > 0$$

$$\min \{L\} \quad , \quad g < 0 \qquad \text{(E.12)}$$

is equivalent to the conditions in (E.1 - E.3).

APPENDIX F

ELIMINATION OF NUMERICAL SINGULARITIES

This appendix describes the measures taken to prevent the appearance of indeterminate ratios in the control calculations, the presence of which led to discontinuities in the controls when the aircraft closely followed the optimal altitude, heading and flight path angle commands.

The expression for the first boundary layer costate (λ_{E_1}) is, from (A.38):

$$\lambda_{E_1} = -WH_o(E, h_1) \;/\; V_1(T_1 - D_o)\Big|_{E = E_{current}} \tag{F.1}$$

where H_o is the outer solution Hamiltonian and the "1" subscripts indicate values at first boundary layer optimum conditions. If the aircraft's maximum velocity cruise point lies on the zero-energy-rate contour, an indeterminate ratio results at $h=h_o$, $E=E_o$. The value of λ_{E_1} actually tends toward zero as the cruise point is approached, so before calculating λ_{E_1}, the energy rate is tested for proximity to zero. If it is too close for a reliable costate calculation, λ_{E_1} is set to zero.

Both the first and second boundary layer solutions specify an optimal altitude (h_1 and h_2), with $h_2 \to h_1$ as the aircraft heading error approaches zero. Generally, the second boundary layer optimal altitude (h_2) is determined by solving the following equation, from (A.51), using a step search in altitude:

$$h_2 = \arg\min_{h} \{-\rho/H_1(E,h,\beta)VK\}\Big|_{\beta=\beta_{current}} \tag{F.2}$$

where

$$|L_{22}| = \sqrt{-q\ s\ WH_1(E,h,\beta)/V\ K\ \lambda_{E_1}} \tag{F.3}$$

Since $H_1(E,h_1,\beta) \to 0$ as $\beta \to \beta_o$, (F.2) approaches an indeterminate form. In the control logic, aircraft heading error is tested for proximity to zero. If it falls within a certain region h_2 is set equal to h_1, eliminating the altitude search.

In the third boundary layer solution, an optimum flight path angle is calculated by solving, from (B.8):

$$\gamma_3 = \arg\max_{\gamma} \{\sin\gamma / H_2(h,E,\beta,\gamma)\} \cdot \text{sign}(h_2-h) \tag{F.4}$$

This is done by a step wise search in the same manner as in equation (F.2) Again, an indeterminate form appears in (F.4) when $h \to h_2$, since both γ_3 and $H_2 \to 0$. When $|h_2-h|$ is small, the current altitude is artifically determined to be

$$h^{\circ} = h_2 + \delta h, \qquad \delta h > 0 \tag{F.5}$$

Requiring δh to be positive precludes violation of the mach constraint boundary. Then γ_3 and λ_{h_3} are calculated in the usual manner, but for $h=h^{\circ}$. Finally, since both γ_3 and λ_{h_3} are zero for $h=h_2$, γ_3 and λ_{h_3} are corrected using a linear interpolation:

$$\gamma_3 = \gamma_3 \, (h-h_2)/\delta h \tag{F.6}$$

$$\lambda_{h_3} = \lambda_{h_3} \, (h-h_2)/\delta h \tag{F.7}$$

Although all calculations in the fourth boundary layer are analytic, it has been found that, due to accumulated numerical inaccuracies in the preceding boundary layer solutions, there is a lack of numerical definition when the flight path angle error becomes small. When this occurs, the flight path angle is perturbed:

$$\gamma^{\circ} = \gamma_3 + \text{sign}\{\gamma - \gamma_3\} \cdot \delta\gamma \, , \qquad \delta\gamma > 0 \tag{F.8}$$

The optimal horizontal and vertical incremental lifts (δL_{14} and δL_{24}) for this boundary layer are then calculated using γ° according to the procedure detailed in Appendix B. Then the following corrections are applied:

$$\delta L_{14} = \delta L_{14} \cdot |(\gamma-\gamma_3)/\delta\gamma| \tag{F.9}$$

$$\delta L_{24} \quad \delta L_{24} \cdot |(\gamma-\gamma_3)/\delta\gamma| \tag{F.10}$$

REFERENCES

1. Kelley, H.J. and Edelbaum, T.N.: "Energy Climbs, Energy Turns and Asymptotic Expansions," J. Aircraft, Vol. 7, 1970, pp. 93-95.

2. Kelley, H.J.: "Singular Perturbations for a Mayer Variational Problem", AIAA J., Vol. 8, 1970, pp. 1177-1178.

3. Kelley, H.J.: Boundary-Layer Approximation to Powered-Flight Altitude Transients," J. Spacecraft and Rockets, Vol. 7, 1970, pg. 879.

4. Kelley, H.J.: Flight Path Optimization with Multiple Time Scales, J. Aircraft, Vol. 8, 1971, pp. 238-240.

5. Kelley, H.J.: Reduced-Order Modelling in Aircraft Mission Analysis, AIAA J., Vol. 9, 1971, pgs. 349-350.

6. Kelley, H.J.: Aircraft Maneuver Optimization by Reduced Order Approximation, Control and Dynamic Systems, Vol. 10, T. C. Leondes, ed., Academic Press, New York, 1973, pp. 131-178.

7. Ardema, M.D.: Solution of the Minimum-Time-to-Climb Problem by Matched Asymptotic Expansions, AIAA J., Vol. 14, 1976, pp. 843-850.

8. Ardema, M.D.: Nonlinear Singularly Perturbed Optimal Control Problems with Singular Arcs, IFAC 7th Triennial World Congress, Helsinki, 1978, pp. 929-936.

9. Breakwell, J.V.: More About Flight-Path-Angle Transitions in Optimal Airplane Climbs, AIAA J. Guidance and Control, Vol. 1, 1978, pp. 205-208.

10. Calise, A.J.: Singular Perturbation Methods for Variational Problems in Aircraft Flight, IEEE Trans. on Automatic Control, Vol. AC-23, No. 3, 1976, pp. 345-353.

11. Aggarwal, R., Calise, A.J. and Goldstein, F.: Singular Perturbation Analysis of Optimal Flight Profiles for Transient Aircraft, Proc. JACC, 1977, pp. 1261-1269.

12. Calise, A.J.: Extended Energy Management Methods for Flight Performance Optimization, AIAA J.; Vol. 15, 1977, pp. 314-321.

13. Calise, A.J.: Energy Management and Singular Perturbation in Flight Mechanics, Proc. IFAC Triennial World Congress, Helsinki, 1978, pp. 949-955.

14. Calise, A.J.: A New Boundary Layer Matching Procedure for Singularly Perturbed Systems, IEEE Trans. Automatic Control, Vol. AC-23, 1978, pp. 434-438.

15. Calise, A.J.: A Singular Perturbation Analysis of Optimal Aerodynamic and Thrust Magnitude Control, IEEE Trans. Automatic Control, Vol. AC-24, 1979, pp. 720-730.

16. Calise, A.J.: A Singular Perturbation Analysis of Optimal Thrust Control with Proportional Navigation Guidance, AIAA J. of Guidance and Control, Vol. 3, No. 4, 1980, pp. 312-318.

17. Shinar, J., Negrin, M., Well, K.H. and Berger, E.: Comparison Between the Exact and an Approximate Feedback Solution for Medium Range Interception Problems, Proc. JACC, 1981, Paper TA-1A.

18. Mehra, R., Washburn, R., Sajan, S. and Carroll, J.: A Study of the Application of Singular Perturbation Theory, NASA CR-3167, 1979.

19. Shinar, J. and Gutman, S.: Recent Advances in Optimal Pursuit and Evasion, IEEE Conf. on Decision and Control, 1979.

20. Shinar, J. and Farber, N.: An Approximate Solution of Singularly Perturbed Non-Linear Pursuit-Evasion Games, TAE No. 359, Technion-Israel Inst. Tech., Haifa, Israel, 1979.

21. Shinar, J. and Farber, N.: A Variable Modelling Approach for Singularly Perturbed Pursuit-Evasion Problems, Israel Annual Conf. on Aviation and Astronautics, 1981.

22. Shinar, J.: Remarks on Singular Perturbation Technique Applied in Nonlinear Optimal Control, IFAC Workshop on Control Applications of Nonlinear Programming and Optimization, Oberpfaffenhofen, Germany, 1980.

23. Price, D., Calise, A. and Moerder, D.: Piloted Simulation of an On-Board Trajectory Optimization Algorithm, Proc. JACC, 1981, Paper No. TA-1C.

24. Aerodynamic Data Package Provided by D. Price, NASA Langley Research Center, Flight Mechanics and Control Division, Hampton, VA 23665.

25. Calise, A.J.: On-Line Optimization of Aircraft Altitude and Flight Path Angle Dynamics, Proc. JACC, 1981, Paper No. TA-1B.

1. Report No.	2. Government Accession No.	3. Recipient's Catalog No.
NASA CR-3597		

4. Title and Subtitle	5. Report Date
SINGULAR PERTURBATION TECHNIQUES FOR REAL TIME AIRCRAFT TRAJECTORY OPTIMIZATION AND CONTROL	August 1982
	6. Performing Organization Code
7. Author(s)	8. Performing Organization Report No.
Anthony J. Calise Daniel D. Moerder	
9. Performing Organization Name and Address	10. Work Unit No.
Drexel University Department of Mechanical Engineering & Mechanics Philadelphia, PA 19104	11. Contract or Grant No. NSG-1496
12. Sponsoring Agency Name and Address	13. Type of Report and Period Covered Contractor Report 2/78 - 12/81
National Aeronautics and Space Administration Washington, DC 20546	14. Army Project No.

15. Supplementary Notes

Langley Technical Monitor: Douglas B. Price
Final Report

16. Abstract

This study examines the usefulness of singular perturbation methods for developing real time computer algorithms to control and optimize aircraft flight trajectories. A minimum time intercept problem using F-8 aerodynamic and propulsion data is used as a baseline. This provides a framework within which issues relating to problem formulation, solution methodology and real time implementation are examined. Theoretical questions relating to separability of dynamics are addressed. With respect to implementation, situations leading to numerical singularities are identified, and procedures for dealing with them are outlined. Also, particular attention is given to identifying quantities that can be precomputed and stored, thus greatly reducing the on-board computational load. Numerical results are given to illustrate the minimum time algorithm, and the resulting flight paths. An estimate is given for execution time and storage requirements.

17. Key Words (Suggested by Author(s))	18. Distribution Statement
Trajectory Optimization Minimum Time Control Model Order Reduction Perturbation Methods Flight Control Algorithms	Unclassified - Unlimited Subject Category 08

19. Security Classif. (of this report)	20. Security Classif. (of this page)	21. No. of Pages	22. Price*
Unclassified	Unclassified	112	A06

*For sale by the National Technical Information Service, Springfield, Virginia 22161

NASA-Langley, 1982